Ph.D Thesis

Tunable devices from moiré superlattices

By

ALEKSANDER SANJUAN CIEPIELEWSKI

International Centre for Interfacing Magnetism and Superconductivity with Topological Matter-(MagTop)
in
Division ON-6 of Institute of Physics, Polish Academy of Sciences (IF PAN)

Submitted in partial fulfillment of the requirements for the degree Doctor of Philosophy
Supervised by **Dr. hab. Wojciech Brzezicki**, Institute Professor, and co-supervised by **Prof. dr. hab. Jakub Tworzydło**, University of Warsaw Professor

JUNE 16, 2025

Abstract in English

Recent advancements in the fabrication and manipulation of two-dimensional (2D) materials have opened new frontiers in condensed matter physics and nanoelectronics. The ability to isolate and stack atomically thin layers with precise control over their relative orientation has led to the discovery of novel quantum phenomena. In particular, heterostructures composed of graphene, transition metal dichalcogenides, black phosphorus, and other 2D materials bound via van der Waals forces exhibit remarkable optoelectronic properties, such as topological effects, high-temperature superconductivity and other unconventional correlated phases. In addition, the physical properties of 2D materials can be precisely adjusted through external stimuli, for instance with electric fields, strain, doping, and manipulation of relative layer orientation. The capacity to finely tune the physical properties of such systems offers a plethora of possible applications for condensed matter research and future optoelectronic technologies.

A particularly striking example is twisted bilayer graphene, where a small relative twist angle between the two graphene layers introduces a moiré superlattice, *i.e.* a long-wavelength periodic potential, that dramatically modifies the electronic structure. At specific "magic angles," twisted bilayer graphene exhibits unconventional strongly correlated insulating phases and superconductivity, challenging conventional theories of electron behavior in solids. Beyond twisted bilayer graphene, moiré superlattices in other 2D systems, such as twisted transition metal dichalcogenides or graphene-hBN heterostructures, further expand the landscape of tunable quantum devices, enabling the engineering of flat bands, pseudospin textures, and excitonic phenomena.

This work explores the physical properties and functionality of tunable optoelectronic devices based on moiré superlattices, through the study of mesoscopic devices made of twisted bilayer graphene. We develop a novel method based on the tight-binding formalism for the numerical study of graphene-based moiré mesoscopic systems. This method of analysis is capable of probing the optoelectronic properties of large multilayered 2D systems with millions of atoms. We discuss how twist angle, interlayer coupling, and external perturbations can be harnessed to control device properties on demand, paving the way for next-generation quantum electronics, sensors, and programmable metamaterials. In particular, we show that van Hove singularities in the moiré band structure can be used to strongly enhance electron correlations, since these singularities lead to a diverging electron density of states. We further connect these features of the moiré band structure with quantum transport simulations, and show that the enhanced density of states has significant effects on measurable physical quantities, with promising potential applications. We show that the energetic position of van Hove singularities is tunable with uniaxial pressure between the graphene layers, and that near a "magic angle" it is just a few meVs from the Fermi level. Thus, a slight shift in the Fermi level (which can easily be induced using simple metallic contacts or doping) can drastically change the quantum transport properties of this remarkable material. Additionally, we discuss a significant challenge in studying and utilizing 2D materials:

the presence of various types of disorder and its substantial impact on the system's optoelectronic properties. Our analysis of disorder in twisted bilayer graphene reveals challenges in creating scalable, tunable moiré nanodevices. However, based on our study, we propose a characterization of disorder that might enable researchers to quantify disorder in real samples through simple quantum transport measurements. Finally, we provide an outlook on future research in this rapidly evolving field.

Abstract in Polish

Ostatnie postępy w produkcji i manipulacji materiałami dwuwymiarowymi (2D) otworzyły nowe granice w fizyce materii skondensowanej i nanoelektronice. Zdolność do izolowania i układania atomowo cienkich warstw z precyzyjną kontrolą ich względnej orientacji doprowadziła do odkrycia nowych zjawisk kwantowych. W szczególności heterostruktury złożone z grafenu, dichalkogenków metali przejściowych, czarnego fosforu i innych materiałów 2D związanych siłami van der Waalsa wykazują niezwykłe właściwości optoelektroniczne, takie jak efekty topologiczne, nadprzewodnictwo wysokotemperaturowe i inne niekonwencjonalne fazy skorelowane. Ponadto, właściwości fizyczne materiałów 2D można precyzyjnie regulować za pomocą bodźców zewnętrznych, na przykład za pomocą pól elektrycznych, odkształceń, domieszkowania i manipulacji względną orientacją warstw. Zdolność do precyzyjnego dostrajania właściwości fizycznych takich systemów oferuje mnóstwo możliwych zastosowań w badaniach nad materią skondensowaną i przyszłych technologiach optoelektronicznych.

Szczególnie uderzającym przykładem jest skręcony grafen dwuwarstwowy, w którym niewielki względny kąt skręcenia między dwiema warstwami grafenu wprowadza supersieci moiré, czyli okresowy potencjał o dużej długości fali, który radykalnie modyfikuje strukturę pasmową elektronów. Przy określonych "magicznych kątach" skręcony grafen dwuwarstwowy wykazuje niekonwencjonalne, silnie skorelowane fazy izolacyjne i nadprzewodnictwo, podważając konwencjonalne teorie zachowania elektronów w ciałach stałych. Oprócz skręconego dwuwarstwowego grafenu, supersieci moiré w innych układach 2D, takich jak skręcone dichalkogenki metali przejściowych lub heterostruktury grafen-hBN, dodatkowo poszerzają możliwości przestrajalnych urządzeń kwantowych, umożliwiając inżynierię płaskich pasm, tekstur pseudospinowych i zjawisk ekscytonowych.

Niniejsza praca bada właściwości fizyczne i funkcjonalność przestrajalnych urządzeń optoelektronicznych opartych na supersieciach moiré, poprzez badanie urządzeń mezoskopowych wykonanych ze skręconego dwuwarstwowego grafenu. Opracowaliśmy nową metodę opartą na formalizmie ciasnego wiązania do numerycznego badania układów mezoskopowych opartych na grafenie. Ta metoda analizy jest w stanie badać właściwości optoelektroniczne dużych wielowarstwowych układów 2D z milionami atomów. Omawiamy, w jaki sposób kąt skręcenia, sprzężenie międzywarstwowe i zewnętrzne perturbacje mogą być wykorzystane do kontrolowania właściwości urządzenia na żądanie, torując drogę dla elektroniki kwantowej nowej generacji, czujników i programowalnych metamateriałów. W szczególności pokazujemy, że osobliwości van Hove'a w strukturze pasmowej moiré mogą być wykorzystane do silnego wzmocnienia korelacji elektronowych, ponieważ osobliwości te prowadzą do rozbieżnej gęstości stanów elektronowych. Ponadto łączymy te cechy struktury pasmowej moiré z symulacjami transportu kwantowego i pokazujemy, że zwiększona gęstość stanów ma znaczący wpływ na mierzalne wielkości fizyczne, z obiecującymi potencjalnymi zastosowaniami. Pokazujemy, że pozycja energetyczna osobliwości van Hove'a jest przestrajalna za pomocą jednoosiowego ciśnienia między warstwami

grafenu, a że w pobliżu „magicznego kąta” znajduje się zaledwie kilka meV od poziomu Fermiego. Tak więc niewielkie przesunięcie poziomu Fermiego (które można łatwo wywołać za pomocą prostych kontaktów metalicznych lub domieszkowania) może drastycznie zmienić właściwości transportu kwantowego tego niezwykłego materiału. Dodatkowo omawiamy istotne wyzwanie w badaniu i wykorzystywaniu materiałów 2D: obecność różnego rodzaju nieuporządkowania i jego znaczący wpływ na właściwości optoelektroniczne układu. Nasza analiza nieporządku w skręconym grafenie dwuwarstwowym ujawnia wyzwania w tworzeniu skalowalnych, przestrajalnych nanourządzeń moiré. Jednakże, w oparciu o nasze badania, proponujemy charakterystykę nieporządku, która może umożliwić badaczom ilościowe określenie zaburzeń w rzeczywistych próbkach poprzez proste pomiary transportu kwantowego. Na koniec przedstawiamy perspektywy przyszłych badań w tej szybko rozwijającej się dziedzinie.

This work is dedicated to my loving family and future wife for their support and care; to my two outstanding supervisors for their academic guidance and mentorship; and to my inspiring high school physics teacher, Oscar Ocampo, who sparked my interest in physics.

AUTHOR'S DECLARATION

I hereby certify that the work contained in this dissertation has not been submitted for consideration in any other academic awards and has been completed in accordance with the rules and guidelines of the Institute of Physics, Polish Academy of Science (IFPAN) and the Code of Practice for Research Degree Programs. Unless otherwise specified by a specific reference in the text, the work is the candidate's own contribution. Work accomplished with the assistance of or in collaboration with others is acknowledged as such. In the dissertation, only the author's viewpoints are given.

SIGNED: ..... DATE: .....

Table of Contents

List of Figures

Figure **Page**

CHAPTER 1

INTRODUCTION

The discovery of graphene in 2004 [1] marked the beginning of a new era in condensed matter physics and gave rise to the field of ultra-thin two-dimensional (2D) materials. Graphene exhibited extraordinary electronic, mechanical, and optical properties, including ultrahigh carrier mobility, exceptional tensile strength, and quantum Hall effects at room temperature [2–6]. These properties are a consequence of its unique 2D hexagonal structure, where electrons at low energies behave as relativistic massless Dirac fermions. The success of graphene spurred intense research into other 2D materials, and as a result, additional stable layered materials were quickly discovered. The growing family of 2D crystals now includes intriguing materials such as hexagonal boron nitride hBN, transition metal dichalcogenides, and black phosphorus, among others.

Advances in synthesis techniques, such as chemical vapor deposition [7] and molecular beam epitaxy [8], have enabled the large-scale production of high-quality 2D materials, facilitating their integration into functional devices. In addition, the ability to stack different 2D layers via van der Waals assembly has opened up unprecedented opportunities for designing heterostructures with tailored mechanical, electronic, and optical properties. These technological advances have paved the way for exploring novel quantum phenomena and developing functional devices with tunable properties.

Early studies of graphene focused on its intrinsic physical properties, highlighting its usefulness for potential applications. However, the gapless band structure of graphene constituted a major drawback of this material, especially for optical devices. A breakthrough came after studies revealed that a two-layer graphene crystal, known as Bernal-stacked (or AB-stacked) bilayer graphene, possesses an adjustable energy gap via an interlayer electrostatic potential [9]. Although Bernal-stacked bilayer graphene does not have Dirac fermions, it still inherits most of the useful properties of graphene, and its tunable bandgap expands the range of possible applica-

tions. Further research has shown that multilayer graphene systems have an extraordinarily wide range of exotic properties and potential applications [10]. More than two decades after graphene was first realized in a laboratory, research into multilayer graphene systems continues to surprise the materials science community. Recently in 2024, a study reported the fractional quantum anomalous Hall effect in pentalayer graphene. [11].

In parallel with efforts to understand the physical properties of multilayer graphene systems, theoretical studies reported on interesting effects that occur in the band structure of 2D periodic systems when they are stacked at a relative angle. Twisting stacked 2D materials bound by van der Waals forces can lead to the formation of a *moiré superlattice* which has its own distinctive moiré band structure. Then, two theoretical studies in 2010 and 2011 predicted the formation of nearly-flat moiré bands near the Fermi level in small-angle *twisted bilayer graphene* [12, 13]. Next, in 2018 researchers made a truly groundbreaking discovery when they stacked two graphene layers at a twist angle of $\theta \approx 1.1°$. Yuan Cao *et al.* observed that twisted bilayer graphene exhibits extraordinary electronic properties at this critical angle [14, 15]. These extraordinary properties led the community to label this critical twist angle a *magic angle*. The moiré nearly dispersionless bands of magic-angle twisted bilayer graphene have a bandwidth of only a few tens of meVs [12, 13], approximately two orders of magnitude lower than graphene's bandwidth. The quasi-flat electron bands have a sharply enhanced low-energy density of states, resulting in strongly correlated behavior. This behavior leads to a plethora of unconventional correlated phases, such as high-temperature superconductivity and Mott insulation. These findings revolutionized the field of 2D materials science and gave rise to the subfield of *twistronics*, the study of 2D materials stacked at a relative angle. The twist angle was found to be a powerful parameter for tuning the electronic, optical, and magnetic properties of various kinds of 2D heterostructures. The discovery of correlated insulating states and unconventional superconductivity in twisted bilayer graphene demonstrated that moiré superlattices could serve as versatile platforms for exploring quantum many-body physics without the need for high chemical doping or strong magnetic fields.

Following the success of twisted bilayer graphene, researchers investigated moiré physics in other 2D materials, particularly in heterostructures that can be stacked via van der Waals forces, such as transition metal dichalcogenides (TMDs). TMDs typically have a direct bandgap in their monolayer form, making them attractive for optoelectronic applications [16]. In general, 2D materials have a wide range of semiconducting bandgaps, ranging from the terahertz and mid-infrared in bilayer graphene and black phosphorus, visible in TMDs, to the ultraviolet in hBN [17]. When twisted, TMD heterobilayers exhibit moiré excitons (bound electron-hole pairs localized by the moiré potential of the superlattice) leading to tunable optical properties and enhanced many-body interactions [18]. Recent studies reveal that, like twisted bilayer graphene, twisted TMDs host exotic quantum phases at small twist angles, including generalized Wigner crystals, quantum emitters, and hybridized exciton-polaritons [19]. The ability to engineer moiré superlattices with tailored properties has led to the development of tunable devices with a wide

range of potential applications in electronics, photonics, and quantum technologies in general. The twist angle serves as a modulator of the interlayer hybridization, enabling precise control over the electronic band structure and the coupling of moiré electrons. Other parameters, such as uniaxial out-of-plane pressure, or interlayer electrostatic potential, can also be used to fine-tune the optoelectronic properties of these 2D systems [20].

Despite progress in the field of twistronics over the last decade, research has been hindered by the difficulty of theoretically studying moiré systems. Most of the interesting phenomena occur at very small twist angles, in the range between 1° and 5°, near the so-called "magic angles". At these critical points, the unit cell of the moiré superlattice is enormous, encompassing hundreds, thousands or even tens of thousands of atoms. Thus, theoretical models are often limited to long-wavelength mean-field approaches or to *ab initio* calculations of a few atoms in a single moiré unit cell. These approaches are incapable of analyzing fine details in the band structure or correlations at the moiré scale. Even in the case of twisted bilayer graphene, the first-discovered and simplest van der Waals heterostructure studied in twistronics, it is difficult to study theoretically this material due to the mesoscopic scale of the moiré supercell at small angles [20].

In this work, we present a powerful approach that balances theoretical rigor with practical feasibility for the study of moiré physics in twisted 2D systems at small angles. Then, we discuss the results of our research of magic-angle twisted bilayer graphene, which we obtained utilizing this method. Our approach essentially consists of combining band-structure analysis with quantum transport characteristics to probe the physical properties of large mesoscopic samples made of 2D moiré materials. The material itself is modeled using an effective tight-binding system defined in real space. We argue that tight-binding methods are currently the best way to explore the low-energy physics of small-angle moiré systems, because they can be scaled up to include correlations at the moiré scale. We demonstrate that this method can be used to derive most of the ground state electronic properties. Additionally, quantum transport calculations provide precise information that can be used to accurately predict measurable physical properties. The results of our studies of twisted bilayer graphene are in agreement with recent experimental measurements of high-quality samples of this material. Moreover, our flexible approach allows us to study more complex effects, such as certain types of electron-electron interactions, lattice defects, and various types of disorder. These effects are prevalent in real samples and pose a significant challenge for experimentalists when analyzing measurements of real devices.

Finally, despite our focus on mesoscopic twisted bilayer graphene, we wish to emphasize that our approach is not limited to graphene-based moiré systems. Our method only requires that the material be modeled with an effective tight-binding system that accurately describes the low-energy band structure. Fortunately, many effective tight-binding models of monolayer and multilayer heterostructures have been developed over the last decade. Besides multilayer graphene systems, effective tight-binding models can describe many other materials, such as

TMDs [21, 22]) and hBN-based systems [23]. Therefore, our method constitutes a timely, useful, and flexible approach for the study of moiré materials.

This thesis is organized as follows: In chapter 2 we present the band theory of monolayer, bilayer, and twisted bilayer graphene, with emphasis on the latter. We discuss in detail the low-energy electronic properties of twisted bilayer graphene, in particular the low-energy band structure at small twist angles. We further highlight the special importance of the tight-binding method for our approach. In chapter 3 we present an introduction to the theory of coherent quantum transport, which is the theoretical underpinning of the conductance results presented in latter chapters. In chapter 4 we detail our numerical method, showing the connection between the theory and the numerical implementation of quantum transport simulations. Chapters 5 and 6 present the results of our research on magic-angle twisted bilayer graphene. We show the connection between critical points, called van Hove singularities, in the moiré bands and the sharply enhanced low-energy conductivity of small-angle twisted bilayer graphene. In addition, the effects of uniaxial out-of-plane pressure, Hartree interactions, and lattice corrugation are all discussed in these latter chapters.

Each chapter begins with an introduction, and ends with a summary where the main results their implications are discussed. At the end of this work we present an outlook for the field in chapter 7, where we discuss promising areas of research and potential applications, as well as the most significant difficulties. The main results presented in the latter chapters 5 and 6 constitute our own contributions to this field, and were published in two prestigious scientific journals, which are found in Refs. [20, 24].

CHAPTER 2

TWISTED BILAYER GRAPHENE

Twisted bilayer graphene is a truly remarkable material that recently attracted interest from the materials science community due to its exotic properties at certain twist angles, commonly referred to as *magic angles* [12–15, 25–30]. Near a magic angle, twisted bilayer graphene becomes a strongly correlated and highly sensitive system. In addition, its optical and electronic properties are often controllable with external parameters, such as pressure, electrochemical potentials, electromagnetic fields, and especially twist-angle variation [20, 31–33]. Moreover, magic-angle twisted bilayer graphene exhibits enhanced electronic interactions and the appearance of superconductivity and other unconventional correlated phases [14, 15, 29, 31, 34–42]. The strong tunability of the electronic properties of this material in regards to its twist angle has heralded the development of the field of *twistronics* [43].

The unusual properties of magic-angle twisted bilayer graphene are principally a consequence of the presence of four exceptionally flat low-energy bands near the Fermi level. At the *first magic angle* $\theta_m \approx 1.05^\circ$ the bandwidth is just a few tens of meVs (there are many magic angles in twisted bilayer graphene, θ_m is the first from high to low, the closest to the experimentally discovered magic angle $\theta_m \approx 1.1^\circ$ [14], and the most frequently studied). In addition, these quasi-flat *moiré* bands have important additional features, such as critical points near the Fermi level known as van Hove singularities, where the electron density of states diverges [44]. Van Hove singularities have been recognized in recent theoretical works as playing a crucial role in the correlated phenomena of twisted bilayer graphene [27, 35, 36]. In general, van Hove singularities occur naturally in two-dimensional periodic systems due to the folding of the reciprocal lattice. Indeed, in graphene we find them a few eVs from the charge neutrality point. However, van Hove singularities are typically far from the Fermi level, and therefore their effects are not relevant to the low-energy theory (although graphene can be over-doped and have its Fermi level tuned to the energy of van Hove singularities [45]). In the case of magic-angle twisted bilayer graphene,

the fact that the moiré bands are so flat and close to the Fermi energy, means that van Hove singularities can be reached by tuning the energy by just a few meVs. Moreover, varying the twist angle near a magic angle shifts the energetic position of van Hove singularities, offering a powerful leverage to control the optoelectronic properties of this material. At twist angles slightly bellow the first magic angle, van Hove singularities can even cross the Fermi energy [20], sharply enhancing the zero-energy conductivity and other Fermi-level electronic properties. The sensitivity of this system is extraordinary: a variation of the twist angle of just a few hundredths of a degree near a magic angle can have remarkably large effects in its electronic and optical properties. For example, near θ_m a deviation of $\delta\theta \approx 0.01^\circ$ can shift the conductivity by about one order of magnitude [20].

In this chapter we develop the low-energy band theory of twisted bilayer graphene. Starting in Sec. 2.1 with graphene, we discuss its band structure and explain why the tight-binding method is exceptionally well-suited for graphene systems. We then utilize this approach to calculate graphene's spectrum and discuss its low-energy theory, where we find a linear dispersion of its two modes near the Fermi level. Next we describe the band structure of untwisted bilayer graphene in Sec. 2.2, and discuss its two common stable configurations, $AA-$ and $AB-$stacked bilayer graphene. We further describe the changes that occur in the spectrum due to the coupling of the layers, and conclude that bilayer graphene can generically be described as two weakly coupled graphene layers. Then, in Sec. 2.3 we develop the band theory of twisted bilayer graphene utilizing two approaches: the first, in Sec. 2.3.1, is a Dirac continuum model that is well-suited to describe the most fundamental properties of the moiré bands in the small-angle regime. Using this model we discuss the two most significant properties of the moiré bands at small angles: their remarkably small bandwidth and the presence of critical points, van Hove singularities, near the Fermi level. However, we find that the continuum model is insufficient for our quantitative approach, and therefore introduce a more flexible method based on the tight-binding formalism. This second approach constitutes a simple and very flexible effective model that is capable of reproducing the energy bands of twisted bilayer graphene to a remarkable precision. We also explain why it is this second approach that proves a powerful method of analysis for twisted bilayer graphene devices, and why other models prove unsatisfactory or unfeasible. Finally, we show that this simple method is not limited to the study of pristine samples. Many complex factors can be incorporated to the model with relative easiness. We show this in case of electron-electron Hartree interactions, corrugation of the layers and various types of lattice disorder.

2.1 Graphene

Graphene is a two-dimensional material composed of a single atomic layer of carbon atoms arranged in a hexagonal (honeycomb) lattice, as pictured in Fig. 2.1. It is an allotrope of carbon formed by strong covalent bonds of hybrid sp^2 orbitals, with a molecular bond length of $l =$

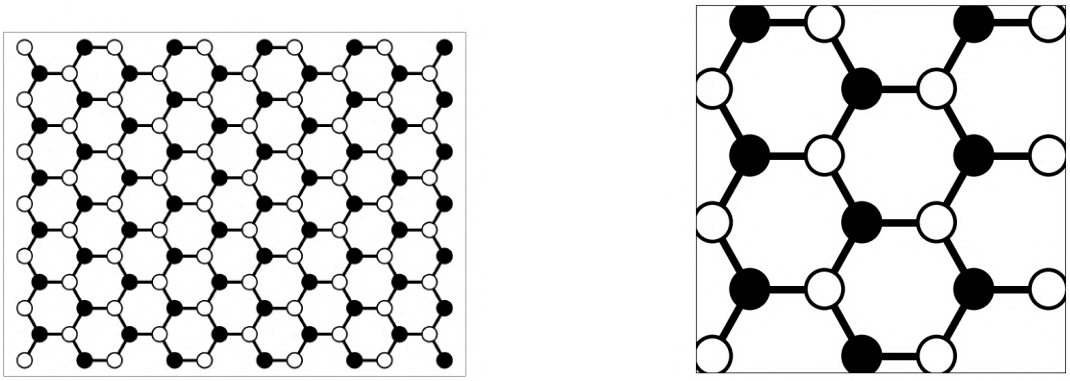

(a) (b)

Figure 2.1: Graphene lattice structure.

0.142 nm. The trigonal hybridization of the s and p atomic orbitals in carbon gives graphene its triangular Z_3 symmetry. The honeycomb lattice has a basis of two ions in each unit cell, which we label as A and B, shown as white (A sites) and black (B sites) dots in Fig. 2.1. We can then choose the following primitive lattice vectors:

$$\mathbf{a}_1 = \frac{a}{2}\left[\sqrt{3},1\right], \quad \mathbf{a}_2 = \frac{a}{2}\left[\sqrt{3},-1\right].$$

Notice that in our notation $a = 2.46$ Å denotes the primitive translation length of the hexagonal lattice, and not the nearest-neighbor distance, which is instead $l = a/\sqrt{3}$. The corresponding reciprocal vectors can be calculated with the formula

$$\mathbf{b}_i = 2\pi \frac{\mathbf{a}_j \times \mathbf{a}_k}{\mathbf{a}_i \cdot (\mathbf{a}_j \times \mathbf{a}_k)}, \tag{2.1}$$

where $i,j,k = 1,2,3$, and we set $\mathbf{a}_3 = [0,0,1]$. This yields the reciprocal lattice translations

$$\mathbf{b}_1 = \frac{2\pi}{a\sqrt{3}}\left[1,\sqrt{3}\right], \quad \mathbf{b}_2 = \frac{2\pi}{a\sqrt{3}}\left[1,-\sqrt{3}\right]. \tag{2.2}$$

The reciprocal lattice is also a hexagonal, but rotated by an angle of $\pi/2$.

To calculate the spectrum of graphene we use the tight-binding method. Firstly, we need to establish the number of hopping integrals to be considered. For graphene, the simplest nearest-neighbor model provides a very accurate approximation, and exhibits the most important properties of the spectrum. This is mainly due to two factors: the fast exponential decay of the overlap integrals, and the strong screening of next-nearest-neighbor hoppings. The latter effect is a consequence of the two-dimensional geometry of graphene: if we draw a line $\overline{XY}$ connecting two distant sites labeled X and Y, we find that at least one intermediate site Z is

placed in the vicinity of $\overline{XY}$. Then, the sp^2 orbital of site Z overlaps more with the orbitals in sites X and Y than the orbitals of X and Y with each other. This effectively screens the hopping integral of distant hoppings. Since all sites are locked in a two-dimensional hexagonal lattice, necessarily there are intermediate sites between any distant pair of atoms. In agreement with this, numerical studies indicate that the low-energy electronic bands of nearest-neighbor graphene are effectively identical to those of the next-nearest-neighbor graphene [46, 47]. We note that the inclusion of next-nearest neighbor hoppings does break electron-hole symmetry $H(\mathbf{k}) \to -H(\mathbf{k})$, and experimental results show a deviation from the ideal behavior of the Dirac quasiparticles at energies above 500 meV [48]. Nonetheless, this effect is not significant for the low-energy theory of graphene. Therefore, throughout this work we utilize the nearest-neighbor tight-binding approximation for the description of the low-energy band structure of monolayer graphene.

We write the Hamiltonian within the formalism of second quantization, since it is especially well-suited for tight-binding systems. Let us define the annihilation operators of electrons at the lowest orbitals centered around atoms in sites A and B as $C_A(\mathbf{r})$ and $C_B(\mathbf{r})$. To describe electrons, these operators must satisfy the fermionic commutation relations:

$$\left\{C_{A|B}(\mathbf{r}), C^\dagger_{A|B}(\mathbf{r})\right\} = 1, \quad \left\{C_{A|B}(\mathbf{r}), C_{A|B}(\mathbf{r})\right\} = \left\{C^\dagger_{A|B}(\mathbf{r}), C^\dagger_{A|B}(\mathbf{r})\right\} = 0. \tag{2.3}$$

Then, the nearest-neighbor tight-binding Hamiltonian can be written as

$$H = -t \sum_{\mathbf{r},\boldsymbol{\delta}} C^\dagger_A(\mathbf{r}) C_B(\mathbf{r}+\boldsymbol{\delta}) + h.c., \tag{2.4}$$

where $t = 3.09\,\text{eV}$ is the nearest-neighbor hopping integral and $\boldsymbol{\delta}$ designates the three vectors connecting A atoms with their neighboring B atoms:

$$\boldsymbol{\delta}_1 = \frac{a}{2\sqrt{3}}\left[1, \sqrt{3}\right] \quad \boldsymbol{\delta}_2 = \frac{a}{2\sqrt{3}}\left[1, -\sqrt{3}\right], \quad \boldsymbol{\delta}_3 = \frac{a}{\sqrt{3}}[-1, 0]. \tag{2.5}$$

To obtain the spectrum, we need to diagonalize Hamiltonian 2.4. Since this system is translationally invariant, performing a Fourier transform on operators C_A and C_B is guaranteed to decouple its constituent equations. To avoid excessive notation, we will identify operators $C_{A|B}$ and their Fourier transforms with the same symbol. Then, we can write

$$C_A(\mathbf{r}) = \frac{1}{\sqrt{N}} \sum_{\mathbf{k}} C_A(\mathbf{k}) e^{i\mathbf{k}\cdot\mathbf{r}}, \quad C_B(\mathbf{r}) = \frac{1}{\sqrt{N}} \sum_{\mathbf{k}} C_B(\mathbf{k}) e^{i\mathbf{k}\cdot\mathbf{r}}. \tag{2.6}$$

Replacing 2.6 in Hamiltonian 2.4 yields the following expression:

$$H = -t \sum_{\boldsymbol{\delta},\mathbf{k}} e^{i\mathbf{k}\boldsymbol{\delta}} C^\dagger_A(\mathbf{k}) C_B(\mathbf{k}), \tag{2.7}$$

where we used the relation $\frac{1}{N}\sum_{\mathbf{r}} e^{i(\mathbf{k}-\mathbf{k}')\cdot\mathbf{r}} = \delta_{\mathbf{k},\mathbf{k}'}$ to fix one summation index. We can further simplify this expression rewriting it using matrix notation. Let $\psi(\mathbf{k}) = [C_A(\mathbf{k}), C_B(\mathbf{k})]^T$. Then, we can write Hamiltonian 2.4 as

$$H = \sum_{\mathbf{k}} \psi^T(\mathbf{k}) h(\mathbf{k}) \psi(\mathbf{k}), \tag{2.8}$$

where $h(\mathbf{k})$ is the Bloch Hamiltonian:

$$h(\mathbf{k}) = \begin{bmatrix} 0 & f(\mathbf{k}) \\ f^*(\mathbf{k}) & 0 \end{bmatrix}, \tag{2.9}$$

where $f(\mathbf{k}) := -t\sum_{\boldsymbol{\delta}} e^{i\mathbf{k}\cdot\boldsymbol{\delta}}$. The two modes of the Bloch Hamiltonian 2.9 have dispersions

$$E_{\pm}(\mathbf{k}) = \pm|f(\mathbf{k})| = \pm t\sqrt{3 + 2\cos\left(k_y a\right) + 4\cos\left(\frac{1}{2}k_y a\right)\cos\left(\frac{\sqrt{3}}{2}k_x a\right)}. \tag{2.10}$$

The first Brillouin zone, the spectrum through high-symmetry points, and also throughout the two-dimensional Brillouin zone are shown in Fig. 2.2 (a), (b) and (c) respectively. In subpanel (a) K and K' represent the two non-equivalent vertices of the hexagon that constitutes the Brillouin zone (by non-equivalent we mean that they can not be connected through reciprocal lattice translations of vectors $\mathbf{b}_1$ and $\mathbf{b}_2$, analogous to sites A and B in the real-space lattice), Γ the center of the first Brillouin zone with $\mathbf{k} = 0$, and M is the middle points between points K and K'. Notice the linear dispersion in the vicinity of points K and K', which are called the *Dirac points* for reasons that will become clear soon. In addition, the region of the bands where the dispersion is linear is often referred to as the *Dirac cones*.

Of special importance for this work is the low-energy theory of graphene. In this carbon allotrope, five of the six available electrons are locked in the $1s$ and $2sp^2$ orbitals and therefore only one $2p_z$ free electron is available per site (to be precise, each carbon atom provides only three out of the six available states in the $2sp^2$ orbitals, the remaining three states are filled with electrons from the three neighboring carbon atoms when forming σ bonds). Recall that the unit cell of graphene has two non-equivalent sites A and B, and therefore we have two spin-degenerate modes available per unit cell. In conclusion, at zero temperature the lower hole band is fully filled, the higher electron band is empty, and the Fermi level lies right in the middle, where the bands cross at the Dirac points.

We calculate the low-energy spectrum of graphene via Taylor-expansion of function 2.10 around its zero-valued points $|f(\mathbf{k})| = 0$. This leads to the following six roots of f:

$$\mathbf{k}_{1,2} = \pm\frac{4\pi}{3a}[0,1], \quad \mathbf{k}_{3,4} = \pm\frac{4\pi}{3a}\left[\frac{\sqrt{3}}{2}, \frac{1}{2}\right], \quad \mathbf{k}_{5,6} = \pm\frac{4\pi}{3a}\left[\frac{\sqrt{3}}{2}, -\frac{1}{2}\right]. \tag{2.11}$$

We can now see clearly that the Dirac points, *i.e.* the six roots of f, indeed correspond to the vertices of the first Brillouin zone. We can select a pair of non-equivalent Dirac points $\mathbf{k}_1$ and $\mathbf{k}_2$,

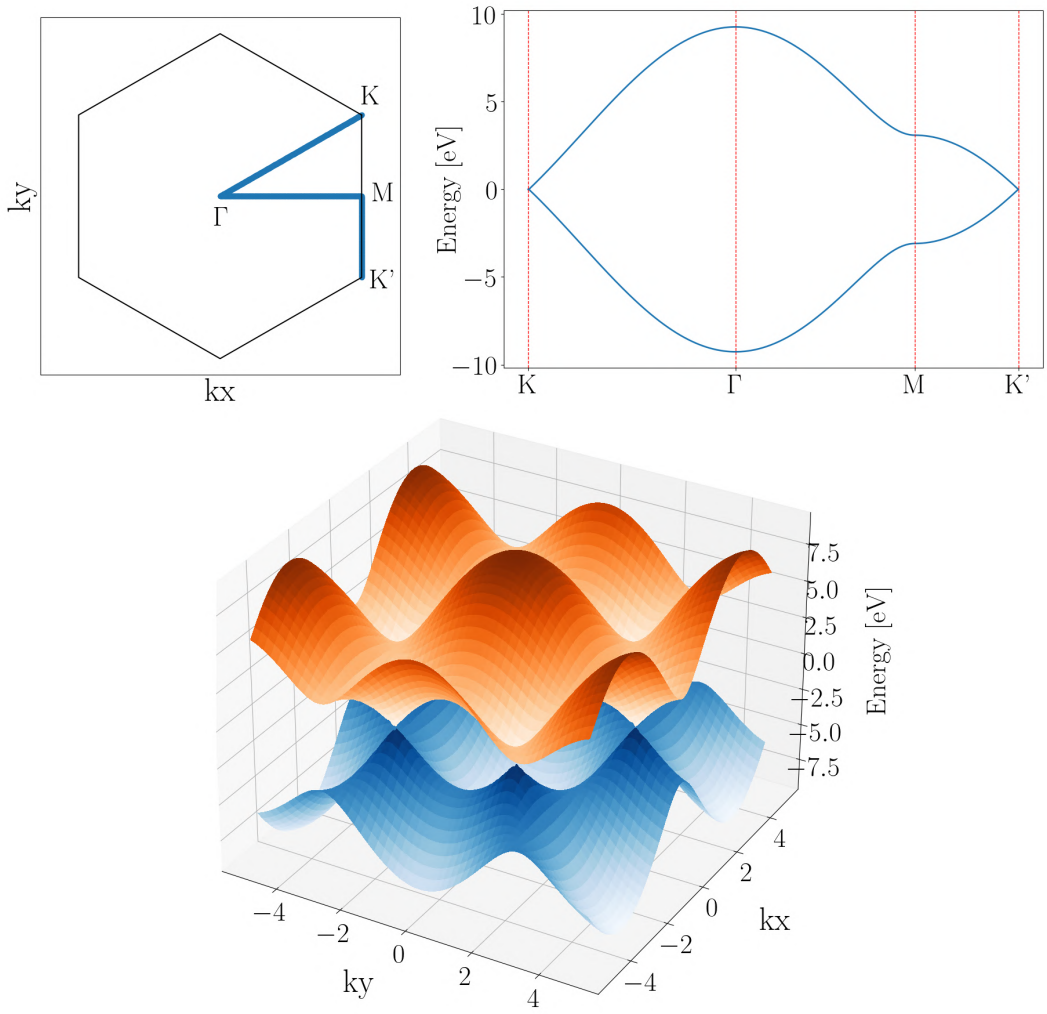

Figure 2.2: Graphene spectrum: (a) First Brillouin Zone and position of high-symmetry points, (b) spectrum through high-symmetry points and (c) spectrum throughout the Brillouin zone

and the rest are not necessary due to the C_3 symmetry of graphene (they can be connected with reciprocal lattice translations $\mathbf{b}_1$ and $\mathbf{b}_2$). Moreover, notice that Hamiltonian 2.9 has inversion symmetry ($h(\mathbf{k}) = \sigma_1 h(-\mathbf{k})\sigma_1$) and time-reversal symmetry ($h(\mathbf{k}) = h(-\mathbf{k})$). Suppose we wanted to add a bandgap $V(\mathbf{k})$ without breaking these symmetries. The addition of $V(\mathbf{k})$ in Eq. 2.9 adds a diagonal term in the Hamiltonian. However, the combination of inversion and time-reversal symmetries forces the constrains

$$\begin{cases} V(-\mathbf{k})^* = V(\mathbf{k}), \\ V(-\mathbf{k}) = -V(\mathbf{k}). \end{cases} \tag{2.12}$$

Therefore $V(\mathbf{k})$ has to be imaginary. But this breaks the condition of hermicity, since no Hermitian matrix can have imaginary terms on its diagonal. Thus the only physical solution

is $V(\mathbf{k}) = 0$, and we find that the Dirac points in graphene are protected by inversion and time-reversal symmetry. We emphasize that it is a combination of these two symmetries which protects the Dirac points.

The first-order Taylor expansion of equation 2.10 at points $\mathbf{k}_1$ and $\mathbf{k}_2$ yields

$$f(\mathbf{k}_1 + \mathbf{k}) \approx -\frac{\sqrt{3}}{2} ta e^{-\frac{2\pi}{3} i} (k_y - i k_x), \tag{2.13}$$

and

$$f(\mathbf{k}_2 + \mathbf{k}) \approx -\frac{\sqrt{3}}{2} ta e^{-\frac{2\pi}{3} i} (k_y + i k_x). \tag{2.14}$$

We can get rid of the constant phase terms using $U(1)$ gauge invariance of the ψ wavefunctions. This leaves the relative phase between the two sublattices unchanged, and is therefore physically inconsequential. Furthermore, it will be convenient to our description of twisted bilayer graphene to express this relation in polar coordinates $k, \theta_{\mathbf{k}}$, where $k = ||\mathbf{k}||$ is the modulus and $\theta_{\mathbf{k}} = (k_x + i k_y)/k$ the argument of the quasi-momentum. We can further simplify this expression by performing a rotation of $-\pi/2$ around the k_z-axis, which is equivalent to replacing $k_x \to k_y$ and $k_y \to -k_x$ in function f. Finally, replacing the low-energy dispersion of f in the Bloch Hamiltonian 2.9 leads to equations

$$h(\mathbf{k} + \mathbf{k}_1) = h_1(\mathbf{k}) = -\hbar v_F \begin{bmatrix} 0 & -k_x - i k_y \\ -k_x + i k_y & 0 \end{bmatrix} = \hbar v_F k \begin{bmatrix} 0 & e^{i\theta_{\mathbf{k}}} \\ e^{-i\theta_{\mathbf{k}}} & 0 \end{bmatrix}, \tag{2.15}$$

$$h(\mathbf{k} + \mathbf{k}_2) = h_2(\mathbf{k}) = -\hbar v_F \begin{bmatrix} 0 & k_x - i k_y \\ k_x + i k_y & 0 \end{bmatrix} = -\hbar v_F k \begin{bmatrix} 0 & e^{-i\theta_{\mathbf{k}}} \\ e^{i\theta_{\mathbf{k}}} & 0 \end{bmatrix}. \tag{2.16}$$

where $v_F = \frac{\sqrt{3} ta}{2\hbar}$ is the Fermi velocity at the Dirac point, and $\mathbf{k}$ now represents the quasi-momenta where the linear expansion is appropriate. Hamiltonians 2.15 and 2.16 are called the Dirac Hamiltonians, since they describe free, massless relativistic (Dirac) particles in two dimensions with velocity v_F. The right-sided polar expression will be useful later to construct the low-energy band theory of twisted bilayer graphene, because it is trivial to perform a rotation of a graphene sheet in these coordinates.

Before we move on, we will briefly discuss the *chiral symmetry* of graphene. The A and B sublattices of graphene, related by C_3 symmetry, are physically identical, meaning that they have the same electronic properties. The labels attached to them are only necessary due to the particular geometry of the honeycomb lattice, which requires two sites in its smallest unit cell. Furthermore, for the low-energy theory (*i.e.* for quasi-momenta in the vicinity of the Dirac points) the Bloch Hamiltonians 2.15 2.16 are linearly coupled in momentum. This means that we can rewrite these Hamiltonians using a *pseudo-spin* representation:

$$h(\mathbf{k} + \mathbf{k}_{1|2}) \approx \pm \hbar v_F \boldsymbol{\sigma} \cdot \mathbf{k}, \tag{2.17}$$

where $\boldsymbol{\sigma} = [\sigma_x, \sigma_y]$ is the pseudo-spin operator. Now, $\boldsymbol{\sigma}$ is restricted to the $xy-$plane, and therefore we can define the *winding number* of points in $k-$space. Any closed curve C in a two-dimensional vector space can be classified by the value of the winding number ξ, which corresponds to the number of times the vector rotates when it travels one loop through C (the sign is determined by the direction of rotation). In our case, this vector is the pseudo-spin, and ξ can thus be defined using the expectation value of the pseudo-spin operator $\langle \boldsymbol{\sigma} \cdot \frac{\mathbf{k}}{k} \rangle$. At point K we find that $\xi_+ = +1$, and at point K' $\xi_- = -1$ instead.

Previously we mentioned that the Dirac points in graphene are protected by PT symmetry (inversion and time-reversal). The points where the bands touch (the Dirac points) cannot disappear under any continuous deformation that preserves PT symmetry. This protection can also be explained in topological terms using the winding number. Any closed curve with a non-zero winding number must necessarily have a point inside with zero pseudo-spin, which implies that the energy is also equal to zero, given that the pseudo-spin Hamiltonian 2.17 is just the pseudo-spin operator times a constant. This topological perspective sheds light on an interesting phenomenon: two points of opposite winding number can "cancel" one another. Suppose we have a closed curve C, that contains inside of it two points of opposite winding number. Then, the resulting winding number of this curve is equal to zero, and the Dirac points are no longer protected. This fascinating phenomenon in graphene is called pair-annihilation of Dirac points [49].

While graphene itself does not have a chiral topology in the conventional sense (like the quantum Hall or Chern insulator) its sublattice symmetry plays a crucial role in defining its topological properties, particularly in the context of topologically protected edge states and the Dirac-point degeneracy. Sublattice symmetry can enforce zero-energy edge states in certain geometries. In graphene, these correspond to so-called *zigzag edge* terminations. However, unlike the edge states in Chern insulators, the zero-energy edge states are localized and non-propagating, unless PT symmetry or sublattice symmetry is broken. Remarkably, a staggered magnetic flux that averages to zero in each unit cell but breaks sublattice and time-reversal symmetries can make turn graphene into a Chern insulator. Haldane's topological model of graphene was the pioneering theoretical work that showed that a two-dimensional system can induce the quantum Hall effect without the reliance on Landau levels [50]. It demonstrates that, in the realization of topological phases, time-reversal symmetry breaking is more fundamental than external magnetic fields [51].

P. R. Wallace in 1946 was the first researcher to study the band structure of graphene, and to highlight the unusual semimetallic spectrum of this incredible material [52]. At the time, the idea of a purely two-dimensional material seemed unrealistic, and even Wallace thought of his analysis only as a starting point to study graphite, a material that was important for the construction of nuclear reactors. In a revolutionary paper published in 2004, Andre Geim, Konstantin Novoselov *et al.* showed that atoms-thick layers of this material could indeed be

procured and kept in stable conditions [1]. For this, they were awarded the Nobel prize in 2010. Since then graphene has been the subject of a vast amount of research that is still ongoing [53]. Remarkably, the discovery of twisted bilayer graphene in 2018 by Yuan Cao *et al.* [14, 15] shows that this simple carbon material can still surprise the materials science community, despite long decades of intense research.

2.1.1 Twisted monolayer graphene

Before developing the theory of bilayer graphene, it is convenient to stop first to consider the effect that a rotation around the $z-$axis has on the spectrum of monolayer graphene, defined in the basis of the non-rotated system. Let us start with a Bloch Hamiltonian 2.9, and notice that a real-space rotation modifies the spectrum through functions f and f^*. Moreover, these functions depend only on the inner product of vectors $\mathbf{k}$ and $\boldsymbol{\delta}_i$. Thus, a clockwise rotation of vectors $\boldsymbol{\delta}_i$ is equivalent to an anti-clockwise rotation of the crystal momentum $\mathbf{k}$. Therefore, we can write the rotated $K-$point Dirac cone described by Hamiltonian 2.15 (*i.e.* the linear dispersion near the K Dirac point) as

$$h_\theta(\mathbf{k}_1+\mathbf{k}) = \hbar v_F k \begin{bmatrix} 0 & e^{i(\theta_{\mathbf{k}}-\theta)} \\ e^{-i(\theta_{\mathbf{k}}-\theta)} & 0 \end{bmatrix}, \tag{2.18}$$

where θ is the angle of rotation. The effect on the second K' Dirac cone, described by Eq. 2.16, is analogous.

2.2 Bilayer Graphene

The sp^2 orbitals of the carbon atoms in graphene, formed by the hybridization of the $2s$, $2p_x$ and $2p_y$ orbitals, form strong *intralayer* covalent σ bonds. These σ bonds in the $xy-$plane make graphene a remarkably strong material. The remaining p_z orbitals couple the sites only weakly in the out-of-plane direction, through van der Waals forces. This weak out-of-plane coupling of the layers is the reason why graphite crumbles so easily, as the layers peel away from each other with ease. However, the weak *interlayer* coupling of the layers can have very consequential effects on the electronic properties of graphene-based systems. In this section we discuss a material formed by stacking two layers of graphene on top of each other, called *bilayer graphene*, while preserving the translational symmetry of the constituent graphene layers. The p_z orbitals in this configuration form weaker σ bonds, with a bond length of $d = 3.35\,\text{Å}$, when two sites are stacked directly on top of each other. Sites stacked in this way have an interlayer hopping integral of $V_{pp\sigma} \approx 0.17\,\text{eV}$, which is about an order of magnitude lower than the value of the intralayer nearest-neighbor hopping in graphene.

There are two common stable configurations of bilayer graphene: $AA-$ and $AB-$stacking (the latter also called Bernal-stacking). The former is created by stacking the graphene layers exactly

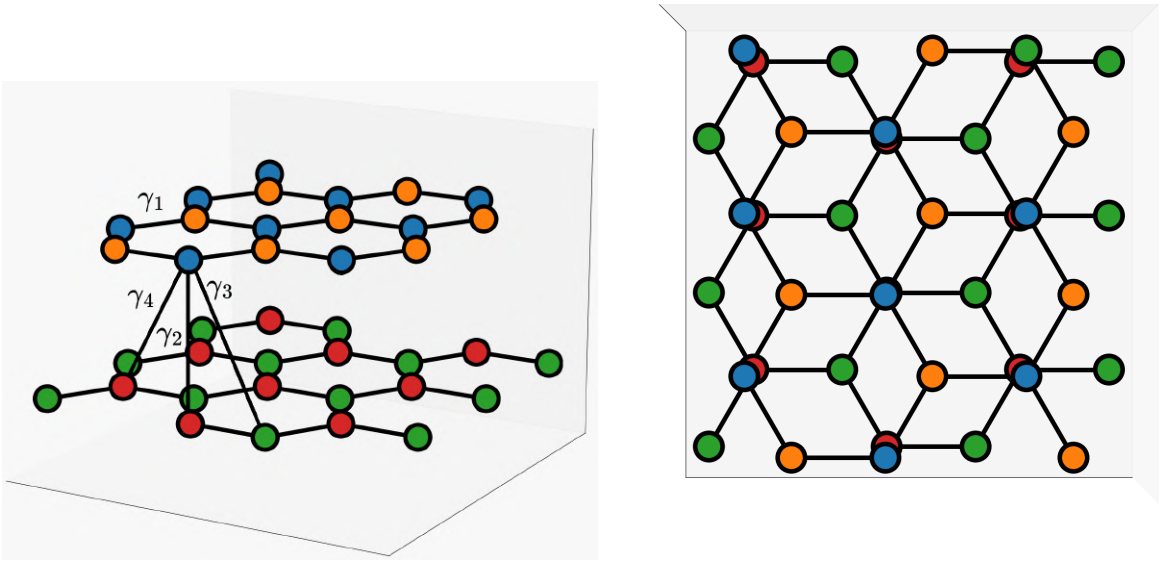

(a) (b)

Figure 2.3: Lattice structure of AB-stacked bilayer graphene (a) view from the side and (b) view from the top.

on top of each other, such that all sites have the same position in the $xy-$plane, and the only difference between the graphene sheets is the interlayer distance separating them. This bilayer configuration has exactly the same two-dimensional crystal structure of graphene, but with four sites in each unit cell instead of two. The two sites with an A label in both graphene sheets are typically labeled AA, and the other two BB. Bernal bilayer graphene is created instead by stacking a pair of sites of different label on top of each other (A and B for instance, which explains the AB label). $AB-$stacked bilayer graphene can also be created from the AA configuration by rotating one of the layers by an angle of $\pi/3$ around an axis that connects any two stacked atoms (AA or BB). Since graphene has C_3 symmetry, the rotated sheet is essentially unchanged. However, this results in the swapping of the labels $A \leftrightarrow B$ in the rotated layer. Moreover, the rotation causes half of the sites in the rotated layer to be displaced towards the middle of the hexagon of the unrotated layer. Of these two configurations, $AB-$stacked bilayer graphene is the more stable. We show the AB configuration in Fig. 2.3.

In contrast to monolayer graphene, the interlayer coupling of bilayer graphene can not be described accurately with a nearest-neighbor tight-binding model, particularly in the case of AB stacking. To obtain an accurate description of the spectrum we need to consider farther overlap integrals, even if we limit ourselves to the description of the low-energy theory. To explain this, recall that in graphene the nearest-neighbor hopping model is accurate due to a combination of the rapid exponential decay of the overlap integrals, and the screening of distant

hoppings by intermediate sites. This is a consequence of the two-dimensional structure of the lattice, because these intermediate sites get "in the way" between any pair of distant sites, so to speak. However, in bilayer graphene sites located in different layers are separated by the interlayer distance, reducing the screening. As a consequence, the effective exponential decay of the interlayer hopping amplitude is weaker than the decay of the intralayer hopping amplitude.

Despite the weaker screening, the rapid exponential decay of the p_z orbitals, relative to the interlayer distance between sites, allows us to accurately describe the band structure of bilayer graphene with second- and third-nearest neighbor tight-binding models. The most frequently used model incudes up to third-nearest neighbor interlayer hoppings, and is sometimes referred to as the 4γ model, due to the labeling of the hoppings (one intralayer hopping γ_1 and three interlayer hoppings γ_2, γ_3 and γ_4) [54]. We show these four hoppings in Fig. 2.3 (a). For most purposes this approximation is sufficient, particularly for the low-energy theory. However, we note that the inclusion of γ_4 hoppings breaks inversion symmetry, which is inconsequential for this work.

The unit cell of bilayer graphene, in both configurations, can be constructed by simply adding two stacked graphene unit cells. Regardless of the stacking order, the unit cell has the same translation vectors as graphene, and thus the Brillouin zone is the same. The unit cell has now four sites, and therefore bilayer graphene has four spin-degenerate bands. We show the band structure of bilayer graphene, of both the AA and AB configurations, in Fig. 2.4. We used the following parametrization [54]: $\gamma_1 = 3.09\text{eV}$, $\gamma_2 = 0.39\text{eV}$, $\gamma_3 = 0.04\text{eV}$, $\gamma_4 = 0$ (this last coupling parameter is $\approx 0.01\,\text{eV}$, we omit it in this work since it has no discernible effect on the low-energy theory). The four bands are only slightly distorted by the coupling of the layers, regardless of the stacking configuration. In agreement with this, the zero-energy conductivity of bilayer graphene is twice that of monolayer graphene, and has the same shot noise [4, 55]. However, notice that the low-energy theory has one significant difference between these two configurations: in AB-stacked bilayer graphene we observe a parabolic dispersion of the bands at the Dirac points, and a Dirac-point bandgap of $\Delta E = \gamma_1$ between two modes. Thus, only two modes are gapless, and the Dirac massless linear dispersion relation is lost. On the contrary, in the AA stacking configuration we find that the low-energy dispersion is essentially identical to that of two independent monolayers of graphene, only slightly displaced in $k-$space. The linear dispersion is preserved, and we have two Dirac points at zero energy.

Since the bands are mostly unaffected by the interlayer coupling, bilayer graphene preserves most of the remarkable properties of monolayer graphene. To name just a few: excellent conductivity; the possibility to tune electrical properties by changing the charge carrier density; high thermal conductivity; mechanical stiffness; strength and flexibility [54]. Unsurprisingly, graphene and bilayer graphene are already utilized in many applications in research and industry [5]. However, the semi-metallic nature of monolayer graphene constitutes a significant limitation for optoelectronic applications. In this regard, bilayer graphene has a significant

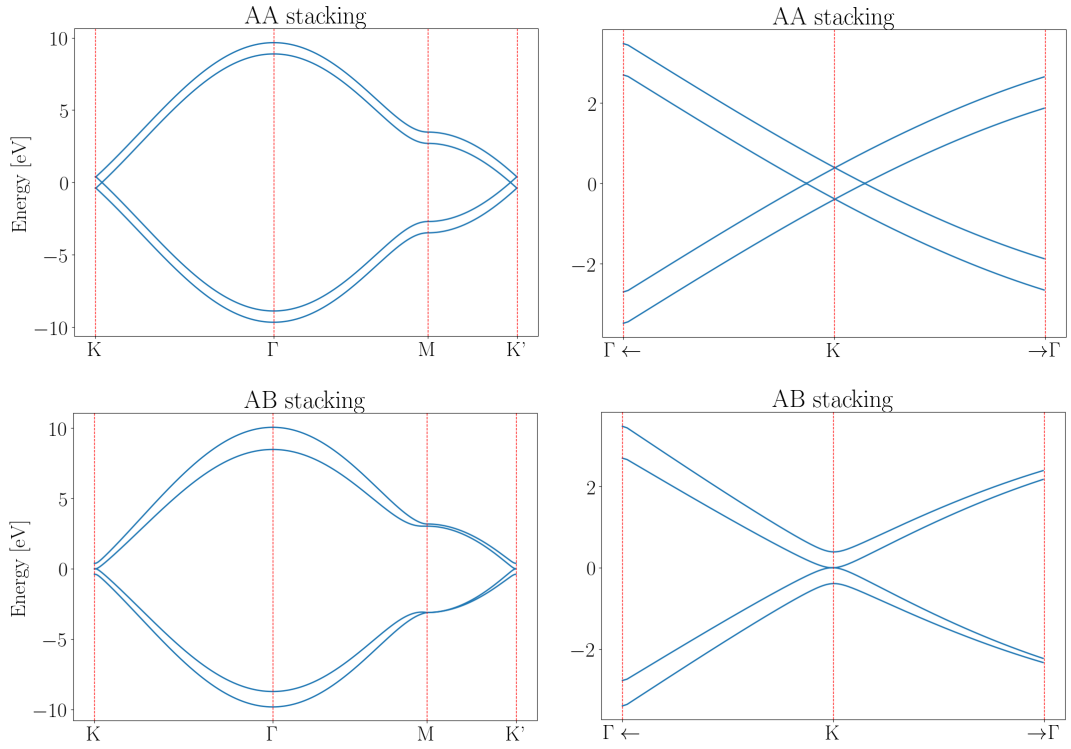

Figure 2.4: Spectrum of AA- and AB-stacked bilayer graphene through high-symmetry points K, Γ, M and K' (see Fig. 2.2 to locate these points in the reciprocal lattice).

advantage: a bandgap of up to $\approx 300\,\text{meV}$ can be opened though doping or interlayer gating. This offers a plethora of new possibilities for the development of electronic applications. Indeed, the bandgap in this material has already been used to create composite nanoparticles with interesting properties [2]. And yet, a small twist in one layer relative to the other goes a step further and fundamentally changes the electronic properties of bilayer graphene. A weakly coupled system transforms into a strongly correlated material with truly unusual characteristics by this seemingly innocuous twist. We will now discuss this new material, twisted bilayer graphene.

2.3 Twisted Bilayer Graphene

Twisted bilayer graphene can be formed starting with a layer of $AA-$ or $AB-$stacked bilayer graphene, and then twisting one of the graphene sheets relative to the other around a fixed point in space. The twisting creates a moiré pattern, as illustrated in Fig. 2.5. The emerging moiré superlattice inherits the hexagonal lattice symmetry of graphene, and therefore we can identify two moiré sublattices AA and AB/BA, which represent the points where atoms in sublattices A and B are stacked on top of each other. AB and BA are essentially indistinguishable, and they can be treated as the same sublattice. However, notice that swapping the graphene sheets

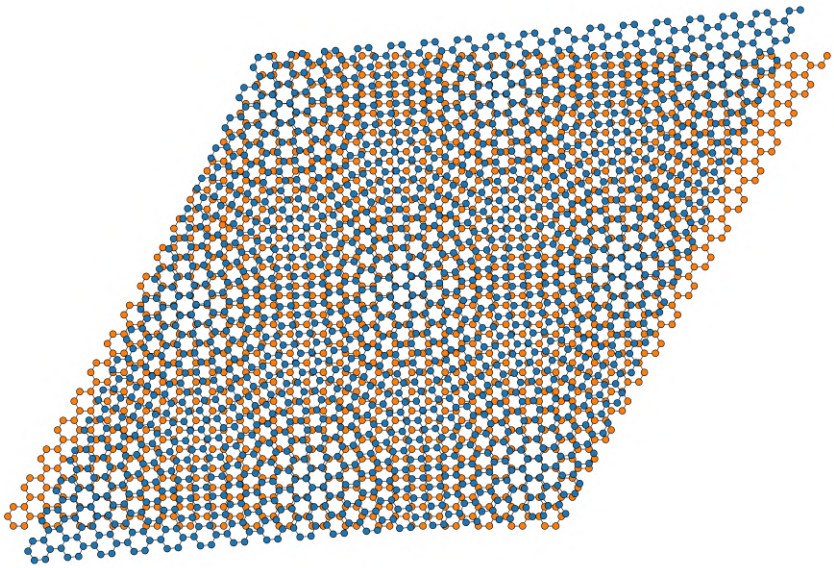

Figure 2.5: Twisted bilayer graphene lattice structure. Different colors indicate different graphene sheets.

changes the labels $AB \to BA$. This seemingly trivial observation has important consequences, because it implies an additional *layer inversion symmetry* present in twisted bilayer graphene.

The area surrounding sites AA correspond to the section of the moiré lattice where the average distance between sites in different layers is the lowest, essentially equal to the interlayer distance between the graphene sheets. We can locate these areas in Fig. 2.5, these are the regions where the orange sites are mostly blocked from view by the blue sites. On the other hand, the vicinities of AB/BA sites have on average the largest distance between sites in different layers. This moiré-periodic inhomogeneity of the average neighboring distance between sites of different layers implies that the effective interlayer coupling of the layers is not uniform. Lattice relaxation induces a *corrugation* in the out-of-plane direction. Theoretical studies predict that the AA sites have a wider interlayer spacing than AB/BA sites [56, 57]. This has important consequences for the electronic properties of twisted bilayer graphene, because it leads to significant band distortion of the low-energy bands. In floating samples, the corrugation amplitude is approximately a tenth of the interlayer distance d of $AB-$stacked bilayer graphene [56]. Such corrugation can be quite substantial, leading to the widening of the quasi-flat low-energy bands characteristic of small-angle twisted bilayer graphene by a factor of ≈ 100. However, real samples of twisted bilayer graphene are placed in the middle of substrates, typically made of layered hexagonal boron nitride hBN, to stabilize the lattice structure. The corrugation in the out-of-plane direction in real samples is estimated to be only $\approx 1\%$ of d [24]. Even this lower value has a significant effect on the low-energy band structure of twisted bilayer graphene at small twist angles.

We could naively anticipate from our discussion of the low-energy theory of bilayer graphene, that twisted bilayer graphene will have a different low-energy band structure depending on the

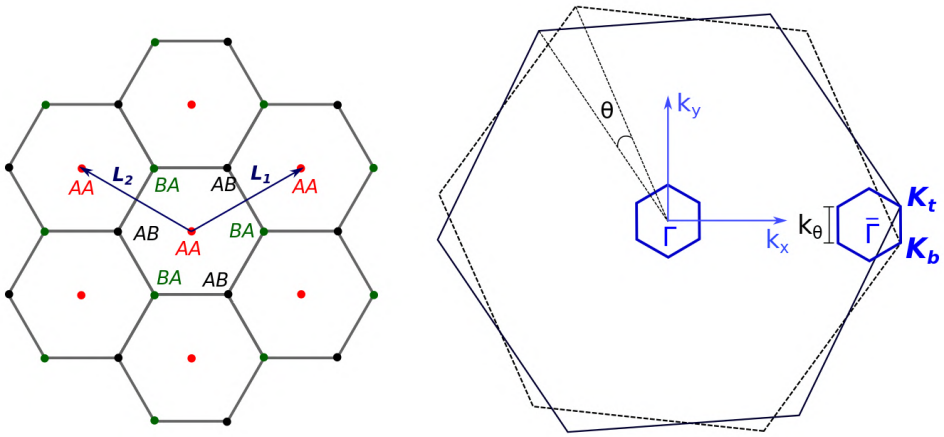

Figure 2.6: Twisted bilayer graphene: (left) moiré superlattice. Also shown are the sublattices AB, BA and the points AA; (right) Brillouin zone of rotated graphene (big hexagons in black) and the moiré Brillouin zone that emerges from twisting (small honeycomb in blue). K_t and K_b represent the rotated K points in the top and bottom layers correspondingly, and k_θ is the nearest-neighbor constant of the moiré reciprocal lattice.

starting configuration ($AA-$ or $AB-$ bilayer graphene at zero twisting). This intuition turns out to be incorrect, which is easy to understand if we carefully observe the physical structure of a twisted bilayer graphene flake. The initial stacking only swaps the position of sites AA, AB and BA in the lattice, and therefore has no effect on the periodic system. This of course breaks in the limit $\theta \to 0$, because the moiré lattice constant diverges to infinity. Nonetheless, for any finite twist angle we find that the initial configuration of the bilayer system does not alter the physical configuration, or the electronic properties, of the moiré superlattice. We also note that since the AA and AB bilayer graphene configurations can be connected with a twist of $\theta = \pi/3$, the twist angle is uniquely defined within the range $\theta \in [0, \pi/3)$. Because of these considerations, without the loss of generality throughout this work we use the AA configuration of bilayer graphene at zero-twisting. However, we note that when considering finite systems with just a few moiré unit cells, the position of the moiré sublattices could be consequential. This is because the Dirac electrons in small-angle twisted bilayer graphene are often localized in the middle of the AA stacking regions [56].

We show the hexagonal superlattice in Fig. 2.6 (a). $\mathbf{L_1}$ and $\mathbf{L_2}$ in this figure represent the moiré translation vectors. We also show the first Brillouin zones of graphene and twisted bilayer graphene in Fig. 2.6 (b). The big hexagons in black represent the graphene Brillouin zones, and the blue small hexagon the emerging moiré Brillouin zone. Since we start from $AA-$stacked bilayer graphene at zero-twisting, all Dirac points are located in the same position in $k-$space (for the moment ignoring the shift in the position of the Dirac point due to the coupling of the layers in $AA-$stacked bilayer graphene). We label the Dirac K points in the bottom and top graphene lattices as K_b and K_t respectively, and the other Dirac K' points as K'_b and K'_t. The

nearest-neighbor distance between sublattices AA and AB in the moiré $k-$space is $k_\theta = G/\sqrt{3}$, where $G = |\mathbf{G}|$ is the primitive translation length of the moiré reciprocal lattice. In this figure we use $\bar{\Gamma}$ to distinguish the center of the moiré Brillouin zone from the center of the Brillouin zones of both graphene sheets, which is identified instead as Γ. To avoid excessive notation, from now on we will use Γ to identify the center of the moiré Brillouin zone.

In general, the moiré superlattice is not strictly periodic, but only quasi-periodic. The *commensurate* twist angles, for which the periodicity condition is fulfilled, constitute an infinite but countable set of points, and have the following form [58]:

$$\cos\theta = \frac{3m^2 + 3mr + r^2/2}{3m^2 + 3mr + r^2}, \tag{2.19}$$

where m and r are coprime positive integers. For commensurate twist angles the moiré lattice constant L_m is well-defined. Setting $r = 1$ in Eq. 2.19, L_m can be written as

$$L_m = \frac{a}{2\sin\frac{\theta}{2}}, \tag{2.20}$$

where a is the lattice constant of monolayer graphene. We recall from the introduction to this chapter that we call certain twist angles "magic" because of the extraordinary properties that twisted bilayer graphene was shown to exhibit at them. The first one from largest to smallest, and the first discovered experimentally, is $\theta_m \approx 1.05°$. At the first magic-angle θ_m we find that the moiré translation length is $L_m \approx 15\,\text{nm}$, so approximately two orders of magnitude larger than that of graphene. There are more than one magic angle, but all of them are very small $\theta \approx 1°$. Looking at Eq. 2.20, we can now appreciate the difficulty of using *ab initio* methods to calculate the electronic properties of magic-angle twisted bilayer graphene. Even at the largest magic angle θ_m the unit cell contains about twenty thousand sites! With access to a cluster of computers, density functional theory calculations are still capable of calculating the spectrum of such large systems. However, the simulation of a finite system with just a few tens of moiré unit cells is completely outside the capabilities of this method. For this reason, *ab initio* methods and density functional theory calculations are unable to study quantum transport in magic-angle twisted bilayer graphene systems.

2.3.1 Continuum model

Due to the very large size of the moiré unit cell at small twist angles, where the "magic" occurs, it is not surprising that the discovery of magic-angle twisted bilayer graphene was experimental rather than theoretical. Even now, many years after its discovery, we do not have an analytical model that fully accounts for the rich variety of exotic phenomena observed in this material. The search for a comprehensive theoretical model is still ongoing, and we note that among the most promising theoretical works in recent years is a topological heavy fermion model proposed by Zhi-Da Song and Andrei Bernevig in 2022 [59]. However, even before the experimental discovery

of the magic-angle, an approximate long-wavelength model existed that described the most important properties of the moiré bands of small-angle twisted bilayer graphene. This *Dirac continuum model* was developed by Rafi Bistritzer and Allan H. MacDonald in 2011 [12]. It is a surprisingly simple yet accurate approach, it accounts for the flattening of the moiré bands within an order of magnitude of precise experimental measurements and predicts the appearance of critical points in the moiré bands near the Fermi level. Though it falls short of explaining all the characteristic properties of magic-angle twisted bilayer graphene, it provides useful insight into the changes in the band structure that take place when the twist angle approaches a magic one.

In the limit of small angles $\theta \approx 1^\circ$, the low-energy physics of twisted bilayer graphene is largely independent of the geometric details of the lattice, so that the quasi-periodicity of the moiré pattern is effectively inconsequential [12]. In addition, notice that Eq. 2.19 implies that the set of commensurate twist angles has an accumulation point at $\theta = 0$. This means that near the first magic angle $\theta \approx 1^\circ$ the angular separation between commensurate twist angles is quite small $\delta\theta \approx 0.03^\circ$. Therefore, in this small-angle regime we can neglect the condition of periodicity and assume that all twist angles are commensurate, and consider θ a continuous parameter.

Let $\mathbf{L}_{1,2}$ be the following moiré translation vectors:

$$\mathbf{L}_{1,2} = L_m \left[\pm \frac{\sqrt{3}}{2}, \frac{1}{2} \right]. \tag{2.21}$$

where L_m is given by Eq. 2.20. The corresponding moiré reciprocal vectors $\mathbf{G_i}$ are therefore

$$\mathbf{G}_{1,2} = \frac{8\pi}{\sqrt{3}L_m} \left[\pm \frac{1}{2}, \frac{\sqrt{3}}{2} \right] = G \left[\pm \frac{1}{2}, \frac{\sqrt{3}}{2} \right]. \tag{2.22}$$

Let the Dirac point K of the unrotated graphene layers be located at position $\mathbf{k} = \frac{4\pi}{3a}[1,0]$ in reciprocal space. The low-energy dispersion of this point in both layers (before interlayer coupling is taken into consideration) is then described by the Bloch Hamiltonian 2.15. We then perform a rotation of the top layer by an angle $\theta/2$, and the bottom layer by an angle $-\theta/2$, according to the prescription given in Eq. 2.18. Furthermore, let us consider the extended Hilbert space $\mathscr{H} = \mathscr{H}_t \bigoplus \mathscr{H}_b$ that includes the top and bottom Bloch Hamiltonians for this Dirac point. The decoupled Hamiltonian for both layers can then be written as

$$H^0(\mathbf{k}) = \begin{bmatrix} h_{\theta/2} & 0 \\ 0 & h_{-\theta/2} \end{bmatrix} = \hbar v_F k \begin{bmatrix} 0 & e^{i(\theta_{\mathbf{k}} - \theta/2)} & 0 & 0 \\ e^{-i(\theta_{\mathbf{k}} - \theta/2)} & 0 & 0 & 0 \\ 0 & 0 & 0 & e^{i(\theta_{\mathbf{k}} + \theta/2)} \\ 0 & 0 & e^{-i(\theta_{\mathbf{k}} + \theta/2)} & 0 \end{bmatrix}. \tag{2.23}$$

In the limit of small angles the moiré translation length L is much larger than graphene's translation length a. The Brillouin zone in the moiré reciprocal lattice is proportionately smaller,

which we can visualize in Fig. 2.6 comparing the sizes of the graphene and moiré Brillouin zones. Because of this, particle transfers between the layers are heavily suppressed except for the nearest-neighbor nodes in the moiré reciprocal lattice [12]. Thus, as a first approximation we can consider a nearest-neighbor tight-binding model, defined now in quasi-momentum space, and neglect more distant hoppings.

In momentum space, the process by which a Dirac electron in a K_b site of the bottom lattice hops to its three nearest neighbors in the top layer is given by the following relation

$$T_{\mathbf{k}} = c^{\dagger}_{t,\mathbf{k}} \sum_{n=0}^{2} T_n c_{b,\mathbf{k}-\mathbf{G^n}}, \tag{2.24}$$

where:

- $c^{\dagger}_{t/b,\mathbf{k}}$ are creation fermionic operators of Dirac particles in the vicinity of a single Dirac point with momentum $\mathbf{k}$ in the top and bottom layers,
- vectors $\mathbf{G}^i$, $i = 0,1,2$, connect the bottom K_b node to its neighboring top K_t nodes: $\mathbf{G}^0 = k_\theta[0,1]$, $\mathbf{G}^1 = k_\theta[-\sqrt{3}/2,-1/2]$ and $\mathbf{G}^2 = k_\theta[\sqrt{3}/2,-1/2]$ (recall that $k_\theta = G/\sqrt{3}$ is the nearest-neighbor distance in the moiré reciprocal lattice, and $G = |\mathbf{G_{1,2}}|$ is the moiré reciprocal translation length),
- T_n are the four-component tensors that represent the hopping amplitudes in the moiré reciprocal lattice. Each tensor takes into account the AA, AB/BA degrees of freedom.

Figure 2.7 shows the emerging moiré reciprocal lattice. Sites with label t represent the top Dirac points and b the bottom ones. The first continuum models of twisted bilayer graphene assumed that the hopping amplitudes were equal, *i.e* that hoppings between sites AA and AB/BA have the same amplitude, which implies that the moiré lattice is uniformly coupled and therefore not corrugated. However, several studies showed that the lattice undergoes relaxation which leads to a corrugation of the lattice in the out-of-plane direction [56]. AA points were shown to have the widest interlayer spacing, and AB/BA points to have the narrowest. We can incorporate this corrugation effect by setting a different tunneling amplitude in the components of hopping tensors T_n. In addition, since tensors T_n take into account the AA, AB and BA degrees of freedom, their components undergo a phase shift because of the displacement between sublattices. The translation vectors from a site with label AA to a pair of neighboring AB and BA points can be chosen as $(\mathbf{L}_2 - \mathbf{L}_1)/3$ and $-(\mathbf{L}_2 - \mathbf{L}_1)/3$ respectively (see Fig. 2.6). Thus, the phase shifts are $e^{i(\mathbf{L}_2-\mathbf{L}_1)\cdot\mathbf{G}_i}, i = 1,2$.

Following Ref. [57], we write the three tunneling tensors T_n as

$$T_0 = \begin{bmatrix} u & u' \\ u' & u \end{bmatrix}, \quad T_1 = \begin{bmatrix} u & u'e^{i\phi} \\ u'e^{-i\phi} & u \end{bmatrix}, \quad T_2 = \begin{bmatrix} u & u'e^{-i\phi} \\ u'e^{i\phi} & u \end{bmatrix}, \tag{2.25}$$

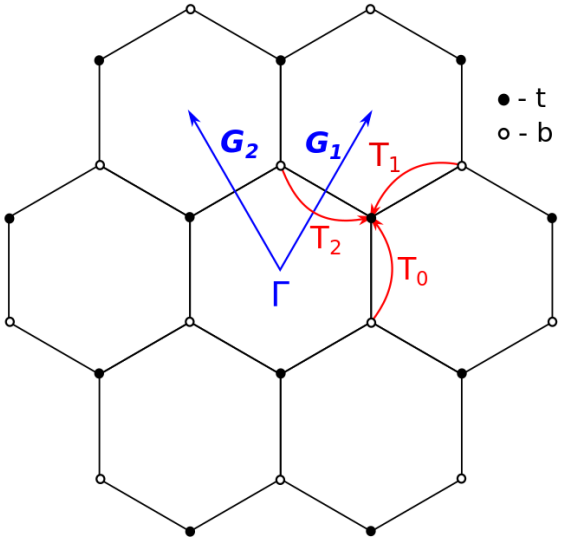

Figure 2.7: Nearest-neighbor reciprocal moiré lattice of twisted bilayer graphene. $\mathbf{G}_i$ correspond to the moiré primitive translations, Γ is the center of the moiré lattice and T_n represent the hopping matrices. Filled nodes with label t correspond to the Dirac point in the top layer, and hollow nodes with label b to the same point in the bottom layer.

where $\phi = 2\pi/3$, $u = 0.0797\,\text{eV}$ and $u' = 0.0975\,\text{eV}$. In the absence of corrugation, *i.e* setting $u = u' \equiv u_0$, the tunneling amplitudes u_0 correspond to the Fourier transform of the real-space tunneling amplitude divided by the unit cell area; $u_0 = t_{\mathbf{k}}/\Omega$. To calculate u and u' in corrugated twisted bilayer graphene, we can assume that the transfer integrals between any pair of p_z orbitals in different layers have a Slater-Koster form, and then use the measured values of corrugation in twisted bilayer graphene lattices to calculate the effective tunneling amplitudes. A detailed calculation is provided in the appendix of Ref. [57].

The coupled Hamiltonian in momentum space cannot be written as a simple matrix, due to the shifting of annihilation operators (see Eq. 2.24). For an succinct description, we can move to the position representation instead. The rotated Hamiltonian in the pseudo-spin description (see Eq. 2.17) can be written as

$$h_\theta(\mathbf{r}) = -v_F\hbar[-i\nabla - \mathbf{k}_{b/t}]\cdot\boldsymbol{\sigma}'_\theta, \tag{2.26}$$

where $\boldsymbol{\sigma}'_\theta = e^{-i\sigma_z/2}\boldsymbol{\sigma}'e^{i\sigma_z\theta/2}$ and $\boldsymbol{\sigma}' = [-\sigma_x, \sigma_y]$. Due to the translational symmetry of the Hamiltonian, the tunneling matrices become trivial:

$$T_{\mathbf{r}} = \sum_{n=0}^{2} e^{i\mathbf{G}^n\cdot\mathbf{r}}T_n. \tag{2.27}$$

This procedure allowed us to establish the description of the Hamiltonian with respect to only one Dirac point K. Recall that K and K' are related via a time-reversal operation T, which in

the pseudo-spin description is equivalent to changing the sign of σ_x: $\boldsymbol{\sigma}' = [-\sigma_x, \sigma_y] \rightarrow \boldsymbol{\sigma} = [\sigma_x, \sigma_y]$. Thus, the Hamiltonian for both Dirac points is:

$$H(\mathbf{r}) = \begin{bmatrix} h_{\theta/2}(\mathbf{r}) & T_{\mathbf{r}} & 0 & 0 \\ T_{\mathbf{r}}^{\dagger} & h_{-\theta/2}(\mathbf{r}) & 0 & 0 \\ 0 & 0 & Th_{\theta/2}(\mathbf{r}) & T_{\mathbf{r}}^{\dagger} \\ 0 & 0 & T_{\mathbf{r}} & Th_{-\theta/2}(\mathbf{r}) \end{bmatrix}. \tag{2.28}$$

We can approximate the spectrum using a finite lattice of points in the moiré reciprocal space, with onsite Hamiltonians given by Eq. 2.23 and tunneling matrices given by Eq. 2.24. We subsequently diagonalize the Hamiltonian of the finite lattice and obtain the energies as a function of wave vector $\mathbf{k}$. We find that a circularly-shaped lattice of just 60 sites reproduces accurately the spectrum of magic-angle twisted bilayer graphene reported in Ref. [57]. We show the band structure through high-symmetry points at angles $\theta_m = 1.05°$ and $\theta = 2.0°$ in Fig. 2.8. This simple model replicates the most important characteristic of small-angle twisted bilayer graphene: the flattening of the moiré bands near a magic angle. Remarkably, just one degree of twisting changes the bandwidth of the moiré bands by a factor of almost a hundred (from $\approx 300\,\text{meV}$ at $\theta = 2.0°$ to $\approx 8\,\text{meV}$ at $\theta = 1.05°$). We further show the two non-equivalent, *i.e* not connected through time-reversal symmetry, quasi-flat bands in Fig. 2.9.

Notice that the four quasi-flat bands have two Dirac points, at the high-symmetry points K and K' (in this discussion we are referring to the high-symmetry points in moiré momentum space, not the high-symmetry points of graphene). In addition, they are mirror-symmetric about the zero-energy line $E = 0$, *i.e.* $H(\mathbf{k}) = -H(\mathbf{k})$. Recall that the Dirac points of graphene are protected by a combination of time-reversal and inversion symmetry. Time-reversal symmetry is of course preserved in the continuum model of twisted bilayer graphene, given by Eq. 2.28, since we included the contributions from both Dirac points (which are connected through a time-reversal operation). However, inversion symmetry is broken in twisted bilayer graphene because of corrugation. In graphene, sublattice symmetry $A \leftrightarrow B$ implies inversion symmetry. The corrugation of the lattice implies that the tunneling amplitudes between sublattices AA and AB/BA are not equal, and therefore sublattice symmetry is broken. However, as we mentioned earlier there is a hidden symmetry present in twisted bilayer graphene which effectively acts as a type of inversion symmetry, and protects the Dirac points in the continuum model. This is the layer-swapping symmetry. Swapping the layers leaves the system unchanged, but swaps the labels of points AB and BA. This operation corresponds to a conjugate-transpose of the tunneling tensors $T_n \rightarrow T_n^{\dagger}$. This symmetry, in conjunction with time-reversal symmetry, protects the Dirac points and implies the symmetry $H(\mathbf{k}) = -H(\mathbf{k})$. Breaking any of these two symmetries removes the protection of the Dirac points. An electric field between the layers, for example, breaks layer-swapping symmetry and induces a gap between the moiré bands.

The flattening of the moiré bands leads to a significant enhancement of the electron density of states. In Fig. 2.10 we show the density of states at the magic angle θ_m. Notice that even within

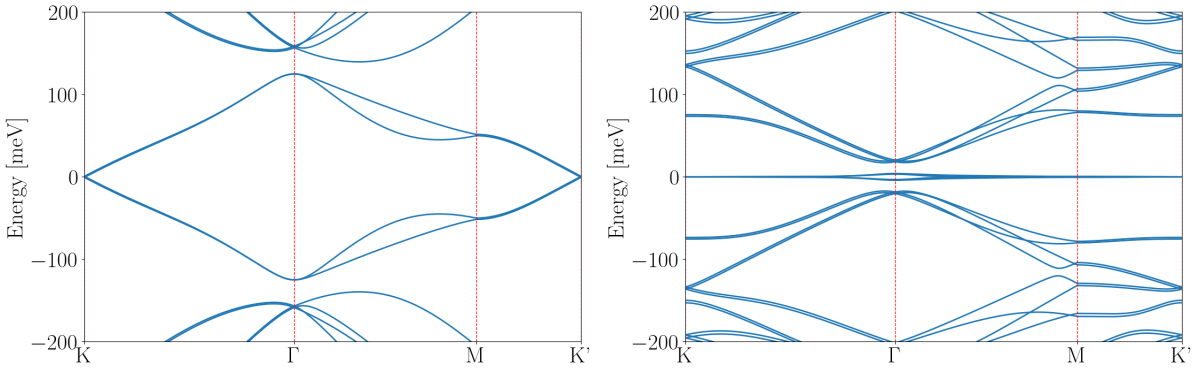

Figure 2.8: Flattening of the moiré bands using the continuum model: (a) $\theta = 2.0°$ and (b) $\theta = 1.05°$

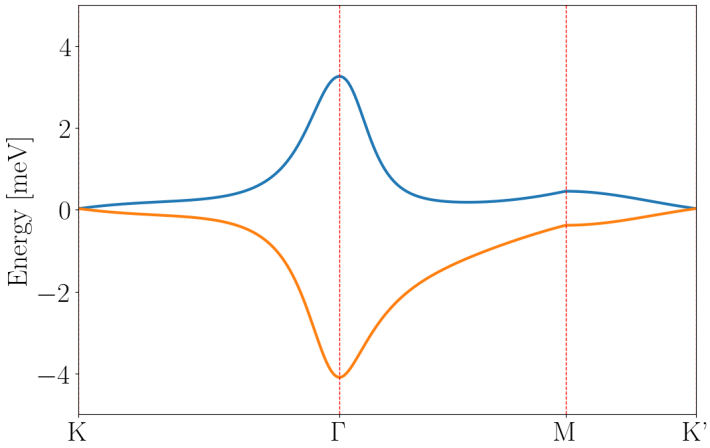

Figure 2.9: The two non-equivalent moiré bands in the continuum model at the magic angle $\theta = 1.05°$ (the other two are obtained by performing a time-reversal operation, which corresponds to particle-hole reflection)

the bandwidth of the quasi-flat bands, the difference in the density of states is enormous between the flatter regions (those with $|E| < 0.5\,\text{meV}$) and the more dispersive regions ($|E| > 1\,\text{meV}$). In addition, we clearly see the presence of the four pronounced peaks in the density of states. These critical points represent *van Hove singularities*. We will now turn to the discussion of these important singularities and their role in the correlated phenomena of twisted bilayer graphene.

2.3.2 Van hove singularities

The exotic phenomena observed in magic-angle twisted bilayer graphene are largely explained by the flattening of the four moiré bands. However, another crucial factor is the presence of singular points in the moiré flat bands near the Fermi level, that sharply enhance the density of states.

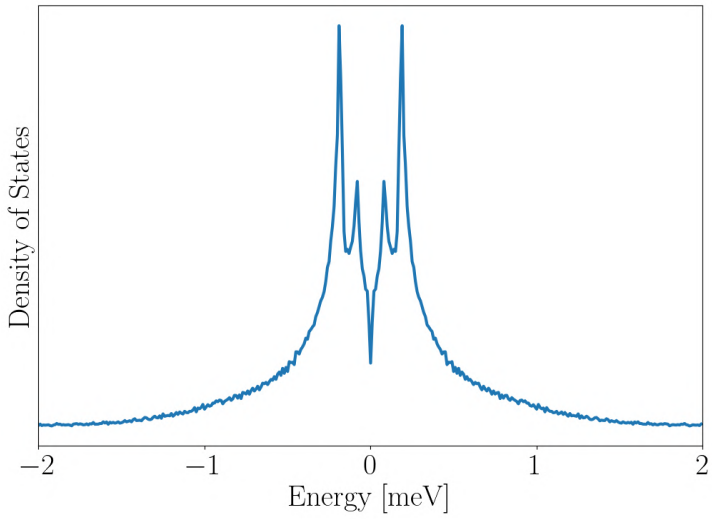

Figure 2.10: Density of States of twisted bilayer graphene at the magic angle $\theta = 1.05°$ throughout the bandwidth of the quasi-flat bands (see Fig. 2.9).

The importance of these singularities in the correlated phenomena observed in twisted bilayer graphene has been the subject of recent theoretical works [35, 36, 38]. Furthermore, the presence of such singular points near the Fermi level has been confirmed experimentally using scanning tunneling spectroscopy [60–62].

A van Hove singularity is essentially a saddle point with a diverging density of states. The first analysis of these critical points was conducted by the Belgian physicist Leon Van Hove in 1953 in a theoretical study of the phonon density of states in crystals [44]. We are instead interested in van Hove singularities present in the electronic quasi-flat bands of small-angle twisted bilayer graphene.

In two-dimensional materials with a dispersion relation $E(\mathbf{k})$, a van Hove singularity occurs in saddle points $\mathbf{k}_s$ defined by relations

$$\nabla_{\mathbf{k}} E(\mathbf{k}_s) = 0, \qquad \det D \leq 0, \tag{2.29}$$

where $D_{ij} = \frac{1}{2}\partial_i \partial_j E$ is the 2×2 Hessian matrix of $E(\mathbf{k})$, valued at $\mathbf{k}_s$. So-called ordinary van Hove singularities occur when the strict inequality holds, while high-order van Hove singularities are present when the equality is fulfilled. Recall that a positive D implies either a local minimum or maximum, and therefore it can not be a saddle point. Van Hove singularities are important due to the divergence of the density of states at these critical points. The density of states can be calculated analytically using the following relation:

$$\rho(E) = -\frac{1}{\pi} \int \frac{d^2\mathbf{p}}{4\pi^2} \frac{1}{E + i0^2 - E(\mathbf{p})}. \tag{2.30}$$

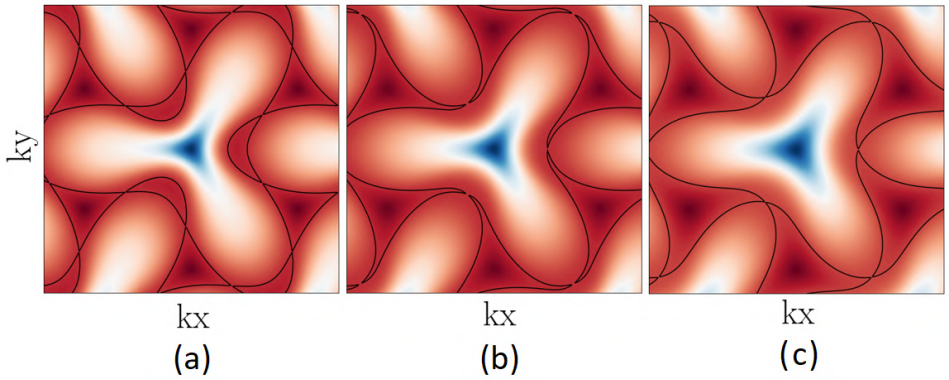

Figure 2.11: Examples of van Hove singularities near the Fermi energy in the hole band of the continuum model of near-magic angle twisted bilayer graphene. The black contour line represents the points with equal energy E_c that aligns with a diverging point in the density of states. The color scale is blue-white-red divergent, from a minimum at the $\Gamma-$point and a maximum at the Dirac points. The parameters are:(a) $E_c = -0.539$meV, $\theta = 1.040°$; (b) $E_c = -1.525$meV, $\theta = 1.075°$; and (c) $E_c = -5.024$meV, $\theta = 1.150°$

Such analysis was conducted in the work of Noah F.Q. Yuan *et al.* [27], where they conclude that ordinary van Hove singularities lead to a logarithmically divergent density of states, and high-order ones show a power-law divergence. Clearly, high-order van Hove singularities have a stronger effect in the density of states, due to the power-law overcoming rapidly the logarithmic dependence. The importance of higher order singularities in magic-angle twisted bilayer graphene has been the subject of intense analysis, due to the fact that both theoretical [27] and experimental studies [61] indicate the presence of these high-order singularities near the Fermi level in the vicinity of the first magic-angle $\theta_m \approx 1.05°$.

Since van Hove singularities are simply saddle points in the energy dispersion, we can visually locate them plotting the Fermi surfaces of the moiré bands in the moiré Brillouin zone. A contour plot, *i.e.* a Fermi surface plot, given by the condition $E_c = const$ near a diverging point of the density of states will reveal the saddle points: for ordinary van Hove singularities we observe the intersection of Fermi contours, the crossing of different Fermi lines; for higher order van Hove singularities we notice either a tangential touching of Fermi contours, or a multi-critical point in which more than three Fermi contours cross at a single point in reciprocal space. Fig. 2.11 shows three examples of van Hove singularities near the magic angle θ_m in the continuum model of twisted bilayer graphene, present in the hole moiré band shown in Fig. 2.9. Subpanels (a) and (c) show ordinary van Hove singularities, and subpanel (b) shows a high-order van Hove singularity, which corresponds to a tangential touching of two Fermi contours. Note that the twist angle at which we find a high-order singularity in this model is within a few hundredths of a degree from the first magic angle θ_m. Finally, to locate van Hove singularities we can directly calculate the density of states of a discrete 2×2 grid of the moiré reciprocal space, and locate the points of

divergence, which is what we did to produce Fig. 2.10.

Experimental studies report that the moiré bandwidth of near-magic-angle twisted bilayer graphene is in the tens of meVs, which is about an order of magnitude higher than this continuum model predicts. And this approach has other significant limitations. It is a long-wavelength theory defined in momentum space, and therefore many observables are difficult or unfeasible to calculate. The effects of complex phenomena, such as electron-electron interactions, correlations at the moiré scale and others, are also difficult to incorporate into this model. In addition, twisted bilayer graphene is particularly sensitive to disorder of several types, and these effects are inherently difficult to model in momentum space since they originate from distortions of the real-space crystal structure (though in some cases we find exceptions, such as the effect of lattice corrugation, which was added to the model via the tunneling amplitudes between the moiré sublattices). Nevertheless, it is remarkable that this simple model is capable of reproducing the flattening of the moiré bands with such precision. In addition, the continuum model also features the presence of van Hove singularities near the Fermi level, which represent a crucial component of the band structure of near-magic-angle twisted bilayer graphene.

2.3.3 Tight-binding model

Various modeling approaches have been utilized for the study of twisted bilayer graphene. These approaches include continuum models, such as the one described above; *ab initio* methods; density functional calculations; and effective tight-binding models. In this work, we primarily use quantum transport simulations of large mesoscopic samples to study the low-energy electronic properties of this material. We require large samples to ensure that finite-size effects at small twist angles are not the dominant factors. This renders *ab initio* methods unfeasible, due to their high numerical demands. First-principles calculations cannot be performed for samples of sizes relevant to correlations at the moiré scale for small twist angles. A single unit cell at the first magic angle $\theta_m = 1.05^\circ$ contains tens of thousands of sites. As mentioned previously, density functional theory methods are capable of calculating the spectrum of twisted bilayer graphene, even at small twist angles, but they cannot compute the conductivity of finite samples with tens of moiré unit cells. On the other hand, continuum models are long-wavelength theories that are incapable of fully capturing details at lengths and energy scales relevant to transport in mesoscopic systems. Thus, tight-binding models constitute the only method through which we can accurately capture the low-energy electronic properties of twisted bilayer graphene over a wide range of twist angles, while having the advantage of being computationally cheaper to scale up. For this reason, the tight-binding model is the main approach we use in subsequent chapters.

A few tight-binding models of twisted bilayer graphene have been proposed over the last two decades. The fact that only p_z orbitals are involved in the coupling of the layers makes this a simple system. The main difficulty lies not in the complexity but in the scale of the simulated devices. Even the single-particle non-interacting tight-binding models encounter numerical lim-

itations when the Hamiltonian of the system has hundreds of thousands of sites. Fortunately, tight-binding Hamiltonians constitute sparse matrices, and therefore we can efficiently calculate the low-energy properties of even enormous systems. This is because sparse matrix diagonalization of a few eigenvalues and eigenvectors is numerically very efficient. For our purposes we are interested uniquely on the properties of the moiré bands of twisted bilayer graphene, and a few low-energy dispersive bands that may be important for quantum transport at low-energies. The flattening of the bands also means that we can focus on a narrow range of energies near the Fermi level. The physical properties of twisted bilayer graphene at energy scales far outside the moiré spectrum are in many cases effectively identical to those of bilayer graphene, so we study instead the low-energy electronic properties where moiré physics dominates at low temperatures.

A particularly simple tight-binding model that we make use of was developed by Xianqing Lin and David Tománek in 2018 [63]. In this approach, the interlayer hopping integral $t'(r)$ is modeled using an exponentially decaying isotropic function $V^{xy}_{pp\sigma}$, which is the result of a fitting procedure used on a Slater-Koster approximation of the overlap integrals of the σ bonds between the p_z orbitals in different layers. This leads to a *minimum effective model* of the interlayer hopping amplitude

$$V^{xy}_{pp\sigma}(r_{xy}) = V^{0}_{pp\sigma} e^{-\left(\sqrt{r_{xy}^2+d_0^2}-d_0\right)/\lambda} \frac{d_0^2}{r_{xy}^2+d_0^2}, \tag{2.31}$$

where $V^0_{pp\sigma} = 0.39\,\text{eV}$ is the interlayer nearest-neighbor hoping amplitude of untwisted bilayer graphene, $d_0 = 3.35\,\text{Å}$ is the interlayer separation (constant if we neglect corrugation), r_{xy} is the xy-plane distance between sites, and $\lambda = 0.27\,\text{Å}$ is a parameter that modulates the decay of $V^{xy}_{pp\sigma}$. The values of $V^0_{pp\sigma}$ and d_0 are taken from precise measurements of $AB-$stacked bilayer graphene [35]. The decay parameter is obtained by fitting the spectrum of $AB-$ and $AA-$stacked bilayer graphene calculated using Eq. 2.31, to the spectrum that is obtained using the four γ model discussed in Sec. 2.2. This minimum model with isotropic exponential decay is capable of reproducing the spectrum of bilayer graphene, of both stable configurations, with high precision. In addition, it also reproduces the spectrum of uncorrugated twisted bilayer graphene very accurately. However, if we wish to model also the corrugation of the lattice, so that $d = d(r)$ is not constant, this simple function is incapable of accurately describing the changes that occur in the moiré bands. The reason for this is that the parameter λ is fitted to variations in the xy-plane distance r_{xy}. But corrugation induces changes in the out-of-plane $z-$direction, and therefore the decay of the hopping amplitude due to corrugation is different than the effect described by λ. We expect the decay to be different because the screening will be stronger in the $xy-$direction than in the $z-$direction, as we explained in Sec. 2.2.

A more complex environment-dependent tight-binding model was developed by M. S. Tang *et al.* in 1996 and applied to several carbon-based systems with satisfactory results [64]. This model goes beyond the traditional two-center approximation, and allows the hopping parameters to

be dependent on the binding environment, which crucially includes a *screening function* S. The interlayer hopping in this approach is generically expressed as

$$t'(r_{ij}) = \alpha_1 R_{ij}^{-\alpha_2} e^{-\alpha R_{ij}^{\alpha_4}} \left(1 - S_{ij}\right), \tag{2.32}$$

where $r_{ij} = \sqrt{r_{xy}^2 + r_z^2}$ is the three-dimensional distance between sites i and j, R_{ij} is the scaled distance, and S_{ij} is the screening function. Parameters α_i are determined with a fitting procedure. The screening function S is modeled using the relation

$$S_{ij} = \frac{e^{\xi_{ij}} - e^{-\xi_{ij}}}{e^{\xi_{ij}} + e^{-\xi_{ij}}}, \tag{2.33}$$

where

$$\xi_{ij} = \beta_1 \sum_l e^{-\beta_2 \left(\frac{r_{il} + r_{jl}}{r_{ij}}\right)^{\beta_3}}, \tag{2.34}$$

and β_i are screening parameters, which are also determined by a fitting procedure. The sum in Eq. 2.34 is over l neighboring atoms of sites i and j. By construction, the screening function S_{ij} is near 0 if i and j are nearest-neighbors, and approaches 1 if there are neighboring atoms near a line connecting sites i and j.

The scaled distance is defined as follows:

$$R_{ij} = r_{ij} \left[1 + \frac{\delta}{2} \left(\left(\frac{g_i - g_0}{g_0} \right) + \left(\frac{g_j - g_0}{g_0} \right) \right) \right], \tag{2.35}$$

where g_i and g_j are the effective coordination numbers of atoms i and j, and g_0 denotes the coordination number for a reference atom in graphene. The effective coordination number is given by

$$g_i = \sum_j \left(1 - S_{ij}\right), \tag{2.36}$$

where S_{ij} takes the form of the screening function defined above, but with different screening parameters β_i. This environment-dependent model is highly accurate and significantly improves the applicability of the tight-binding approach to carbon systems. However, we note that the fitting procedure does not produce parameters that accurately model all carbon-based systems. There are various parametrizations that have been calculated, and their accuracy varies depending on the type of carbon crystal for which they were intended. Nonetheless, in the specific case of twisted bilayer graphene, this approach allows us to incorporate the effects of interlayer distance variation in our simulations, arising either from corrugation of the lattice or applied uniaxial pressure. However, it is computationally intensive since it requires many calculations for each pair of atoms to estimate the effective interlayer hopping amplitude. To address this issue, we use a similar approach to the work of X. Lin *et al.* in Ref. [63] that led to the minimum effective model described by Eq. 2.31.

Before we describe our method to derive the effective decay in the $z-$direction, we note that the parametrization of Ref. [64] is not well-suited for graphene systems. This parametrization badly reproduces the band structure of bilayer graphene and twisted bilayer graphene. Fortunately, other works have expanded on this flexible model and found more accurate parametrizations. We use the parameters calculated by Landgraf *et al.* in 2013 [65], which were obtained using a different fitting procedure. This parametrization reproduces very accurately the band structure of graphene-based systems, including bilayer graphene, twisted bilayer graphene and even multilayer graphene (of more than two graphene layers).

Firstly, we need to establish if both the minimum effective model of X. Lin *et al.* and the environment-dependent model of M. S. Tang *et al.* are consistent with each other, since they depend on quite different fitting procedures. The effective decaying parameter λ in Eq. 2.31 is defined in relation to the in-plane distance r_{xy}. Thus, we can consider a fixed i site in one of the layers and compute t'_{ij} in Eq. 2.32 for multiple neighboring atoms j on the other layer. Then, we fit the calculated values to an exponentially decaying function. This procedure yielded a decay parameter $\lambda_2 = 0.26\,\text{Å}$, near the value $\lambda = 0.27\,\text{Å}$ calculated by X. Lin *et al*. We therefore find that both methods consistently yield similar values of the decay parameter in the xy-plane direction, and we can proceed to use the environment-dependent model to derive the decay in the z direction.

We again fitted the calculated interlayer hopping amplitude t'_{ij}, of several pairs of sites i (fixed) and j (neighboring) to an exponentially decaying function, when varying the interlayer distance between the graphene sheets d. We then obtained a new effective decay in the out-of-plane direction $\lambda' = 0.50\,\text{Å}$. Since the effective interlayer overlap integral is not uniform throughout the moiré lattice, we found that the choice of site i slightly modifies the calculated value of λ'. However, this effect is marginal, we find that the maximum variation of λ' is just $\approx 0.1\%$.

Finally, to construct our model we combine the two effective decaying parameters λ and λ' into one function:

$$V_{pp\sigma}(\mathbf{r}) = V^0_{pp\sigma} e^{-\left(\sqrt{x^2+y^2+d_0^2}-d_0\right)/\lambda} e^{-|z-d_0|/\lambda'} \frac{d_0^2}{x^2+y^2+z^2}, \tag{2.37}$$

where $\mathbf{r} = [x, y, z]$ is a vector that connects two sites in different layers. In Fig. 2.12 we show the computed low-energy spectrum of twisted bilayer graphene through high-symmetry points for three small commensurate twist angles, and without corrugation. The moiré bandwidth at the magic angle θ_m is about the same as the one calculated using the continuum model. With corrugation, which we will consider later, the bandwidth is $\approx 10\,\text{meV}$, which is closer to experimental measurements [27]. Moreover, the moiré bands in this effective tight-binding model have an approximate symmetry $E(\mathbf{k}) = -E(\mathbf{k})$ for twist angles above $\theta \approx 1.1°$, but not below the first magic angle θ_m. At some twist angle near θ_m this approximate symmetry is broken. We can visualize this in Fig. 2.12, contrasting the approximately mirror-symmetric spectra of panels (c)

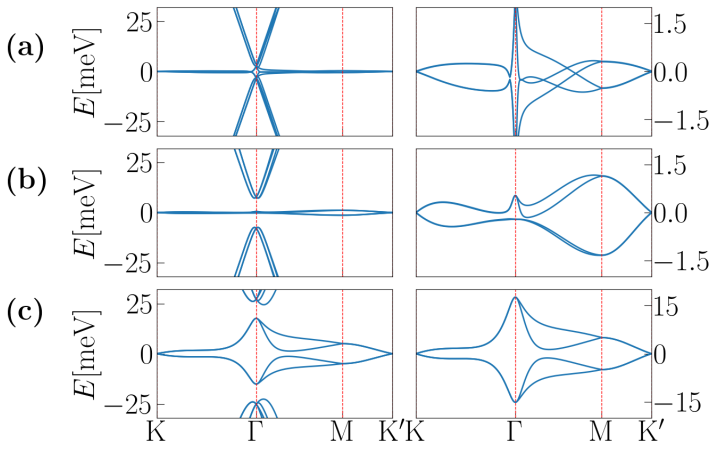

Figure 2.12: Near-magic angle twisted bilayer graphene, spectrum through high-symmetry points (see Fig. 2.2) in the tight-binding model: (a) $\theta \approx 1.02°$, (b) $\theta \approx 1.05°$ and (c) $\theta \approx 1.16°$

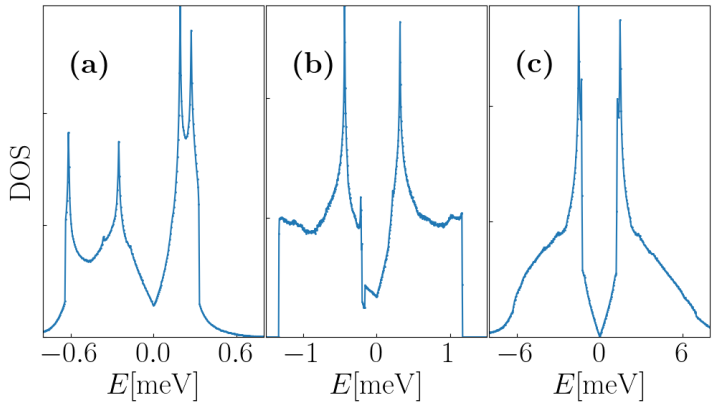

Figure 2.13: Density of States of near-magic angle twisted bilayer graphene in the tight-binding model: (a) $\theta \approx 1.02°$, (b) $\theta \approx 1.05°$ and (c) $\theta \approx 1.16°$

to those which are clearly not symmetric in panels (a) and (b). We recall that in the continuum model the electron and hole bands are always mirror-symmetric about the $E = 0$ line, unless layer-swapping symmetry is broken. The electron density of states at these three small twist angles is shown in Fig. 2.13. The density of states is still largely symmetric $E \leftrightarrow -E$ at the magic angle θ_m, but is clearly asymmetric at lower angles. This asymmetry of the density of states at small twist angles has important consequences, because it is principally the sharply enhanced electron density of states which leads to correlated phenomena in small-angle twisted bilayer graphene. Congruent with our results, experimental studies report that the moiré bands are asymmetric near the magic angle, but symmetric at larger angles. Tunneling conductance measurements show asymmetric conductance peaks at a twist angle $\theta = 1.10°$ [27]. On the contrary, at large angles $3° < \theta < 57°$ the density of states is symmetrical [24].

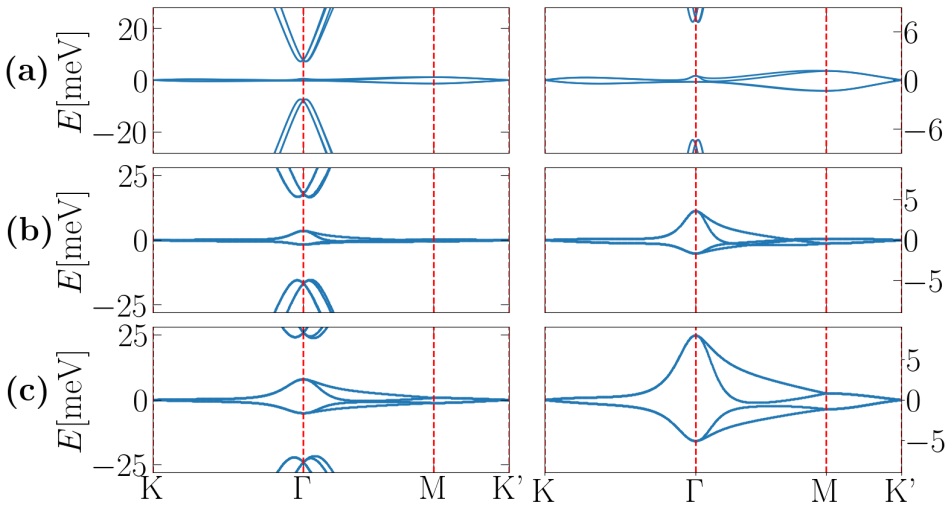

Figure 2.14: Effects of lattice corrugation on the low-energy spectrum through high-symmetry points of magic-angle ($\theta_m \approx 1.05°$) twisted bilayer graphene. We set $\Delta d := |d_{far} - d_{near}|/d_0$, where d_{far} and d_{near} represent the maximum and minimum interlayer distances between the layers respectively, and $d_0 = 3.35\,\text{Å}$ is the equilibrium interlayer distance of $AB-$stacked bilayer graphene. (a) $\Delta d = 0\%$; (b) $\Delta d = 1\%$; (c) $\Delta d = 2\%$.

2.3.3.1 Atomic corrugation

Equation 2.37 allows us to compute the effective exchange integral between two sites in different graphene layers. However, we still need to know what is the actual corrugation field, **i.e.** the position-dependent lattice distortion in the $z-$axis throughout the moiré lattice. Previous studies report that the corrugation field is dependent on the twist angle, and that at small angles it is moiré-periodic [56]. This is consistent with our previous considerations, since the lattice distortion mainly arises due to the differences in the effective interlayer coupling between the AA and AB/BA regions. Following Uchida K. *et al.* [56], we include the atomic corrugation in our effective tight-binding model using a moiré-periodic cosine function:

$$z(\mathbf{r}) = \frac{\alpha}{3} \sum_{j=1,2,3} \cos\left(\mathbf{r}\cdot\mathbf{G}_j\right), \tag{2.38}$$

where α is the corrugation amplitude, $\mathbf{G}_{1,2}$ are the moiré reciprocal lattice translations and $\mathbf{G}_3 := \mathbf{G}_1 + \mathbf{G}_2$. Figure 2.14 shows the effect of corrugation on the low-energy bands of magic-angle twisted bilayer graphene. Atomic corrugation is shown to have a strong effect on the moiré bands. A corrugation of $\Delta d = 2\%$, which corresponds to a corrugation amplitude of just $\Delta z_{max} \approx 0.1\,\text{Å}$, widens the quasi-flat bands by about one order of magnitude. Now, the corrugation amplitude in a suspended crystal of twisted bilayer graphene has been estimated to be as much as $\Delta d \approx 7\%$ [56]. This surprising result seemingly contradicts our previous analysis, since the moiré bands at the magic-angle are not quite flat if corrugation is included in our model. Indeed, for a corrugation of $\Delta d \approx 10\%$ the moiré bands are almost in the eV range, comparable to the band structure of

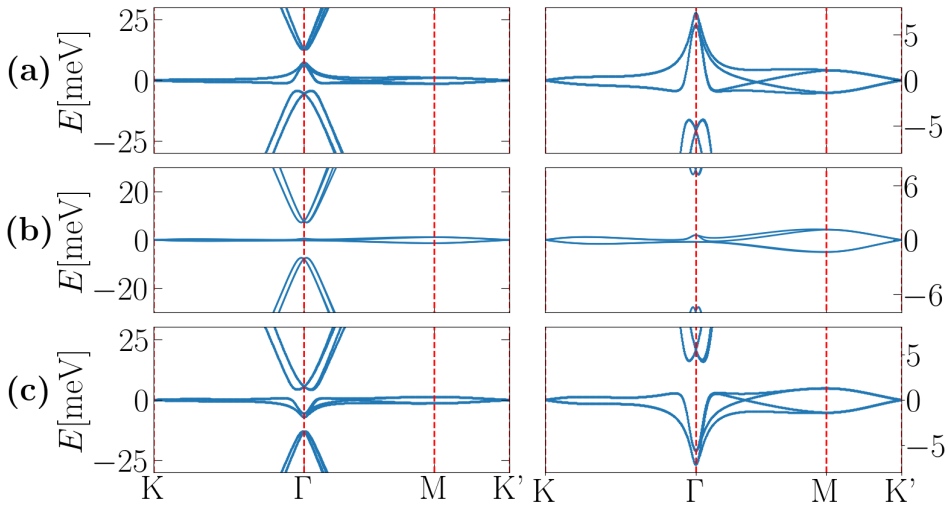

Figure 2.15: Effects of a Hartree potential on the low-energy spectrum through high-symmetry points of magic-angle ($\theta_m \approx 1.05°$) twisted bilayer graphene. Here $\Delta\nu = (\nu - \nu_\theta)$ is the doping level relative to the value at which the Hartree potential vanishes. (a) $\Delta\nu = -1$; (b) $\Delta\nu = 0$; (c) $\Delta\nu = 1$.

untwisted bilayer graphene! However, the estimated corrugation amplitude reported in the work of Uchida *et al.* greatly overestimates the value of the lattice distortion in realistic samples. A real device made of twisted bilayer graphene is never suspended in a vacuum. Instead, it is stabilized between two substrates, typically made of hBN layers, and often put under uniaxial pressure. The presence of the substrates in real samples is expected to greatly diminish the corrugation amplitude. Detailed scanning tunneling spectroscopy studies [61, 62, 66] and compressibility measurements [67] show that the moiré bandwidth at the magic angle is in the tens of meVs. We therefore estimate the corrugation to be in the order of $\Delta d \approx 1\%$ in realistic devices [24].

2.3.3.2 Hartree interactions

The tight-binding method is a one-particle, non-interactive approach that is almost always insufficient to describe the electronic properties of systems with strong electron-electron interactions. Thus far, we have discussed how the flattening of the moiré bands and the appearance of van Hove singularities near the Fermi level leads to the emergence of correlated phenomena at low energies, due to the sharp increase in the electron density of states. But we have stopped short of discussing electron-electron interactions directly, due to the limitations of our method. Our analysis can be described as tangential, trying to understand the dominant effects that lead to an increase in electron correlations without directly addressing these interactions. However, there are some electron-electron interactions that can be studied with tight-binding methods. Effective position-dependent potentials that emerge from interactions can be easily included to the onsite Hamiltonians throughout our lattice. One prominent example of such a potential is the *Hartree potential*, *i.e.* the electrostatic potential felt by an electron due to the average charge

distribution of all other nearby electrons. Electron-electron interactions in small-angle twisted bilayer graphene create an inhomogeneous Hartree potential, which has been predicted to give rise to a significant distortion of the moiré bands [68–72]. Goodwin *et al.* [71] showed that the Hartree potential can be included in our atomistic model with a moiré-periodic potential of the form

$$V_H(\mathbf{r}) = V_\theta(\nu - \nu_\theta) \sum_{j=1,2,3} \cos\left(\mathbf{r}\cdot\mathbf{G_j}\right), \tag{2.39}$$

where V_θ is a twist-angle dependent energy parameter (at the first magic angle we find that $V_{\theta_m} = 5.51\,\text{meV}$), $\nu_\theta = -0.24$ is the doping level where the Hartree potential vanishes, and $\mathbf{G}_j,\ \ j = 1,2,3$ are the moiré translations defined previously in Sec. 2.3.3.1. The magnitude of the Hartree potential in realistic crystals is hard to estimate, since it is influenced by factors such as the screening and electrostatic environment, which depend on the particular substrate. We note that these effects were not taken into account in the work of Goodwin *et al.*, and therefore the magnitude of the Hartree potential they report is likely much higher than that in real devices. We instead parametrize this potential via an effective potential strength $\Delta\nu V_\theta$, where $\Delta\nu = (\nu - \nu_\theta)$, and we assume that this parameter is of similar order as the Hartree-Fock potentials appearing in the correlated phases of twisted bilayer graphene due to Coulomb interactions [24]. Figure 2.15 shows the effect of the Hartree potential on the low-energy spectrum of magic-angle twisted bilayer graphene. The moiré bands are slightly widened, but not by a large factor. Noteworthy is the reduction of the bandgap of the moiré bands to the nearest dispersive bands. For a doping of $\Delta\nu = \pm 1$, the gap is almost closed. Also interesting is that near the Fermi level the moiré bands undergo band inversion. At zero doping, $\Delta\nu = 0$, the two electron moiré bands connect with the two hole bands only at the Dirac points K, K'. However, at $\Delta\nu = \pm 1$ they cross each other at a point located between the Γ and M high-symmetry points of the moiré reciprocal lattice.

2.4 Summary

In this chapter we developed the low-energy theory of twisted bilayer graphene, and we presented the model that we later use for studying this extraordinary material. We started with a long-wavelength Dirac continuum theory that allows us to qualitatively describe the flattening of the moié bands as we lower the twist angle to $\theta \approx 1°$, and a remarkably flat dispersion when we are near the "magic" angle $\theta_m \approx 1.05°$. In addition, we find that the flattening of the bands is accompanied by the appearance of critical points near the Fermi level, *i.e.* van Hove singularities, where the electron density of states diverges. These phenomena are crucial to understand the emergence of correlated phenomena in small-angle twisted bilayer graphene. However, we found that the continuum model has significant shortcomings: it predicts a narrower moiré bandwidth than the one reported in experimental measurements; it can not account for correlated phenomena on the scales relevant to mesoscopic quantum transport; it is difficult to expand, and therefore

incapable of studying additional complex phenomena present in small-angle twisted bilayer graphene, such as: Hartree interactions; Coulomb interactions; site impurities; lattice disorder; finite-size effects; non-zero temperature; and more. Due to these limitations, we developed an atomistic, effective tight-binding model, that allows us to scale finite samples to mesoscopic dimensions, where quantum transport measurements are possible. Furthermore, we have seen that this atomistic model is a remarkably flexible method that allows us to encompass many effects in our analysis, as long as these effects can be expressed as either onsite Hamiltonians, lattice distortions or contributions to the hopping integrals. We shortly discussed the effects of Hartree interactions and atomic corrugation on the low-energy spectrum of magic-angle twisted bilayer graphene. However, our model is capable of studying many other effects. A few notable examples are: intralayer or interlayer potential biases applied at a point-contact or a segment of the sample; the effects of site impurities and electrostatic disorder; the effects of an applied magnetic field (using the Peierls method to add a phase factor to the hoppings). Finally, we noted that this simple effective model shows remarkable congruence with experimental measurements of real samples. The estimated moiré bandwidth is within the same order of magnitude as measurements of real samples; this model predicts electron-hole asymmetry of the moiré bands near the magic angle; it also predicts important transitions in the moiré bands, that correspond to the energetic shifting of position of van Hove singularities near the magic angle.

CHAPTER 3

COHERENT QUANTUM TRANSPORT

The field of quantum transport studies the properties of electrons (more generally of charge carriers) as they pass through a sample which is small enough to exhibit quantum phenomena. The actual size that a particular device must have in order to be considered quantum greatly varies, depending on many factors. A few important factors are: the intrinsic physical properties of the constituent materials; the external constraints that are imposed on the device (such as temperature or magnetic field); the dimension and geometry of the device; the degree of disorder (of various types) present in the sample [73]. If a device exhibits quantum properties, a typical transport measurement will show the quantization of one or more physical observables, such as charge q, conductance G (equivalent to resistance ρ), or magnetic flux Φ.

Quantum transport measurements constitute a very powerful tool to probe a system in order to gain access into its physical properties. They are relatively inexpensive, highly tunable, and can be remarkably precise (for example, quantum Hall resistance measurements have been found to be accurate to better than one part in a billion [74]). We can also derive detailed information about the electronic band structure, and its associated density of states. Moreover, we can directly measure the charge mobility, and infer the types of scattering mechanisms present in a particular device under precisely-controlled conditions. In general, we can typically calculate the carrier density and mobility with a simple measurement of the low-field magnetic resistivities in semiconducting films. For this reason, a Hall measurement is a basic characterization tool for semiconducting films [73]. In particular, two-dimensional (2D) materials have favorable properties for quantum transport, especially in the case of semiconducting films, due to the large Fermi wavelengths and large mobilities that can be achieved [75]. Thin semiconducting samples at room temperature have been shown to exhibit the quantum Hall effect [73]. On the contrary, in the case of metallic thin films, for quantum phenomena to be present the sample typically

needs to be very small, of a few nanometers at most, and the temperature very low.

Quantum transport measurements have played a prominent role in researching the physical properties of magic-angle twisted bilayer graphene. In fact, most of the extraordinary phenomena observed in this material is deeply linked with quantum transport. To name just a few: superconductivity; unconventional Mott-insulating phases; an oscillating thermoelectric power, *i.e.* a voltage differential due to a thermal gradient. Indeed, the initial discovery of its unusual correlated phases is the result of precise quantum transport measurements at very low temperatures [15]. Despite several years of intense research, interesting transport properties have been discovered in recent years. For example, "strange metal behavior" has been observed in doped magic-angle twisted bilayer graphene [76]. Strange metal behavior is a consequence of Planckian scattering rates and linear magnetoresistivity, whereas the superconducting phases in magic-angle twisted bilayer graphene are associated with Fermi-liquid behavior. Very recent observations of an oscillating Seebeck coefficient (a measure of thermoelectric power) are consistent with the topological heavy Fermion model of magic-angle twisted bilayer graphene, shortly mentioned in the introduction of Chapter 2. Quantum transport studies are also not limited to experimental measurements. Our contribution to the scientific literature consisted of numerical simulations based on the theory outlined in this chapter [20, 24]. We note that any more quantum transport studies of this material have been published in recent years [10, 32, 42, 77–81].

The theory of quantum transport has been at the forefront of many important technological developments. Currently, the most economically impactful is the effort to expand the range of capabilities of conventional electronics. Since the 1960's, the number of transistors in an integrated circuit has roughly doubled every two years, an observation first noted by Gordon Moore in 1965 and now referred to as Moore's law. The main reason this technological trend has continued for several decades is that transistors could be made smaller and smaller, as the technical capabilities of technology companies increased. However, a modern state-of-the-art transistor is already so small that it has only a few hundreds or even tens of available quantum states. An electronic system of this size necessarily requires quantum analysis to describe its properties [82]. Reducing the size of such transistors makes them susceptible to quantum fluctuations, which implies unreliability and therefore they would be no longer useful as bits of information. Surprisingly, some researchers are trying to exploit the quantum nature of such devices to improve efficiency, seeing it as an advantage instead of a hindrance [83]. However, the fact of the matter is that increasing the number of transistors in an integrated circuit is no longer a matter of technical difficulty, but of physical limitations. The breakdown of Moore's Law in modern integrated circuits is often referred to as the *scaling problem*, and constitutes the main obstacle to the development of new electronic technologies.

Quantum transport researchers have proposed several possible solutions to the scaling problem, which can be generally understood as extending the functionality of conducting electrons in devices. This can be done by optimizing the properties of charge carriers or by increasing the

available degrees of freedom. For example, there is great interest in making quantum transport resistanceless. Heat dissipation is a major cost and physical constraint in integrated circuits and remains one of the most important factors to consider in microcircuit design. And heat dissipation is only one of many problems in current electronic systems. Here are just a few noteworthy examples of quantum transport subdisciplines that aim to improve conventional electronics: Topological quantum transport is a discipline that seeks to produce devices with near-zero electrical resistance that are robust against disorder due to the topological protection of edge states. Superconductivity research is finding many applications in recent years, such as quantum computing through the use of Josephson junctions, and the search for room temperature superconductors with industrial applications is still considered by some to be the holy grail of condensed matter physics. Spintronics aims to exploit the spin degree of freedom in addition to the charge of electrons, greatly expanding the range of applications of conventional electronic devices, for instance by making information transfer essentially resistanceless through the propagation of spin waves. Valleytronics proposes to exploit local extrema (valleys) in the band structure to either optimize the properties of conventional charge carriers or to add new properties to them.

Of particular relevance to this work and closely related to the theory of quantum transport is the field of *twistronics*. Twistronics essentially consists of tuning the physical properties of charge carriers by exploiting the moiré structure that forms when 2D materials are stacked with a relative twist between them. In such devices, moiré physics can be used as a powerful tool to enhance desirable conducting properties, or even to add entirely new functionalities. For instance, as we discussed in Chapter 2 the electron density of states can be made exceptionally large near the Fermi level in small-angle twisted bilayer graphene. Despite the promising properties measured in controlled experiments, twistronics has been hindered by a few technical difficulties. A common problem with moiré lattices is crystal disorder, which often strongly suppresses the emergent moiré phenomena. In addition, the preparation of moiré lattices is often technically difficult. The field of single-layer 2D materials is in fact quite young, graphene was experimentally realized just two decades ago in 2004 [1]. Moiré systems add a great deal of complexity by requiring the precise overlapping of high-quality and extremely sensitive 2D layers, and then stabilizing the sample with an adequate substrate that does not significantly modify the crystal structure. These are just a few of the reasons why this area of condensed matter physics has been explored only recently, after technological developments allowed researchers to fabricate 2D devices of extremely high quality under controlled environments. In the case of twisted bilayer graphene, state-of-the-art techniques allow for the twist angle to be pinned down to within a tenth of a degree. And twisted bilayer graphene is only one of many materials that have been shown to exhibit exotic phenomena when stacked with a twist. Moiré physics is a promising field with many unexplored avenues, and graphene systems should be considered only the starting point of the field. It is to be hoped that the remarkable conducting properties obtained in precise laboratory measurements will one day be exploited in functional devices.

In this chapter we develop the essential theory of coherent quantum transport that is necessary for the analysis of mesoscopic quantum transport simulations (without a magnetic field). We note that this is not a comprehensive survey of the field, which is too large for the purposes of this work. The reader is encouraged to see the work cited in Refs. [73–75] for a deeper dive into the theory. Instead, we focus on the main tool we use to probe the electronic properties of mesoscopic twisted bilayer graphene: ballistic (coherent) quantum transport within the Landauer-Büttiker formalism. Furthermore, we do not treat magnetotransport since we do not use magnetic fields in any of our simulations. Magnetoresistance measurements are a major pillar of the field of quantum transport, so this promising line of research is left for future studies. Nevertheless, we believe that the selected experiments described in this chapter sufficiently illustrate the main concepts which are relevant to the results outlined in the following chapters. We start in Sec. 3.1 with an introduction to the length scales involved in quantum transport measurements, *i.e.* the mesoscopic scale. Here we discuss generically the types of scattering and how they influence quantum phenomena. In Sec. 3.2 we briefly introduce the Drude model, and explain why it is incapable of describing quantum phenomena in mesoscopic samples. We then derive the Landauer formula in Sec. 3.4 for a simple two-terminal device at zero temperature. Next we extend our results to multi-terminal devices at low temperatures. Finally, we relate the transmission function to the scattering matrix formalism to obtain a comprehensive picture of the theory.

3.1 The mesoscopic scale

A small sample whose dimensions are intermediate between the microscopic and the macroscopic is called *mesoscopic*. The mesoscopic scale is much larger than the atomic scale, but not large enough to be considered a classical system. To be precise, in a classical conductor the conductance G shows an "*ohmic*" behavior, which means that the conductance is proportional to the area cross-section A through which electrons travel and inversely proportional to the length L between two contacts:

$$G = \sigma \frac{A}{L}, \tag{3.1}$$

where the conductivity σ is an intrinsic property of the material. Typically, a conductor exhibits ohmic behavior if its dimensions are much larger than a few characteristic length-scales, the most important of which are the following: the de Broglie wavelength λ of conducting electrons; the mean free path L_m, *i.e.* the average distance that an electron travels before its initial momentum is effectively destroyed; and the phase relaxation length L_φ, the average distance that an electron travels before its phase is effectively randomized. These length scales define the distances over which properties of the conducting electrons' wavefunctions are randomized by scattering processes, and can vary enormously from one material to another. Because of this, quantum transport phenomena have been observed in conductors with widely varying dimensions,

from just a few nanometers to hundreds of microns. In addition, these length scales are strongly affected by external parameters, principally by temperature, because of their effects on various scattering mechanisms.

To understand why ohmic behavior breaks down in mesoscopic systems, let us consider each of the three characteristic length scales mentioned above. First of all, if the de Broglie wavelength of conducting electrons is comparable to the size of the system, then clearly we cannot describe electrons as point-particles, and a wave description is necessary. Ohmic behavior is observed in systems described by semi-classical approaches such as the Drude model, which assume that electrons are point-particles and therefore neglects the effects of quantum interference. Therefore, in systems with sizes comparable to the wavelength of conducting electrons wave dynamics is essential to describe phenomena such as quantum interference. In the case of metals, conducting electrons have a small wavelength, comparable with the size of an atom $\lambda \approx 1\text{Å}$. Because of this a metallic device typically shows quantum properties only if its temperature is very low and if its size is very small. For semiconductors, the wavelength of conducting electrons can reach the micron range, and nanoscale devices at room temperature are more feasible.

3.1.1 Elastic and inelastic scattering

An electron in a perfect crystal moves unimpeded, as in a vacuum, but with a different mass. In the extreme case of graphene, the effective mass near the Fermi level is zero, and electrons behave as relativistic Dirac particles. Any deviation from perfect crystallinity, such as impurities, lattice vibrations (phonons) or electron-electron interactions leads to "collisions" that scatter the electron from one state to another. The mean free path L_m is therefore a measure of how much a particle travels in space before its initial momentum is destroyed due to these collisions. However, this does not mean that L_m equals the average distance that an electron travels between collisions. One collision might not be sufficient to effectively destroy the initial momentum. In fact, not all collisions are equally destructive of momentum. Inelastic scattering is typically more destructive of momentum than elastic scattering. We can therefore divide L_m into two components: the inelastic L_m^{inel} and the elastic L_m^{el} mean free paths.

For elastic scattering, we can distinguish large-angle scattering and low-angle scattering based on the angle between the incident and outgoing particles. A consequence of Fermi's golden rule is that scattering at static potentials does not change the energy of the scattered electrons. Therefore static impurities in a crystal can only contribute to elastic scattering, and they are temperature-independent. In the case of large-angle scattering, the mean free path L_m^{el} is roughly equal to the average distance between collisions, because a single collision is sufficient to randomize most of the initial momentum direction. Low-angle scattering only slightly changes a particle's direction of momentum, so that a typical particle undergoes many such collisions before its initial momentum direction is effectively randomized.

Inelastic scattering changes both the magnitude and direction of momentum, making it

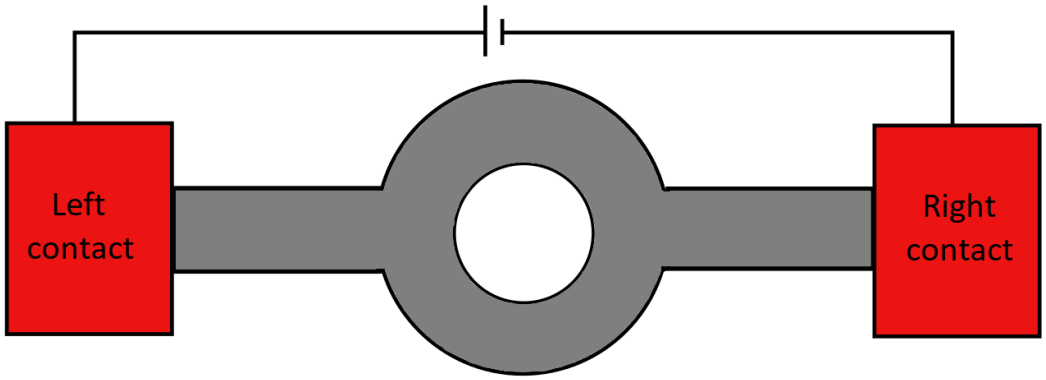

Figure 3.1: A ring-shaped mesoscopic scatterer in a two-terminal device. Incoming electrons from the left electron reservoir can travel through either one of the two arms of the ring. The type of scattering present in the conductor, as well as external constraints imposed on the device, will determine the type of interference pattern near the right contact.

generally more destructive. The most common types of inelastic scattering are phonon-electron and electron-electron interactions. However, electron-electron interactions preserve the total momentum and therefore do not affect L_m. Inelastic scattering is strongly temperature-dependent due primarily to phonon-electron scattering, and is therefore dominant over elastic scattering at high temperatures. Impurities with fluctuating internal degrees of freedom can also contribute to inelastic scattering, since they induce a dynamic potential.

In short, inelastic scattering depends heavily on temperature and is generally more destructive of a particle's momentum. We expect this to be the dominant mechanism at high temperatures. It largely arises due to electron-phonon interactions and impurities with dynamic internal degrees of freedom. Conversely, at low temperatures, the dominant source of scattering is generally elastic and arises from static impurities, crystal defects, and boundary effects.

Until now, we have considered the effects of scattering in regards only to the momentum of conducting electrons in a device. However, within the context of quantum transport, much more important is to consider the effect of collisions on an electron's *quantum phase*. We will now discuss this fundamental concept.

3.1.2 Coherent and incoherent transport

A device can be many orders of magnitude larger than the de Broglie wavelength of conducting electrons and still exhibit quantum phenomena, for the same reason that we can observe interference patterns on the surface of a large body of water. What matters most in quantum transport is the undistorted propagation of electron waves. If most electrons preserve the correlation of their phases as they pass through a device from one contact to another, we expect interference phenomena to be observed regardless of the size of the device. On the other hand, if the phases of

incoming electrons are completely randomized, then there are no correlations observed in the outgoing contact, and we expect a fluctuating interference pattern that time-averages to zero.

The phase-relaxation length L_φ can be defined as the average distance that an electron travels before its initial phase is randomized through scattering. Typically we observe interference effects if L_φ is comparable to the size of the device. Analogous to our discussion of the momentum-relaxation length, L_φ can be different than the average distance between collisions. However, in this case there are important subtleties that require further discussion.

We can understand the relevant concepts with a simple toy-model. Consider a ring-shaped scatterer, as illustrated in Fig 3.1. A vacant state in the scatterer is occupied by an electron originating from a source contact to the left, it propagates throughout the system in an average time τ until it exits at a drain contact to the right (throughout this work we will refer to electron reservoirs as terminals or contacts interchangeably). Electrons can travel through each of the two arms of the ring. In the absence of any form of scattering, we expect to measure an interference pattern due to the electron wavefunction interfering with itself at the point of convergence near the right contact. Moreover, we can tune the relative phase of electrons in different arms of the ring with a magnetic field perpendicular to the surface of the device. This creates oscillations of constructive and destructive interference as a function of magnetic field. These are known as the Aharonov-Bohm oscillations. Note that in this case $L_\varphi \to \infty$.

Now suppose we are not in a perfect crystal but in a real one with collisions due to impurities, phonons, electron-electron interactions, etc. We expect the interference amplitude to be reduced exponentially $\propto \exp[\tau/\tau_\varphi]$, where τ_φ is the phase-relaxation time. Furthermore, we expect interference to be strongly affected by temperature, due to inelastic scattering.

Let us first consider the effect of static scatterers present in the arms of the ring. Electrons will have a phase shift due to elastic collisions at static impurities, defects, etc., and in general near the right contact the phase-relationship between the electrons from different arms will be random. However, this phase difference will itself be static, i.e. constant in time. Therefore, a perpendicular magnetic field will again tune the interference in exactly the same way, and consequently we would observe Aharonov-Bohm oscillations of the same amplitude and period as in the case of a pure crystal. The length of the arms would only alter the point of reference of the phase difference at zero magnetic field. We thus conclude that the phase-relaxation length is not affected by static scatterers and $\tau_\varphi \to \infty$.

The situation is quite different for dynamic scatterers, such as phonon-electron, electron-electron interactions and impurities with fluctuating internal degrees of freedom. In this case, the phase relationship between the arms is randomized and there is no stationary interference pattern. If we time-average our measurements, we expect the effects of interference to average to zero. We therefore conclude that L_φ is determined by dynamic scatterers. We often find that the inelastic mean free path L_m^{inel} and L_φ are similar (in fact they are sometimes not distinguished in the literature) though L_φ tends to be slightly smaller than L_m^{inel}.

To summarize, we can distinguish three regimes of quantum transport based on the relation between the size of the device L, the mean free path L_m, and the phase-relaxation length L_φ. If a sample has dimensions smaller than L_m and L_φ, then most electrons will pass through without being scattered. We call such devices *ballistic*. On the other hand, if the device is significantly larger than L_m, then on average we expect a large number of scattering processes to take place in the time it takes for an electron to pass from one contact to the other. In this case the conduction is disordered, and we call such devices diffusive. Finally, we often distinguish an intermediate category called quasi-ballistic, in which $L_m \approx L$, where we observe a fluctuating interference with partial correlations between incoming and outgoing electrons.

In this work we utilize ballistic, mesoscopic samples of twisted bilayer graphene. This is because our focus is on the effects of the low-energy moiré bands of magic-angle twisted bilayer graphene on its energy-resolved conductance. Scattering mechanisms are not considered in our analysis. Even when considering the effects of temperature on the conductance (see Chapter 6), we only consider the thermal broadening of the occupation distributions of electrons, maintaining a single-particle non-interacting picture.

3.2 The Drude model

Let us recall the simplest of classical models of a conductor, called the Drude model in honor of Paul Drude who introduced it in 1900, and discuss its main properties. In a grounded metal (*i.e.* a conductor with no effective electric field inside of it), an electron is assumed to be a point particle bouncing chaotically, with a vanishing drift velocity and no collective diffusion. When an electric potential is induced between two contacts, electrons accelerate in the direction of the induced electric field $\mathbf{E}$. However, this acceleration is quickly countered by scattering processes until it averages to zero, so that we may write

$$\langle \frac{d\mathbf{p}}{dt} \rangle = \frac{m^* \langle \mathbf{v} \rangle}{\tau} = e\mathbf{E}, \tag{3.2}$$

where τ is the average momentum relaxation time, and m^* is the effective mass of electrons. The drift velocity $\mathbf{v}_d = \langle \mathbf{v} \rangle$ is therefore

$$\mathbf{v}_d = \frac{e\tau \mathbf{E}}{m^*} = -\mu \mathbf{E}, \tag{3.3}$$

Where $\mu := |e|\tau/m^*$ is the *mobility* of electrons in the conductor. We can relate the current density $\mathbf{j}$ to the electron density n_e via $\mathbf{j} = e\mathbf{v}_d n$ to obtain the Drude *conductivity*:

$$\sigma = \frac{j}{E} = n|e|\mu = \frac{e^2 n \tau}{m^*}. \tag{3.4}$$

To give these quantities some concrete expressions, let us consider a simple two-dimensional electron gas. The electron density in this case is constant and determined by the Fermi wave vector k_F: $n_{e,2d} = k_F^2/2\pi$. Then, the Drude conductivity of a 2D electron gas is

$$\sigma_{2d} = \frac{2e^2}{h}\frac{\pi L_m}{\lambda_F} \approx \frac{2e^2}{h}\frac{L_m}{d_{e,e}}, \tag{3.5}$$

where $L_m = v_F\tau$ is the momentum relaxation length. The coefficient $d_{e,e}$ can loosely be interpreted as the distance between electrons. When the ratio $L_m/d_{e,e} \approx 1$, i.e. when the momentum relaxation length is comparable to the distance between electrons, then we are deeply in the ballistic regime. On the other hand, the term $2e^2/h$ is a fundamental constant for quantum transport, which corresponds to a quantum of conductance.

Thus far we considered the conduction of electrons in terms of the *drift* velocity, acquired by electrons due to the induced electric field. However, we can approach the same problem through another route and describe conduction in terms of electron *diffusion*. In this analysis, excess states occupied in the contact with higher chemical potential E_F^+ will diffuse to the vacant states in the contact with lower chemical potential E_F^-. The diffusion current is given by relation

$$\mathbf{j} = -eD\nabla\rho, \tag{3.6}$$

where D is the diffusion coefficient and ρ is the electron density of states. Let us consider again a two-dimensional electron gas. The electron density of states of a 2D electron gas is constant $\rho_{2d} = m^*/\pi\hbar^2$, so we might expect there to be no diffusion gradient. This is of course true at energy ranges bellow E_F^-. However, at zero temperature, states within the energy range $E_F^+ - E_F^-$ are fully occupied only on one of the contacts, the one with higher chemical potential E_F^+, and fully vacant in the other one. This occupation differential induces a diffusion gradient:

$$\nabla\rho = \rho_{2d}\frac{E_F^+ - E_F^-}{L}\hat{x}, \tag{3.7}$$

where L is the length between the contacts and $\hat{x}$ a unit vector in the direction of diffusion. Plugging Eq. 3.7 in Eq. 3.6 yields

$$\mathbf{j} = e^2 D\rho_{2d}\frac{E_F^+ - E_F^-}{|e|L}\hat{x} = e^2 D\rho_{2d}\mathbf{E}. \tag{3.8}$$

Thus, the conductivity is given by the following relation:

$$\sigma = e^2\rho_{2d}D. \tag{3.9}$$

Equation 3.9 is the Einstein relation for *degenerate conductors*, *i.e.* in conductors where the difference between the Fermi level and the bottom of the bands is much larger than the thermal energy $E_F - E_b >> k_BT$. Notice that Eqs. 3.4 and 3.9 have very different interpretations of the same physical observable. For these equations to be consistent, the diffusion coefficient and the mobility should be related as follows

$$\frac{|e|D}{\mu} = \frac{n_s}{\rho_{2d}} = E_F^+ - E_F^-, \tag{3.10}$$

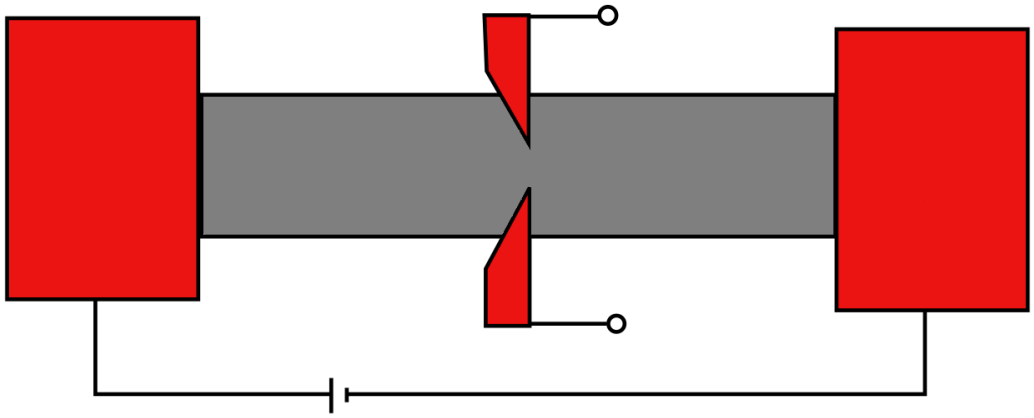

Figure 3.2: A split-gate two-terminal configuration. The effective width of the conductor can be made narrower by applying a negative voltage in the contacts attached in the middle of the conductor.

From Eq. 3.10 we can obtain the following expression that relates the diffusion coefficient with the Fermi velocity:

$$D = \frac{1}{2} v_F^2 \tau. \tag{3.11}$$

Suppose now that we double the electron concentration in a conductor, which would have a measurable doubling of the conductivity σ. Equation 3.4 suggests that this doubling is a consequence of the twofold increase of the electron density n . On the other hand, Eq. 3.9 (together with relation Eq. 3.10) indicates that it is instead the Fermi velocity what causes the doubling of the conductivity, the electron density of states is unaltered. This curious difference in interpretation only holds for degenerate conductors, where the diffusion coefficient is proportional to the conductivity (Eq. 3.9). For non-degenerate conductors, *i.e.* in the hi, the Einstein relation can be obtained by replacing $(E_F^+ - E_F^-)$ with $k_B T$ (this correspondence between degenerate and non-degenerate conductors generally holds [73]), which leads to equation

$$\frac{|e|D}{\mu} = k_B T. \tag{3.12}$$

Thus, the diffusion coefficient for non-degenerate conductors, , is proportional to the mobility and not to the conductivity.

3.3 The breakdown of the Drude model: Mesoscopic experiments

Imagine a simple two-terminal (in this work we use the words terminal and contact interchangeably) setup like the one depicted in Fig. 3.2. In this device a pair of metallic gates is added in the middle of the scatterer (often referred to as a split-gate probe). A negative voltage induced on

the gates depletes electrons in the scatterer, and effectively *constricts* the width of the conductor. According to Ohm's Law (Eq. 3.1), this constriction should linearly decrease the conductance G as a function of the induced negative voltage (or, correspondingly, increase the resistance G^{-1}). The first two mesoscopic split-gate experiments on semiconductors were reported on 1988 [84, 85]. The conductance shows a step ladder decay as a function of negative voltage, instead of a continuous decreasing line, with plateaus at multiples of the quantized unit of conductance $2e^2/h$ (and correspondingly of resistance $h/2e^2$). As we will see shortly, the breakdown of the Drude model arises from the small number of transverse modes present in the constricted device. When this number is macroscopic, then the constriction essentially continuously reduces the number of transverse modes at a given energy, and therefore the plot is linear. However, if the number of modes is sufficiently small, then the continuous tuning of the negative voltage will at some point sharply reduce the number of transverse modes by one. This is the reason for the step-like evolution of the conductance.

Suppose now that instead of a width constriction we reduce the length between the terminals. Based on Ohm's Law we expect the conductance to diverge, and the resistance to decrease to zero if the length is reduced to a few nanometers, so that the scatterer is ballistic. However, what we find instead is that the resistance approaches a limiting value and does not decay further [73]. This seems to contradict both the Drude model and our previous considerations regarding ballistic transport. How can a device have resistance if it is ballistic? The answer again highlights a major blind spot of the Drude model, the neglection of the quantized transverse modes in the conductor.

Clearly, the Drude model is incapable of describing mesoscopic transport, and we require a new approach that encompasses quantum effects. A theoretical model developed for quantum transport, called the Landauer-Büttiker formalism, places at its center of analysis the discrete transverse modes in a mesoscopic conductor, and the probabilities that electrons injected in one side of a conductor transmit to another terminal. We proceed now to this fascinating approach.

3.4 The Landauer-Büttiker formalism

The Landauer-Büttiker approach essentially consists of expressing the conductance of a mesoscopic conductor in terms of the *transmission probabilities* that charge carriers have of passing through it. Originally conceived to calculate the current-voltage characteristics of tunneling junctions with small transmission probabilities, it has become the main paradigm for the analysis of mesoscopic experiments. So much so that the Landauer relation is often referred to as Ohm's Law of mesoscopic physics. Moreover, this approach is intuitively very appealing, since it seems correct that the conductance is related to the ability of electrons to pass throughout a device. However, even within this framework, not all mesoscopic phenomena are easy to interpret, and it has taken several decades for researchers to develop the field.

For simplicity, we will start with with zero-temperature quantum transport. We will also

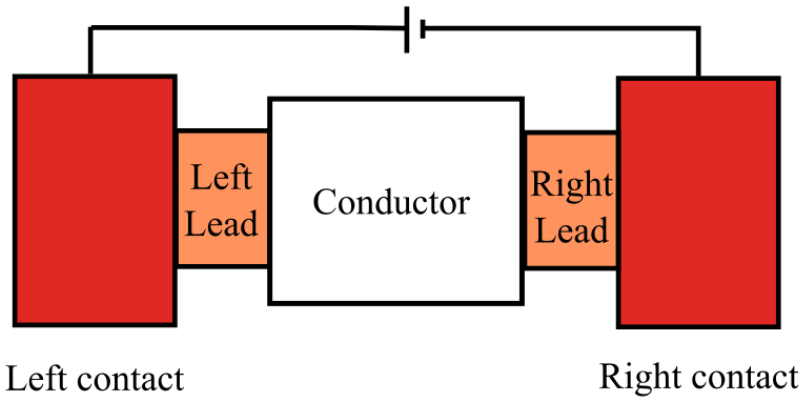

Figure 3.3: A simple two-terminal setup. Both leads are assumed to have the same number of modes M.

restrict our analysis to a two-terminal rectangular device, and assume that the transmission properties are uniform over the range of energies in which transport takes place. This effectively reduces the transport to a single energy channel. Once we develop the appropriate physical intuition for these systems, we will increase the complexity and discuss multi-terminal devices with different energy channels at non-zero temperatures. Finally, we will consider that the leads connecting the scatterer to the contacts, both identical in structure, are large enough to be considered semi-infinite, so that we can impose periodic boundaries along the current axis.

Consider a simple two-terminal device like the one shown in Fig. 3.3. We assume that the type of contacts we are dealing with are '*reflectionless*'. By this we mean that the electrons inside the leads can enter the contacts without reflection. This assumption greatly simplifies our analysis, since otherwise we would have to include an infinite number of reflected waves to calculate the current. Fortunately, numerical calculations indicate that as long as the energy level is not near the bottom of the bands, reflection from narrow conductors to wide ones is marginal. We note that reflections from the contacts into the scatterer (*i.e.* the conductor in Fig. 3.3) can of course be quite large. In fact we expect them to be large. It is only in one direction, from the narrow conductor to the contact, that this assumption is justified.

We can now proceed to calculate the Landauer formula. The narrow mesoscopic conductor depicted in Fig. 3.3 has a couple of identical leads attached to it with a finite number of transverse modes. The left lead is attached to a reservoir with a chemical potential μ_L, and the right lead to another reservoir with chemical potential μ_R. Let $\mu_L > \mu_R$. Each of the transverse modes has a dispersion relation $E(N,k)$ with a cut-off energy $\varepsilon(N,k=0)$. This cut-off represents the minimum energy of each transverse mode. Thus, the mode will not propagate at energies bellow $\varepsilon(N,k=0)$. The number of transverse modes at a given energy E is therefore equal to the sum of modes having energy cut-offs smaller than E:

$$M(E) = \sum_N \theta(E - \varepsilon_N). \tag{3.13}$$

Consider a single transverse mode in the left lead whose $+k$ states are occupied according to some function $f^+(E)$. The current of a simple electron gas is $I = env$, where n is the electron density and v the velocity. The electron density of a single k state in a one-dimensional conductor of length L is simply $1/L$. Therefore we can write the incoming current carried by the $+k$ states in the left lead as

$$I_L^+ = \frac{e}{L}\sum_k v f^+(E) = \frac{e}{L\hbar}\sum_k \frac{\partial E}{\partial k} f^+(E) = \frac{2e}{h}\int_\varepsilon^\infty dE f^+(E), \tag{3.14}$$

where ε is the energy cut-off of the mode. We used the common transcription $\sum_k \to 2 \times \frac{L}{2\pi}\int dk$ to facilitate calculations. To extend this result to transport with many modes, we need only add Eq. 3.13 to this expression:

$$I_L^+ = \frac{2e}{h}\int_{-\infty}^\infty dE f^+(E) M(E). \tag{3.15}$$

Surprisingly, the current is totally independent of the dispersion relation $E(k)$ of the bands, and depends only on the number of modes in the range of energies where transport takes place. The current per mode of a fully occupied state is $2|e|/h \approx 80\,\text{nA/meV}$. The outflux to the right lead is simply the incoming current times the transmission probability $T(E)$ that an electron transmits through the scatterer:

$$I_R^+ = \frac{2e}{h}\int_{-\infty}^\infty dE f^+(E) M(E) T(E). \tag{3.16}$$

The rest of the current is reflected back to the left reservoir, where it empties without reflection:

$$I_L^- = \frac{2e}{h}\int_{-\infty}^\infty dE f^+(E) M(E)(1 - T(E)). \tag{3.17}$$

Finally, the net current is

$$I = I_L^+ - I_L^- = \frac{2e}{h}\int_{-\infty}^\infty dE f^+(E) M(E) T(E). \tag{3.18}$$

If the voltage bias $V = (\mu_L - \mu_R)/e$ is small, then the transmission probability $T(E)$ is approximately constant within the range of energies $E \in [\mu_R, \mu_L]$. We call this the *linear response regime*. Similarly, we can generally assume that $M(E)$ is roughly constant in this energy range. Now, at zero-temperature $f^+(E) = 1$ at energies bellow μ_L. Moreover, the current outside the bias is fully compensated from incoming electrons from both terminals, so we can consider $f^+(E) = 1$ if $E \in [\mu_R, \mu_L]$ and $f^+(E) = 0$ elsewhere. Thus we obtain the following relation:

$$I = \frac{2e}{h} MT \int_{-\infty}^\infty dE f^+(E) = \frac{2e^2}{h} MT \frac{\mu_L - \mu_R}{e} = \frac{2e^2}{h} MTV. \tag{3.19}$$

From this equation we can extract the conductance of the scatterer:

$$G = \frac{2e^2}{h} MT, \tag{3.20}$$

which is the famous Landauer relation. Note that even in the case of a two-terminal ballistic conductor the transmission probability may be less than unity, due to several factors, like mismatches between the leads and the conductor, phase interference or geometric defects. Moreover, a static scatterer might induce partial reflections even if it does not affect the phase-relaxation length of the device.

Let us now consider whether a ballistic conductor can have any resistance. Assume that the leads are of the same structure as the conductor, and therefore $T = 1$ in Eq 3.20. Previously, in Sec.3.1.2, we noted that ballistic transport is free of scattering. Therefore, we could naively interpret this fact to imply that the resistance of the conductor is zero. However, experiments show that the measured conductance of this device approaches a limit value G_c when the length of the conductor becomes much smaller than the mean free path. Where does this resistance (G_c^{-1}) come from? Before electrons are injected into the conductor they must first transmit through the boundary between the contact and the leads. The contacts and the scatterer are very different systems, the reservoirs have effectively an infinite number of transverse modes, while the mesoscopic conductor has a very finite number of them. The enormous confinement of the transverse modes available between the scatterer and a contact creates an interface resistance due to the redistribution of the current-carrying modes. For this reason G_c^{-1} is called the contact resistance.

We can calculate G_c^{-1} from Eq. 3.20:

$$G_c^{-1} = \frac{h}{2e^2 M} \approx \frac{13\text{k}\Omega}{M}. \tag{3.21}$$

Remarkably, the contact resistance of a ballistic conductor with ten transverse modes is $\approx 1\text{k}\Omega$. We can see why the contact resistance is not important in macroscopic devices. If M is macroscopic, then the contact resistance is effectively zero. In a typical field effect transistor, contact resistance is usually in the few Ω range.

3.4.1 Multi-terminal devices: The Büttiker relation

The Landauer relation neatly describes mesoscopic transport in terms of the number of transverse modes available in a mesoscopic conductor/scatterer, and the transmission probability that electrons travel through it. However, for some time there was a great deal of ambiguity regarding the interpretation of four-terminal measurements. Büttiker found a simple solution to this problem. He treated all terminals as voltage probes and focused on the currents and voltages measured in them, completely bypassing any questions regarding the internal state of the conductor. Starting with the two-terminal linear response formula (Eq. 3.19), he simply summed over all terminals. The current in the $i-th$ lead is given by

$$I_i = \frac{2e}{h}\sum_j [\bar{T}_{ji}\mu_i - \bar{T}_{ij}\mu_j] = \sum_j [G_{ji}V_i - G_{ij}V_j], \tag{3.22}$$

where $\bar{T}_{ij}$ is the total transmission probability from lead j to i (including all incoming and outgoing modes), $G_{ij} = (2e^2/h)\bar{T}_{ij}$ the total conductance from lead j to i, and $V_i = \mu_i/e$ the voltage at the $i-th$ contact. The coefficients G_{ij} must follow the summation rule to ensure that the current is zero when all the potentials are equal:

$$\sum_i G_{ij} = \sum_j G_{ij}. \tag{3.23}$$

Therefore we can rewrite Eq. 3.22 as follows

$$I_i = \sum_j G_{ij}[V_i - V_j]. \tag{3.24}$$

This is the famous Büttiker relation that expands the Landauer formula to multi-terminal devices. The remarkable simplicity of this relation makes it a very useful tool. In Chapter 5 we will utilize a four-terminal setup, so let us write Eq 3.24 in its matrix form for this case. The right side of Eqs. 3.22 for a four-terminal setup leads to the following matrix:

$$\begin{pmatrix} I_1 \\ I_2 \\ I_3 \\ I_4 \end{pmatrix} = \begin{pmatrix} G_{12}+G_{13}+G_{14} & -G_{12} & -G_{13} & -G_{14} \\ -G_{21} & G_{21}+G_{23}+G_{24} & -G_{23} & -G_{24} \\ -G_{31} & -G_{32} & G_{31}+G_{32}+G_{34} & -G_{34} \\ -G_{41} & -G_{42} & -G_{43} & G_{41}+G_{42}+G_{43} \end{pmatrix} \begin{pmatrix} V_1 \\ V_2 \\ V_3 \\ V_4 \end{pmatrix}. \tag{3.25}$$

The corresponding system of equations is not linearly independent. We can reduce the dimension of the system by one if we ground one of the terminals, *i.e.* if we set $V_i = 0$ at a given contact. This leads to a linearly independent system with a non-singular matrix, and therefore an invertible matrix. The resistance matrix is defined as the inverse of the reduced conductance matrix $R = G^{-1}$.

3.4.2 Non-zero temperature

In a two-terminal setup, at zero temperature all transport takes place in the energy range $\mu_R < E < \mu_L$. Bellow this range of energies the current is fully compensated in both directions, and above it there are no available states to transport current. However, at finite temperature the Fermi distribution of electrons in the contacts must be taken into account. The thermal broadening of the occupation distribution of electrons implies that transport takes place through multiple energy channels in a wider range $\mu_R - nk_BT < E < \mu_L + nk_BT$, where n is a small positive integer. In other words, transport at finite temperatures also takes place at energies a few multiples of k_BT away from the energy bias between the two contacts.

The current density $\mathscr{I}(E)$, *i.e.* the integrand in Eq.3.18, can be written as

$$\mathscr{I}(E) = \frac{2e}{h} M(E)T(E)[f_L(E) - f_R(E)], \tag{3.26}$$

where $f_{L|R}$ are the occupying distributions of electrons in the left and right leads respectively (notice that $f^+ = f_L - f_R$). The occupation functions $f_{L|R}$ are not in equilibrium and therefore are not Fermi-Dirac distributions. However, notice that if both contacts are held at the same potential, this equation predicts zero current. At zero-current, $f_{L|R}$ are indeed Fermi-Dirac distributions. From this point of equilibrium, we can Taylor-expand in energy the difference between the Fermi distributions $(f_L(E) - f_R(E))$. Therefore, for small biases we can write

$$\delta f = (f_L(E) - f_R(E)) \approx -(\mu_L - \mu_R)\left(\frac{\partial f_0}{\partial E}\right), \tag{3.27}$$

where f_0 is now the equilibrium distribution for electrons, *i.e.* the Fermi-Dirac distribution. Finally, the linear-response finite temperature conductance is given by the following expression

$$G(E) = \frac{e}{\mu_L - \mu_R} \int d\tilde{E} \mathscr{I}(\tilde{E}) = \frac{2e^2}{h} \int d\tilde{E} \Big(- \frac{\partial f(\tilde{E} - E)}{\partial \tilde{E}} \Big) \bar{T}(\tilde{E}), \tag{3.28}$$

where $f(E) = 1/(e^{\beta E} + 1)$, $\beta = 1/(k_B T)$ and $\bar{T}(E) = M(E)T(E)$. Recall that in the linear response regime, the number of transverse modes M and the transmission function T can be assumed roughly constant, so that $\bar{T}(E) = \bar{T}$. In the limit of zero temperature the derivative inside the integral becomes the delta function, and we recover the previous expression (Eq. 3.19).

3.4.3 The scattering Matrix and its relation to the conductance

Thus far we have described the current flow in terms of the transmission function $\bar{T}$ without detailing how to calculate this function. We will now discuss the relationship between the transmission function and the scattering matrix S (or $S-$matrix). The $S-$matrix is a fundamental concept in quantum transport theory that describes how electrons scatter as they move through a conductor, encapsulating all the information about transmission and reflection processes.

A coherent conductor can be characterized at each energy by an $S-$matrix that relates the outgoing wave amplitudes to the incoming wave amplitudes at the different leads. To ensure conservation of probability (no loss of particles), the $S-$matrix must be unitary. At any given energy E, we denote the number of propagating modes at lead i by $M_i(E)$. The total number of modes is obtained by adding the modes of each lead in the device $M_T(E) = \sum_j M_j(E)$. The $S-$matrix is of dimensions $M_T \times M_T$.

Let us first consider a very simple system, the two-terminal device depicted in Fig. 3.3. Moreover, assume that there is only one mode in each lead. Then, the $S-$matrix is a simple 2×2 matrix

$$\begin{pmatrix} b_L \\ b_R \end{pmatrix} = \begin{pmatrix} r & t' \\ t & r' \end{pmatrix} \begin{pmatrix} a_L \\ a_R \end{pmatrix} = S \begin{pmatrix} a_L \\ a_R \end{pmatrix}, \tag{3.29}$$

where a_L, a_R are the amplitudes of the incoming electrons from the left and right leads respectively, b_L, b_R the amplitudes of the outgoing waves, r, r' are the reflection amplitudes for waves incident from the left and right respectively, and t, t' the corresponding transmission amplitudes. As we can see the $S-$ matrix simply relates all the incoming and outgoing modes through coefficients that represent the probabilities of transmission and reflection. We can now expand this to multi-terminal devices with multiple modes per lead: let $a_{i,n}$ and $b_{i,n}$ represent the incoming and outgoing amplitudes of waves in lead i and mode n. Then the $S-$matrix can be written as

$$b_{i,n} = \sum_j \sum_i S_{i,n;j,m} a_{i,m}, \tag{3.30}$$

where $S_{i,n;j,m}$ is the $S-$matrix element describing the scattering amplitude from the incoming mode m in lead j to the outgoing mode n in lead i.

We are interested now in relating this $S-$matrix to the transmission function $\bar{T}$. The transmission probability T_{nm} from mode m to n is obtained by taking the squared magnitude of the corresponding element of the $S-$matrix

$$T_{nm} = |S_{nm}|^2. \tag{3.31}$$

To obtain the transmission function $\bar{T}_{ij}$ we have to sum over all modes in each of these leads:

$$\bar{T}_{ij} = \sum_{m \in j} \sum_{n \in i} T_{nm} \tag{3.32}$$

Finally, we can relate the conductance matrix G to the $S-$matrix as follows:

$$G_{ij} = \frac{2e^2}{h} \bar{T}_{ij} = \frac{2e^2}{h} \sum_{m \in j} \sum_{n \in i} |S_{i,n;j,m}|^2. \tag{3.33}$$

The $S-$matrix of a coherent conductor can be calculated directly using the effective mass Schrödinger equation. Once the $S-$matrix is calculated, the conductance is easily extracted using this relation. In the next chapter we will see how we can implement this method numerically.

3.5 Summary

In this chapter we gave a brief overview of the theory of quantum transport. We showed how Ohm's law is incapable of describing mesoscopic phenomena, and how the Landauer-Büttiker approach allows for a consistent and intuitive interpretation of mesoscopic experiments. The conductance of a mesoscopic conductor is determined by the number of transverse modes and

a transmission function which describes the probability that injected electrons pass through the scatterer. A multi-terminal experiment can be analyzed using the Büttiker relation, in which we focus uniquely on the voltage-current characteristics at each terminal and bypass any information regarding the inner states of the scatterer. We further discussed the linear response regime, where the number of modes and the transmission function is assumed to be constant and the conductance is proportional to the small applied bias. Next, we showed how the conductance changes at non-zero temperature, where we find the thermal smearing of energy channels that contribute to the current. Finally, we saw how the $S-$matrix formalism relates to the transmission function and derived the conductance matrix for multi-terminal devices with multi-moded transmission. In the next chapter we will see how this fascinating theory can be implemented in numerical simulations.

CHAPTER 4

NUMERICAL METHOD

The theory of coherent quantum transport, introduced in the previous chapter, provides a powerful tool for studying the electronic properties of materials at the mesoscopic scale. Quantum transport simulations are a key ingredient in our approach to study the electronic properties of magic-angle twisted bilayer graphene. Specifically, we use the energy-resolved conductance of a large mesoscopic sample to derive information about the low-energy quasi-flat moiré bands that are characteristic of this two-dimensional material. These numerical simulations prepare the ground for future experiments, and provide guidance in the interpretation of measurements of real devices. Moreover, they align well with experimental studies already reported in the scientific literature. We emphasize that, given the size of the devices required for quantum transport calculations, a numerical approach based on the tight-binding method is the only one capable of handling the amount of computation required.

Computer simulations play a central role in condensed matter physics, serving as an indispensable tool for understanding and predicting the behavior of complex systems that are often intractable by purely analytical methods. These systems typically involve a large number of interacting particles, making exact solutions to the underlying equations extremely difficult or even impossible to obtain analytically. Even in non-interacting systems, such as the tight-binding model, the number of atoms present in realistic devices is enormous. This is especially true in the case of twisted bilayer graphene, where we study electron correlations at the scale of the moiré unit cell. For simulations to contain information about electron correlations at such scale, the devices simulated should have at least a few tens of moiré unit cells. Recall that near the first magic angle $\theta_m \approx 1.05^\circ$ the moiré translation length is more than 10 nm long. This means that each moiré unit cell has tens of thousands of atoms. Computer simulations are thus the only way to bridge the gap between theory and experiment by providing a means to solve these equations numerically.

There are various techniques that have been developed for numerical simulations of materials. Molecular dynamics simulations model the motion of atoms and molecules over time, providing insight into structural and dynamical properties. Monte Carlo methods use random sampling to construct statistical ensembles, and are often useful for simulating systems with many coupled degrees of freedom or with significant uncertainty in their inputs. In the case of condensed matter physics, quantum Monte Carlo techniques are useful to study quantum many-body problems. Density functional theory simulations focus on the computation of the electronic structure, enabling the prediction of material properties such as band structures and binding energies. Coarse-grained models simplify complex systems by grouping particles into larger units. And there are many more numerical techniques, each typically tailored for a specific problem. In this work, we focus primarily on probing the electronic properties of twisted bilayer graphene via solving the scattering problem in large mesoscopic devices, within the coherent transport regime (see Sec.3.1.2). In other words, we are interested in the transmission characteristics between incoming and outgoing leads attached to a finite scatterer made of this two-dimensional material. These leads simulate contacts attached a sample, and therefore our method has a direct bridge between theory and experimental measurements of real devices. In addition to solving the scattering problem, we need to calculate the spectrum and the density of states of twisted bilayer graphene to compare the energy-resolve conductance with spectral features. This is much easier, because for this we just need to impose periodic boundary conditions on the moiré unit cell and solve the Bloch Hamiltonian. For tight-binding systems, such operations are not computationally expensive.

Solving the scattering problem is one of the most common and general tasks in condensed matter physics. Since the early days of mesoscopic physics, the use of computer simulations has been one of the main pillars of research. One of the first developed and most widely used algorithms to solve the scattering problem is the recursive Green's function method. However, this approach is restricted to quasi-one dimensional geometries and to a particular type of tight-binding Hamiltonian. Due to these limitations, this method is insufficient for our purpose, we need an efficient algorithm for solving the scattering problem for arbitrary one-particle tight-binding Hamiltonians. Fortunately, there is now a Python-based numerical package that does exactly this. This useful tool is called *kwant* [86]. It is a powerful and easy-to-use package that is uniquely suited to the kind of mesoscopic experiments we need to simulate. First of all, this package can handle any quantum system as long as it is defined by a tight-binding Hamiltonian. Thus, this method fits very well with our theoretical description of twisted bilayer graphene. Moreover, this package has a comprehensive set of tools for the analysis of quantum transport, which greatly facilitates the understanding of the system and its transport-related properties. For example, the user can quickly calculate the scattering wave function's probability weights to see if the modes are localized or delocalized throughout the scatterer. Finally, it is remarkably well-optimized, which is of fundamental importance given the large sizes of the moiré devices we

need to simulate.

In this chapter we explain the functionality of Kwant, and prepare the groundwork for the simulations we used for the results discussed in chapters 5 and 6. The authors of this excellent numerical toolkit provided an explanation of kwant's functionality in a published work in 2014 [86], and they also produced an online tutorial that provides a hands-on approach (available at https://kwant-project.org). We try not to repeat the argumentation of the authors, but to provide a more detailed explanation of the method this package is based on in 4.1 and we also detail the steps for a simple example. Firstly, we introduce kwant in Sec. 4.1 and describe its workflow. Next, we present the essential theory of how kwant solves the scattering problem in Sec. 4.2. We then show a thorough explanation for a simple one-dimensional chain in Sec. 4.3. We note that we do not discuss in detail the specific code we use to implement these simulations. This is because in both of our published works [20, 24] we included the source code and all the data for the results shown in chapters 5 and 6. In addition, we believe that the online tutorial does an excellent job of explaining the coding details of this package, and there is nothing that we need to add.

4.1 Introducing kwant

Kwant is a free software package for quantum transport based on the Python programming language. Its goal is to solve the scattering problem of any system described by a tight-binding Hamiltonian. By "system" we mean a finite scattering region connected to as set of semi-infinite leads, which model the electrodes of physical experiments. The scattering problem consists essentially in calculating the $S-$matrix, which relates the outgoing modes to the incoming modes through transmission and reflection probabilities (see Sec. 3.4.3). In addition, we can calculate the scattering wave functions to obtain more information about the sample's properties. The scattering matrix and the scattering wave functions are the two main outputs of kwant's principal object class. However, kwant also provides several optimized functions to calculate derivative quantities of these outputs, such as the conductance, shot noise, spin currents, Peltier and Seebeck coefficients, local density of states, current density, and others. Finally, this package also includes many methods to facilitate the understanding of the simulated system, such as functions to easily visualize the structure of the scatterer, to plot the scattering wave-functions probability weights, or to extract the number of propagating modes in a lead at a specific energy.

The workflow of Kwant can be generically described as follows: (1) Define a system by specifying the lattice structure (the positions of the sites in the scatterer and in the leads) and setting the tight-binding Hamiltonian of the system. (2) Attach the leads to the scatterer and obtain the Hamiltonian of the entire system after coupling the scatterer with the leads. (3) Solve the scattering problem (calculate the $S-$ matrix and the scattering wave functions inside the scatterer). In the next sections, these steps will be explained in detail. The online tutorial

(https://kwant-project.org) provides several examples with detailed explanations, as well as the source codes to implement these simulations using any updated Python compiler. We believe it is not necessary to repeat these examples in this work. We instead focus our efforts on explaining in detail the numerical solution to the scattering problem using the wave function formulation kwant uses, without dwelling on the technical details.

4.1.1 Defining a system

In kwant, a finite scatterer is created by specifying its geometry and tight-binding Hamiltonian. By geometry we mean the graph corresponding to the lattice to be simulated. The scattering region must be represented by a discrete set of points in a lattice, connected through lines which represent the hopping amplitudes between sites. The user then specifies the Hamiltonian of the scatterer, *i.e.* the on-site Hamiltonians and the hoppings between sites, on a site-by-site basis. The lattice can be adapted to represent low-dimensional geometries, such as one-dimensional chains, or it can be written in three-dimensional space. There are many methods in this package that facilitate the process of lattice formation so that the user does not have to add sites one-by-one specifying the position of each site.

In the language of first quantization, we can write the Hamiltonian of the scattering region in the following way:

$$\hat{H} = \sum_{ij} H_{ij} |i\rangle \langle j| , \tag{4.1}$$

where $|i\rangle = |\mathbf{r}, \alpha\rangle$ corresponds to a site at position $\mathbf{r}$ and α denotes its internal degrees of freedom. These can represent the spin, orbital, or any other internal degree of freedom, as long as they are expressed in matrix form. The diagonal components H_{ii} contain the on-site energies of the system, and the off-diagonal components $H_{ij\neq i}$ correspond to the hopping amplitudes between sites.

Kwant is designed to perform quantum transport simulations on systems defined in a lattice, but this does not mean that they have to correspond directly to the atomic positions of a real crystal. For example, the Hamiltonian can be represented in reciprocal space, and both the on-site energy and the hoppings can therefore be functions of the quasi-momentum. Or the Hamiltonian can represent an effective, discretized system that describes approximately a *de facto* continuous problem. The user can also find other kinds of effective descriptions of systems, where the lattice sites in kwant correspond to scaled-up microsystems, which is a useful method in cases where the system size is too big to handle even for a tight-binding system. As long as a quantum system can be represented by a connected network of sites described by Hermitian matrices, kwant is capable of performing quantum transport calculations on it.

This package is capable of calculating the energy levels of finite systems by simply diagonalizing the Hamiltonian. If the Hamiltonian is written as a function of the quasi-momentum, then

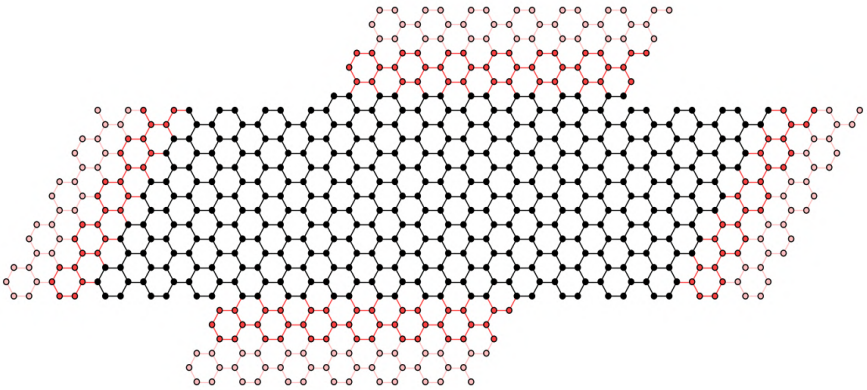

Figure 4.1: Example of a Kwant system. A parallelogram-shaped graphene scattering region is attached to four graphene leads.

diagonalization of the Hamiltonian of a finite lattice yields an approximation to the dispersion relation. However, the main focus of this package is on quantum transport calculations. As described in Sec. 3.4, the Landauer-Büttiker formalism allows us to represent the electrodes in a mesoscopic experiment as semi-infinite leads with a number of propagating modes that transport current. These leads act as waveguides that direct plane waves into and out of the scattering region. In Kwant, leads are simply tight-binding systems with a translational symmetry. Therefore electrons in the leads have dispersion relations along the axis of translational symmetry. At a given energy level, current is carried from the incoming to the outgoing transverse modes that cross that energy level. These leads are subsequently attached to the scattering region, *i.e.* the wave-functions at the interface are equated. Boundary conditions are thus imposed at the interface between the leads and the scatterer.

Figure 4.1 shows a four-terminal experiment on a sheet of graphene modeled using kwant. The scatterer is attached to four electrodes, all essentially graphene nanoribbons with one translation symmetry. Sites belonging to the scattering region are shown as black dots, and sites belonging to the four semi-infinite leads are shown as red dots. The fading red sites in the leads represent the axis of translational symmetry. Hoppings between sites are shown as lines, black in the scattering region and red in the leads. Thus, this system corresponds to the nearest neighbor hopping model of graphene, since only the nearest adjacent sites are connected to each other.

Consider the following problem: Suppose we want to attach leads of one lattice geometry to a scatterer with a different geometry. Looking at Fig. 4.1, we can see that there is no obvious way to connect leads and scatterers of different symmetries. The user should have a way to model the connection between the scatterer and the leads if they have different symmetries. Kwant automatically does this when the symmetries match, and therefore it is recommended to not change the lattice geometry between the leads and the sample. A kwant user should always be

aware of the limitations on the physical structure of the devices that can be simulated.

4.2 Kwant's method for solving the scattering problem

Once we have the complete system, consisting of the finite scatterer and the semi-infinite leads, the next step is to solve the scattering problem. Kwant is based primarily on the wave-function formulation of the this problem, although it can be used to obtain the non-equilibrium Green's functions. In essence, the scattering problem is solved by computing the scattering matrix (S-matrix), which we shortly discussed in the previous chapter. To do this, kwant first calculates the modes of the semi-infinite leads, solving the Bloch Hamiltonian *at a given energy*. Kwant does not calculate the energy dispersion of these leads, since only the modes at a given energy are relevant to quantum transport. Then, kwant fits the wave-functions of the scattering region to the incoming and outgoing modes in the leads at the interfaces. Finally, the Schrödinger equation is reduced to a simple system of linear equations, which can be solved efficiently. We will now describe this process in detail.

For simplicity, we will assume that there is only one lead attached to the scatterer. Multiple leads can be considered as a single disjoint composite lead, so this has no consequence for our results and it greatly simplifies notation. Let H_{scat} be the Hamiltonian of the scatterer, and H_{lead} the Hamiltonian of one unit cell in the lead. Next, let V_{lead} represent the hoppings matrix that couples the unit cells in the lead with each other, and V the hoppings matrix that couples the scattering region to the first unit cell of the lead. The total Hamiltonian of the infinite system can therefore be written as:

$$\hat{H} = \begin{pmatrix} \ddots & V_{\text{lead}} & & \\ V_{\text{lead}}^{\dagger} & H_{\text{lead}} & V_{\text{lead}} & \\ & V_{\text{lead}}^{\dagger} & H_{\text{lead}} & V \\ & & V^{\dagger} & H_{\text{lead}} \end{pmatrix}. \tag{4.2}$$

We can thus express the wave functions of the whole infinite system as $\left(\cdots, \psi_2^{\text{lead}}, \psi_1^{\text{lead}}, \psi^{\text{scat}}\right)^T$, where ψ^{scat} is the wave function of the scattering region and ψ_i^{lead} the wave-function of the $i-$th unit cell in the lead. Now, the translational symmetry of the leads implies that the wave functions take the form of Bloch waves. Thus, the eigenstates can be written as

$$\phi_{j,n} = e^{ik_n ja} u_n, \tag{4.3}$$

where a is the lattice constant of the leads, n labels the eigenfunctions in one unit cell and u_n is a function with the same periodicity as the unit cell. We can classify the modes depending on the wave vector k_n. If k_n is real, the oscillating solution corresponds to plane waves and we call them *propagating modes*. If k_n is imaginary, then the exponent must be negative, and therefore

the wave function has an exponentially decaying amplitude. We call these *evanescent modes*. Solutions with a positive real exponent are not physical.

The Hamiltonian of one lead unit cell coupled to its neighbors, with $j > 1$ so that it is not in the interface with the scattering region, is given by:

$$H = H_{\text{lead}} + V_{\text{lead}} + V_{\text{lead}}^{\dagger}. \tag{4.4}$$

Inserting the Bloch waves from Eq. 4.3 into the Hamiltonian 4.4 yields:

$$H_{\text{lead}}\phi_{j,n} + V_{\text{lead}}\phi_{j,n+1} + V_{\text{lead}}^{\dagger}\phi_{j,n-1} = \left(H_{\text{lead}} + V_{\text{lead}}e^{-ik_n a} + V_{\text{lead}}^{\dagger}e^{ik_n a}\right)u_n = E_n u_n. \tag{4.5}$$

Now, kwant does not calculate the energy dispersion of the whole periodic lead, because this would be computationally demanding. Instead, the user sets a specific energy E and kwant calculates the modes that cross this energy level. This is done so by linearizing the Schrödinger equation to a generalized eigenvalue equation of the form

$$\begin{bmatrix} 0 & \mathbb{I} \\ -V_{\text{lead}}^{\dagger} & (E\mathbb{I} - H_{\text{lead}}) \end{bmatrix} \begin{bmatrix} \phi_{j,n} \\ e^{ik_n}\phi_{j,n} \end{bmatrix} = e^{ik_n} \begin{bmatrix} \mathbb{I} & 0 \\ 0 & V_{\text{lead}} \end{bmatrix} \begin{bmatrix} \phi_{j,n} \\ e^{ik_n}\phi_{j,n} \end{bmatrix}, \tag{4.6}$$

where $\mathbb{I}$ is an identity matrix of the same dimension as H_{lead}. The propagating modes are normalized according to the expectation value of the particle current operator I, so that

$$\langle I \rangle \equiv 2\text{Im}\,\langle \phi_{j,n} | V_{\text{lead}} | \phi_{j-1,n} \rangle = 2\text{Im}\left(e^{-ik_n a}\langle u_n | V_{\text{lead}} | u_n \rangle\right) = \pm 1. \tag{4.7}$$

We distinguish *incoming modes* ϕ_n^{in} ($\langle I \rangle = 1$) from *outgoing modes* ϕ_n^{out} ($\langle I \rangle = -1$). In the case of evanescent modes ϕ_n^{ev} we have a vanishing particle current $\langle I \rangle = 0$. All in all, the scattering wave functions in the conductors can be written as superpositions of incident, outgoing and evanescent modes:

$$\psi_j^{\text{lead}} = \sum_n a_n \phi_{j,n}^{\text{in}} + \sum_m b_n \phi_{j,m}^{\text{out}} + \sum_l c_l \phi_{j,l}^{\text{ev}}. \tag{4.8}$$

In the previous chapter we saw that the scattering matrix ($S-$matrix) by definition relates the incoming and outgoing modes:

$$b_n = \sum_n S_{nm} a_n. \tag{4.9}$$

Furthermore, the normalization condition implies that the coefficients of the incoming modes are all $a_n = 1$. Thus, the scattering wave functions in the leads can be written as

$$\psi_j^{\text{lead}} = \sum_n \left(\phi_{j,n}^{\text{in}} + \sum_m S_{mn}\phi_{j,m}^{\text{out}} + \sum_m \tilde{S}_{mn}\phi_{j,m}^{\text{ev}}\right), \tag{4.10}$$

where S is the scattering matrix and $\tilde{S}$ is a matrix that relates the evanescent modes to the incoming modes. We are typically interested only in calculating S, since the evanescent modes do not contribute to the current.

The $S-$matrix and the wave function in the scatterer ψ^{scat} are both calculated by matching ψ^{scat} with the wave function ψ_1^{lead}. Continuity of the wave function demands that $\psi_{\text{scat}} = \psi^1_{\text{lead}}$ at the interface. This is achieved in kwant by solving a discretized version of the Schrödinger equation for each incoming mode individually, then placing the above form of the wave function to solve the eigenvalue problem for the whole system, $H\psi = E\psi$ where H is given by Eq. 4.2.

Most transport properties can be derived from S and ψ_{scat}

Recall from Sec. 3.4.3 that the differential conductance $G_{ij} = dI_i/dV_j$, where i, j label two leads, is related to the $S-$matrix through the relation

$$G_{ij} = \frac{e^2}{h}\tilde{T}_{ij} = \frac{e^2}{h}\sum_{m\in j}\sum_{n\in i}|S_{i,n;j,m}|^2, \tag{4.11}$$

where the indexes n, m label the modes within the leads i, j. In our previous considerations, only one composite lead is attached to the scatterer, so we did not need an extra pair of indexes. Also we note that Eq. 4.11 is slightly different from the equation we derived in Sec.3.4.3. The reason for this is that in this section we did not assume spin degeneracy, and therefore electrons in the leads can have different dispersion relations depending on their spin, and consequently correspond to distinct transverse modes.

4.3 A simple example: Scattering in a one-dimensional chain of atoms

Our discussion thus far described in principle kwant's approach to the scattering problem. To get a feel of how kwant actually calculates the scattering matrix let us consider a very simple example: scattering through a one-dimensional chain of atoms. Two semi-infinite one-dimensional leads to the right and left are connected to a finite array of atoms with n sites. Let a be the lattice constant, equal throughout the whole chain (comprising both the leads and the scatterer). Our goal is to calculate the scattering matrix S, whose components are the transmission and reflection probabilities. Essentially, we want to solve a 1D Schrödinger equation of the form

$$-\frac{\hbar^2}{2m}\frac{d^2}{dx^2}\psi(x) + V(x)\psi(x) = E\psi(x), \tag{4.12}$$

where $V(x)$ is the position-dependent potential in the chain. For simplicity, let us consider $V(x) = 0$ for $0 \le x \le L = na$, which implies that the leads correspond to grounded contacts. This equation is a continuous one, and our discrete lattice is described by a tight-binding Hamiltonian. To relate this Schrödinger scattering equation to our tight-binding Hamiltonian, we can approximate the second derivative in the following manner:

$$\frac{d^2}{dx^2}\psi(x) \approx \frac{1}{a^2}[\psi(x–a)–2\psi(x)+\psi(x+a)].$$

Using this expression, we can rewrite the Schrödinger equation in a discrete form:

$$-t\psi_{n-1}+(V_n+2t)\psi_n–t\psi_{n+1}=E\psi_n, \tag{4.13}$$

where $t=h^2/2ma^2$, $\psi_n=\psi(x=na)$, and $V_n=V(x=na)$. To simplify this equation, we set $t=1$ and $V_n'=V_n+2t$. The *discretized Schrödinger equation* is then

$$-\psi_{n+1}-\psi_{n-1}+V_n'\psi_n=E\psi_n. \tag{4.14}$$

Now, let us describe the transmission characteristics of incoming electrons from the left lead. An electron propagates in the left lead towards the right, and either transmits through the scatterer to the right lead or is reflected back. Thus, to the left of the scatterer, the wave functions have the form of superposed incoming and reflected plane waves:

$$\psi_{n\leq 0}=e^{ikn}+Re^{-ikn}, \tag{4.15}$$

where R represents the *reflection coefficient*. Notice that we set the amplitude of incoming electrons to 1. On the right side of the scatterer, the outgoing electrons are plane waves of the form

$$\psi_{n>L}=Te^{ikn}, \tag{4.16}$$

with T corresponding to the *transmission coefficient*. For this simple problem, we can solve directly the discretized Schrödinger equation inside the leads, where $V(x)=0$, and this yields a cosine energy dispersion:

$$E(k)=-2\cos(k). \tag{4.17}$$

However, we emphasize that in general kwant does not solve the energy dispersion of the periodic leads. It instead solves the linearized version of the generalized eigenvalue problem we described above. This greatly improves efficiency, and reduces numerical demand. A user can calculate the energy dispersion using another method in this package, but it does not calculate it while solving the scattering problem. Next, to obtain the solution for the whole chain, we need to impose the continuity of the wave functions at the boundaries between the leads and the scatterer. In a discrete lattice, this is done by matching the wave functions at four points, $n=0,1,L,L+1$. This sets up a system of essentially five linear equations:

$$
\begin{aligned}
&n = 0 : Re^{e^{-ik}} - \psi_1 = -e^{ik}, \\
&n = 1 : R + (E - V_1')\psi_1 + \psi_2 = -1, \\
&n = p : \psi_{p-1} + (E - V_p')\psi_p + \psi_{p+1} = 0, \\
&n = L : \psi_{L-1} + (E - V_L)\psi_L + Te^{ik(L+1)} = 0, \\
&n = L+1 : \psi_L - Te^{ikL} = 0,
\end{aligned}
$$

where $n = p$ is any point inside the scatterer (excluding the boundaries). We can then rewrite this system of linear equations in matrix form:

$$
\begin{bmatrix}
e^{-ik} & -1 & 0 & \dots & \dots & \dots \\
1 & E - V_1' & 1 & 0 & \dots & \dots \\
\dots & \dots & \dots & \dots & \dots & \dots \\
\dots & \dots & \dots & 0 & E - V_L' & e^{ik(L+1)} \\
\dots & \dots & \dots & 0 & 1 & -e^{ikL}
\end{bmatrix}
\begin{bmatrix}
R \\ \psi_1 \\ \psi_2 \\ \dots \\ \psi_L \\ T
\end{bmatrix}
=
\begin{bmatrix}
-e^{ik} \\ -1 \\ 0 \\ \dots \\ 0 \\ 0
\end{bmatrix}. \tag{4.18}
$$

Finally, to obtain the scattering matrix S, we can repeat this procedure for right-lead incoming electrons scattering towards the left. This yields another two transmission and reflection coefficients, T' and R' respectively. All four coefficients define the scattering matrix:

$$
S = \begin{bmatrix} R & T \\ T' & R' \end{bmatrix}. \tag{4.19}
$$

Once the scattering matrix is computed, the conductance can be extracted using the Landauer-Büttiker theory we described in Chapter 3. Notice that in this chapter we slightly altered the notation introduced in Chapter 3, making the following changes $t \to T$, $r \to R$. This was done to avoid confusing the hopping t with the transmission coefficient T.

4.4 Summary

In this chapter we briefly described the Python-based numerical package kwant, and how it efficiently solves the scattering problem. We explained in principle how kwant approaches the scattering problem, and then explicitly solved a very simple example of a one-dimensional chain of atoms to detail the process. This package is extremely optimized to improve efficiency and reduce random access memory (RAM) requirements. First of all, it stores only non-zero elements of the sparse matrix which represents the whole system (e.g., Compressed Sparse Column (CSC) format). It also uses lower-upper (LU) decomposition (via numerical packages UMFPACK or SuperLU) to factorize the matrix of the system and then utilize efficient sparse linear algebra algorithms. Precisely, kwant's algorithms are taken from the KPM (Kernel Polynomial Method)

or they other efficient direct eigensolvers (e.g., LAPACK) to solve the general eigenvalue problem. All-in-all, kwant constitutes a practical and powerful numerical toolkit, written with the purpose of making quantum transport simulations as efficient and straightforward as possible. In the following chapters we will see that kwant allowed us to simulate enormous devices comprising millions of atoms, and to subsequently extract the scattering matrix and with it the tunneling conductance.

CHAPTER 5

TRANSPORT SIGNATURES OF VAN HOVE SINGULARITIES IN MESOSCOPIC TWISTED BILAYER GRAPHENE

In this chapter we study the low-energy conductance and its relation to the electronic moiré bands of near-magic-angle twisted bilayer graphene. Conductance measurements are a useful tool for studying this interesting material because they are cheap, easy to perform, and provide important information about the properties of charge carriers. Conductance simulations based on the Landauer-Büttiker approach, described in Sec. 3.4, can prove the coupling of the two graphene layers and identify important features in the moiré band structure, such as critical points where electron correlations are strongly enhanced. We recall that our approach is based on a single-particle picture, and thus our analysis of electron correlations is only tangential, by which we mean that we infer that electron correlations become more significant as the electron density of states is sharply increased. Nonetheless, we believe that our method provides a powerful tool for studying the most characteristic feature of this remarkable material: the presence of nearly dispersionless low-energy bands, and their effect on the strongly correlated electron properties of magic-angle twisted bilayer graphene. The numerical method we use to conduct quantum transport simulations is outlined in Chapter 4.

In the Landauer-Büttiker approach, there is no direct, universal equation relating the conductance G to the density of states of the scatterer. Recall that $G(E)$ is directly determined by the transmission probability function $T(E)$, which depends on a number of factors, such as the types of scattering present in the sample and the coupling between the scatterer and the leads. In the case of coherent transport, $T(E)$ depends directly on the overlap of the wave functions in the leads and the scatterer. Thus, for a given mode in the leads, the number of available states in the scatterer near the energy E determines the probability $T(E)$ and hence the conductance $G(E)$. This is most explicit in the case of quantum dots, where resonant tunneling dominates and

$T(E)$ can be approximated by a Breit-Wigner (Lorentzian) function, leading to a proportionality relation $G(E) \propto T(E)$. For this reason, in mesoscopic devices we generally expect the density of states in the scatterer to play a critical role in determining the conductance.

Our method of analysis is novel and powerful, and contributes to the ongoing efforts to understand this remarkable two-dimensional material. Most of the research on twisted bilayer graphene to date has focused on observables in the thermodynamic limit and on transport in macroscopic samples within the semiclassical regime [80, 87], and is therefore limited to the long-wavelength electronic properties. On the other hand, quantum transport studies have mostly focused on more specific questions, such as: the angle-dependent minimal conductivity and the effects of disorder on it [88, 89]; quantum transport across twist-angle domains [81]; magnetic properties of driven and electrically controllable twisted bilayer graphene [90–92]. In addition, quantum transport studies of twisted bilayer graphene often use small devices with scattering regions smaller than the magic-angle moiré unit cell [93–95], and therefore they cannot account for coherent quantum effects on the moiré scale. Our approach allows the researcher to probe the electronic properties in an energy-resolved fashion with remarkable precision, revealing detailed effects arising from the flat band topology. Moreover, conductance simulations of large samples are able to preserve information about coherent quantum effects over the length scale of many moiré unit cells.

We find that the low-energy quantum transport in twisted bilayer graphene is affected by several factors. The main one is the overall flatness of the moiré bands, since this strongly enhances the electron density of states. Van Hove singularities in the bands (see Sec. 2.3.2), due to their diverging density of states, are also very important, and consequently the energy-resolved conductance shows sharp peaks at their respective energy levels. We also find oscillations of the conductance as a function of the system size, whose period does not correspond to the size of the moiré unit cell, indicating a non-trivial interference pattern of the scattering wavefunctions. Surprisingly, non-singular band crossings of the flat bands also show enhanced conductance signatures, although the bulk density of states shows discerning feature at these crossing points. These results indicate that twisted bilayer graphene exhibits strong quantum nonlinearity in its conductance near van Hove singularities, and that it is a remarkably sensitive system with potential applications as a compact high-frequency device and sensitive detector [20].

The organization of this chapter is as follows: we start in Sec. 5.1, where we describe the model and the device we use for our simulations. We also describe in detail the geometry of the devices we use for the quantum transport calculations. Next, in Sec. 5.2 we highlight a very useful feature of our model: the equivalence that changes in the twist angle and the interlayer hopping amplitude have on the moiré spectrum, for small variations of these parameters. This result allows us to bypass the periodicity condition of the twist angle, and continuously tune the moiré band structure in near-magic-angle twisted bilayer graphene. Thus, we can continuously evolve the angle-resolved low-energy spectrum of twisted bilayer graphene and follow the evolution of

van Hove singularities, and of other interesting features inside the quasi-flat bands. Next, in Sec. 5.3 we discuss the Dirac point conductance of twisted bilayer graphene, where we distinguish two regimes: the large angle regime, where the graphene layers are effectively decoupled; and the small angle regime, where the layers are strongly coupled. Then, in Sec. 5.4 we detail the relationship between the moiré bands and the four-terminal conductance of twisted bilayer graphene and discuss our results. Finally, in Sec. 5.5 we give a brief summary.

5.1 Model and setup

Consider a device formed by stacking two crossed graphene nanoribbons, as shown in Fig. 5.1. State-of-the-art experimental techniques are capable of realizing this setup [96]. Remarkably, recent technical advances even allow the continuous tuning of the twist angle and pressure [97]. The graphene ribbons are chosen to have armchair terminations along their finite dimensions, to avoid contributions from edge states to the conductance (in graphene, zigzag termination leads to the localization of the scattering wave functions at the edges of the sample [98]). This results in a parallelogram-shaped overlap region. The upper ribbon is then twisted by an angle θ around a fixed point in space, which is located at the center of the overlap region. At zero twist, the graphene layers are chosen to be stacked in an AA fashion (see the discussion in Sec. 2.2 concerning AA- and AB-stacked bilayer graphene). As explained in Sec. 2.3, the choice of stacking is arbitrary, qualitatively the results are effectively the same if we set the untwisted configuration to AB stacking.

To capture the emergence of moiré physics in our conductance simulations, we need samples with at least a few tens of moiré states, of which we have one per moiré unit cell. Therefore, the system should contain at least a few tens of moiré unit cells (the more the better, of course, but we find that reaching a hundred magic-angle moiré unit cells was not possible in our computers, due to memory overflow, even with 128GB Random Access Memory per computing node). However, at small twist angles ($\theta \approx 1°$) the moiré unit cell is quite large $L_m \approx 120$Å. Therefore, the finite samples for quantum transport simulations should have at least one characteristic length of about a tenth of a micron. The need to diagonalize the scattering matrices, required to extract the conductance matrices, makes this approach computationally intensive. For this work, we used a sample with a rectangular scattering region made of twisted bilayer graphene with approximately 20×4 magic-angle moiré unit cells. This configuration allows us to realize two junctions: one short and wide, and another long and narrow.

The continuation of the graphene nanoribbons outside the overlap region defines four semi-infinite, monolayer graphene leads. (leads 1-4 in Fig. 5.1). We simulate metallic contacts by tuning the chemical potential in the leads μ_L far from the Dirac-point energy and deep into the bulk of the dispersion bands, to include as many modes as possible (in our simulations we use $\mu_L = -2$eV, equal in all terminals). In addition, the Dirac-point energy, here treated as equal to the Fermi

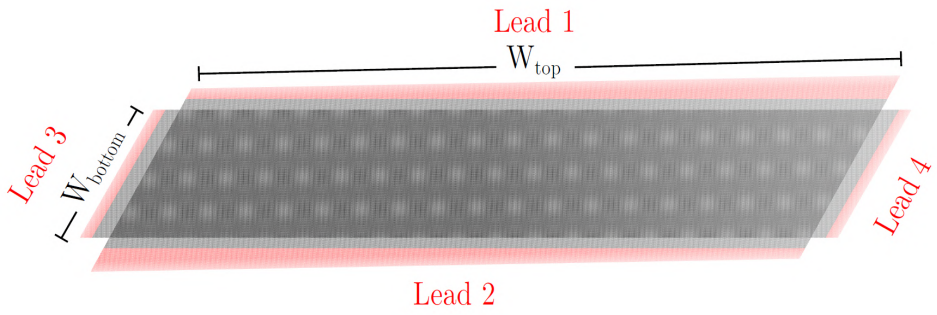

Figure 5.1: Twisted bilayer setup: two crossed graphene nanoribbons with leads (red) form a parallelogram-shaped scattering twisted bilayer region (dark grey area).

level, is always set to $E = 0$. The number of modes crossing the Fermi level in leads 1 and 2 is in the order of tens of thousands, and of thousands in leads 3 and 4. Finally, we note that the twisting of the upper sheet implies that leads 1 and 2 connect with the scattering region closer to the left of the sample than to the right. We account for this factor by adding more sites to the scatterer, and equalizing the chemical potential of these added sites to the one in the leads, *i.e.* μ_L. The additional sites allows us to largely maintain constant the distance between the leads and the scatterer in all contacts and irrespective of the twist angle. This can be visualized in Fig. 5.1, where we see that the red regions, which correspond to the sites where $E = \mu_L$, to the right of the sample are larger. In our simulations this simple workaround effectively made the sample C_2-symmetric.

For a four-terminal setup, the differential conductance G is a 4×4 tensor defined by the relations $G_{ij} = dI_i/dV_j$, where I_i is the current at the i-th lead and V_j is the voltage at the j-th lead of the system. Moreover, our setup has an approximate C_2 symmetry, which is only weakly broken along the boundaries of the system due to its termination, and thus $G_{ij} \approx G_{ji}$. Therefore, our setup has effectively four independent components, which we choose to be the intralayer conductances G_{12} (short and wide junction) and G_{34} (long and narrow junction), as well as the interlayer conductances G_{13} and G_{14}.

The intralayer conductance G_{12} is the most important channel for quantitative analysis of the conductance. This is the channel that we use for studying the signatures in the conductance that arise from spectral features in the moiré bands. This is due to the large number of modes available in the leads, which are tightly packed in energy within a wide energy range that fully encompasses the width of the quasi-flat bands. This allows our setup to energetically probe extremely fine details in the topology of the moiré band structure. On the other hand, the three other channels are useful to qualitatively assess the coupling of the graphene ribbons. If the layers are weakly coupled, then we expect the intralayer conductance to be approximately equal to that of monolayer graphene. Most electrons will propagate with marginal interlayer scattering,

and therefore largely without contribution from the adjacent graphene sheet. For the same reason, in this weakly-coupled regime we expect the interlayer conductances to be approximately zero. As the coupling is increased, the conductance will deviate from the monolayer value.

In conclusion, the device in Fig. 5.1 is capable of qualitatively assessing the coupling of the graphene sheets, and it can also be used to quantitatively study the effects of spectral features of the moiré bands on the wide-junction conductance G_{12}. However, this setup has two apparent drawbacks. The first is that the spectrum can only be calculated for commensurate twist angles, and therefore we might lose track of critical points when we continuously evolve the twist angle in the conductance simulations. A critical transition, for instance the merging of van Hove singularities in the moiré bands, can happen at a non-commensurate twist angle. The second issue that our device has is that even if we keep the size of the scatterer constant, a change in the twist angle leads to a different moiré pattern. Recall that the conductance is largely determined by the overlap of the electron wave functions between the leads and the scatterer. A different moiré pattern can have scattering wave functions localized in different places of the scatterer. This will influence the conductance, simply by measure of the relative position in which the terminals connect with the scatterer in relation to the moiré pattern. For example, suppose that the coupling of the layers at twist angles θ_1, and θ_2 is the same. However, the moiré pattern of the scatterer at θ_1 is such that AA regions connect directly to the terminals 1 and 2 (recall that the wave functions of twisted bilayer graphene at small twist angles localize in the AA regions). On the contrary, the moiré pattern of the scatterer at θ_2 is such that the scattering wave functions have their minima, at AB regions, near the contacts 1 and 2. Despite the coupling being the same, the conductances could have different values only due to the relative position where we connect the terminals.

Fortunately, these two difficulties in our method can be overcome using a remarkable feature of our tight-binding model: the equivalence of the interlayer coupling induced by the twist angle and the interlayer hopping amplitude for small variations of these parameters. Due to this equivalency, we can bypass the periodicity condition of the twist angle, and continuously evolve the moiré bands using the interlayer hopping amplitude instead. Within a small range of deviations, these two parameters lead to effectively the same changes in the low-energy spectrum of twisted bilayer graphene, even of dispersive bands outside the moiré spectrum. This feature of our model allows us to preserve the physical configuration of the device, not only the size but also the moiré pattern, and to continuously tune the interlayer coupling. We turn now to the discussion of this crucial result.

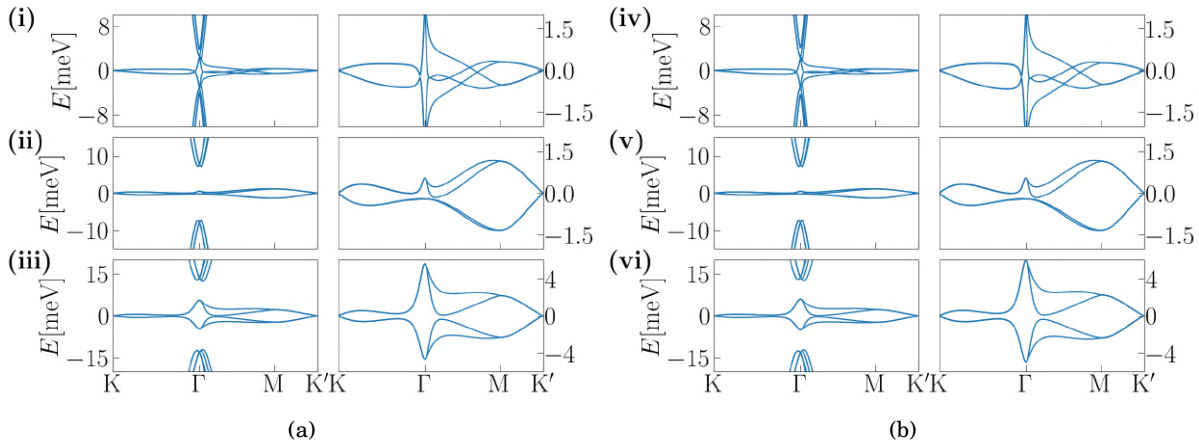

Figure 5.2: Spectrum of near-magic-angle twisted bilayer graphene through high-symmetry points K, Γ, M and K'. (a) Left column. Twist angle variation at constant interlayer hopping amplitude $V^0_{pp\sigma} = 390$ meV: (i) $\theta \approx 1.02°$, (ii) $\theta \approx 1.05°$ and (iii) $\theta \approx 1.08°$. (b) Right column. Interlayer hopping variation at constant twist angle $\theta \approx 1.05°$: (iv) $V^0_{pp\sigma} = 377$ meV, (v) $V^0_{pp\sigma} = 390$ meV and (vi) $V^0_{pp\sigma} = 403$ meV.

5.2 Equivalence between twist angle and interlayer hopping amplitude

Untwisted bilayer graphene, as well as large angle ($\theta \gtrapprox 3°$) twisted bilayer graphene, can be described as weakly coupled systems [20]. Consequently, they exhibit a conductance equal to twice that of monolayer graphene, especially at energies near the Dirac points [4, 55]. On the other hand, small-angle ($0.6° \lessapprox \theta \lessapprox 3°$) twisted bilayer graphene is a strongly coupled system. This coupling is primarily a result of the flattening of the four spin-degenerate moiré bands, which can be deduced from the long-wavelength Dirac continuum theory of this material we discussed in Sec. 2.3.1. In our tight-binding model, the minimum bandwith of the moiré bands is about a dozen meVs, and it occurs at the commensurate twist angle $\theta \approx 1.02°$, which is close to the reported first magic-angle in real samples $\theta_m \approx 1.1°$ [99]. We find that at a twist angle of $\theta \approx 3°$, the bandwidth is still in the eV range, and we have a system of two largely decoupled graphene ribbons. We can infer from these two observations that the flattening of the moiré bands occurs rapidly in the range $\theta \in (1°,\ 3°)$. In addition, in the coupled regime we can interpret the twist angle as an interlayer coupling parameter.

Another important parameter of our tight-binding model is the interlayer hopping amplitude $V^0_{pp\sigma}$ (see Eq. 2.37). This parameter corresponds to the $\sigma-$bonded p_z overlap integrals of sites stacked right on top of each other, and does not change with twisting. Atomic corrugation of the lattice, which we will discuss in the next chapter, also does not modify this parameter, since its effect is encompassed by the exponentially decaying factor in Eq. 2.37. $V^0_{pp\sigma}$ is, by definition,

another interlayer coupling parameter that can be tuned in real samples by applying uniaxial pressure between the layers. Indeed, recent studies on small-angle twisted bilayer graphene have shown that pressure induces an increase in the interlayer coupling and, consequently, the modification of the value of the magic angle [100, 101]. Therefore, both experimental and theoretical considerations suggest that the coupling of the graphene sheets can be tuned through pressure (i.e., through the interlayer hopping amplitude $V^0_{pp\sigma}$ in our model) in a way that induces analogous effects to the tuning of the twist angle.

Remarkably, within the small-angle regime, in our model both of these interlayer coupling parameters can be tuned to induce almost exactly the same distortion of the low-energy band structure [20, 24]. In Fig. 5.2 we can observe that the moiré bands, the bandgap to the nearest dispersive bands, and even the first dispersive bands can be tuned to be indistinguishable to each other with proper tuning of these parameters. Near the magic angle this equivalence holds to a remarkable precision of $\Delta E \approx 10^{-6}$ meV. We note that the Dirac-point energy is slightly shifted (in the order of a few tenths of meVs), and therefore the equivalence is not total, since a shift in energy takes place of the whole band structure. However, this fact is inconsequential for this work, since we are interested in the flat bands themselves, and therefore we always fix the Fermi level, and Dirac-point energy, at $E_F = 0$. The electron density of states, shown in Fig. 5.3, confirms that the quasi-flat bands are effectively the same throughout the moiré Brillouin zone. This equivalence is a powerful tool that allows us to bypass the commensurability condition of Eq. 2.19, which limits our spectral calculations to commensurate twist angles, and instead continuously tune the interlayer hopping amplitude. Moreover, we can utilize commensurate angles to establish the relationship between these two coupling parameters. In addition, it increases the flexibility of our model, because variations in the interlayer hopping amplitude do not affect the geometry of the sample. The "drawbacks" that we discussed in the previous section are removed, improving the consistency of our calculations.

Of course, the equivalence between twist angle and interlayer hopping amplitude must break at some point. We find that within a range of twist-angle deviations of $\delta\theta \approx 0.3°$, which corresponds to $V^0_{pp\sigma} \approx 13\,\text{meV}$, this equivalence still holds, with a maximum difference of just $\Delta E \approx 10^{-6}\text{meV}$. This range of equivalence $(\theta_m - \delta\theta,\ \theta_m + \delta\theta)$ is sufficient for our purposes, since it is wider than state-of-the-art experimental capabilities to produce twisted bilayer graphene samples ($\delta\theta \approx 0.1°$ [102]). Moreover, it is sufficient to connect two nearest commensurate twist angles for twist angles below $\theta = 1.2°$. Therefore, below this threshold we can anchor the twist angle to a commensurate one, continuously tune the interlayer coupling using the interlayer hopping amplitude, and reach the effective coupling of the next commensurate twist angle. Afterwards we repeat the process.

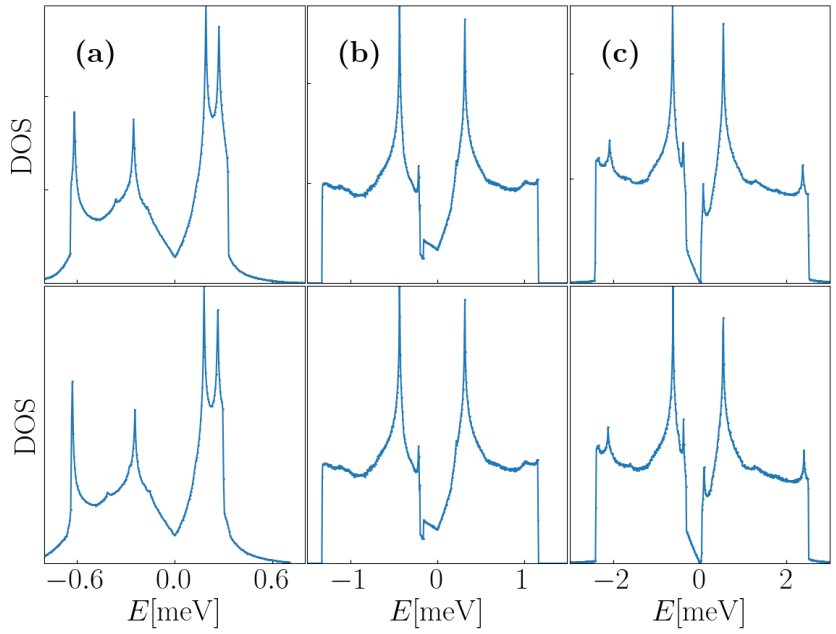

Figure 5.3: Density of states of near-magic-angle twisted bilayer graphene. The top row has varying twist (left to right $\theta \approx 1.02°,\ 1.05°$ and $1.08°$), the bottom row has varying interlayer hopping amplitude ($V^0_{pp\sigma} \approx 377$meV, 390meV and 403meV respectively). Compare with Fig. 5.2: column (a) corresponds to subpanels (i) and (iv), column (b) to subpanels (ii) and (v), and column (c) to subpanels (iii) and (vi).

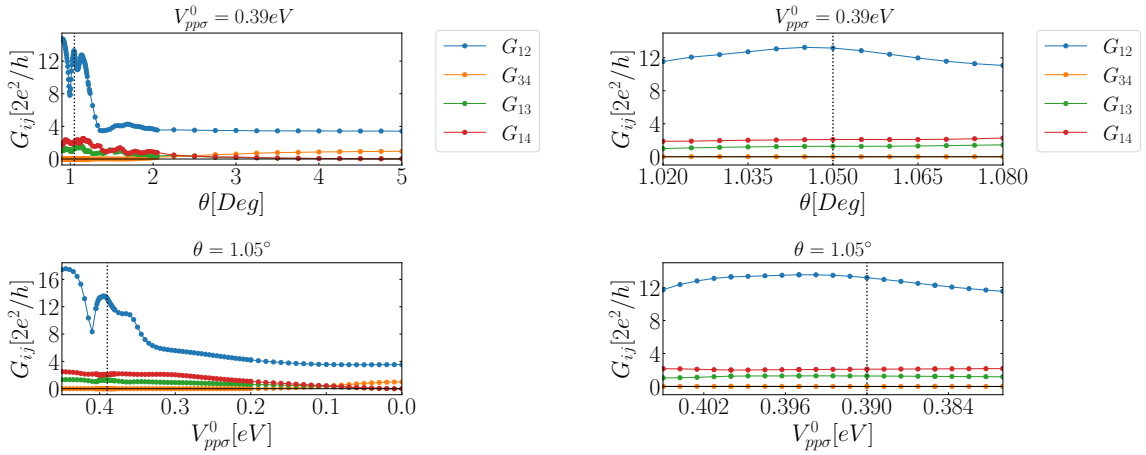

(a) Wide range

(b) Narrow range

Figure 5.4: Four-terminal minimal conductance $G_{ij}(E = 0)$. Upper row: fixed interlayer coupling $V^0_{pp\sigma} = 0.39\,\text{eV}$ and varying twist θ. Bottom row: fixed twist angle $\theta = 1.05°$ and varying interlayer hopping amplitude $V^0_{pp\sigma}$.

5.3 Minimal conductance

Having established the setup and the method of analysis, we now calculate the conductance G_{ij} at the Dirac-point energy $E_F = 0$, which we dub the *minimal conductance* of the system in congruence with previous quantum transport studies on graphene systems [4, 6, 55]. We show these results in Fig. 5.4. We examine the minimal conductance both as a function of the twist angle (upper row) and the interlayer hopping amplitude (bottom row). At large angles ($\theta \gtrsim 3°$) the conductance shows a universal behavior independent of the twist angle. The short-junction conductance G_{12} approaches a value corresponding to the minimal conductivity of monolayer graphene, namely $G_{12}\, W_{\text{bottom}}/W_{\text{top}} \approx 4e^2/\pi h$, which is in agreement with the literature. On the other hand, the long-junction conductance G_{34} converges to the quantized value of $2e^2/h$, indicating a lack of interference with the second graphene layer. Finally, the interlayer conductances G_{13} and G_{14} vanish, since electrons do not propagate between the layers.

These results are fully consistent with our interpretation of large-angle twisted bilayer graphene as a weakly coupled system. The large-angle conductance is the same as the conductance of two completely decoupled graphene sheets with $V^0_{pp\sigma} = 0$. The long-junction conductance corresponds to a single spin-degenerate, propagating bulk mode confined to the bottom layer, whose presence is attributed to the width of the nanoribbon [103]. The interlayer channels effectively have zero-conductance, because there is no scattering crossover between electrons in different layers. Thus, the two nanoribbons are effectively decoupled, and the conductance tensor decomposes into two independent two-terminal conductances. This is fully in agreement with previous studies [88].

For small angles ($\theta \lesssim 3°$) the interlayer conductances are non-zero, clearly indicating scattering crossover between the two nanoribbons. This is also reflected in the decay of the long-junction conductance G_{34}, since the propagating bulk mode in the bottom sheet can now interfere with the corresponding mode in the top layer. Near the first magic angle $1.02° \lesssim \theta \lesssim 1.08°$ G_{34} is practically equal to zero. On the contrary, the wide-junction conductance G_{12} is sharply enhanced in the small-angle regime, and as we approach the magic angle $\theta \approx 1.05°$ G_{12} has a value considerably larger than that in the large-angle regime (about three times larger).

The behavior of the different conductance channels is primarily a consequence of the formation of quasi-flat energy bands in small-angle twisted bilayer graphene. The density of states around $E_F = 0$ is strongly enhanced by the formation of the flat bands, while the Fermi velocities of the corresponding bulk modes are decreased. A sufficiently large number of modes is required to capture the conductance enhancement, which is why the wide-junction conductance G_{12} shows the largest effect. This reinforces our view, that G_{12} is the most appropriate quantity to study how the properties of the moiré bands affect the transport properties of this device.

Note that the equivalence between twist angle and interlayer hopping amplitude is largely preserved in these conductance calculations. Within our deviation target of $\delta\theta \lessapprox 0.3°$ in twist angle, or $V^0_{pp\sigma} \lessapprox 13\,\text{meV}$ in interlayer hopping amplitude, we observe a very similar conductance

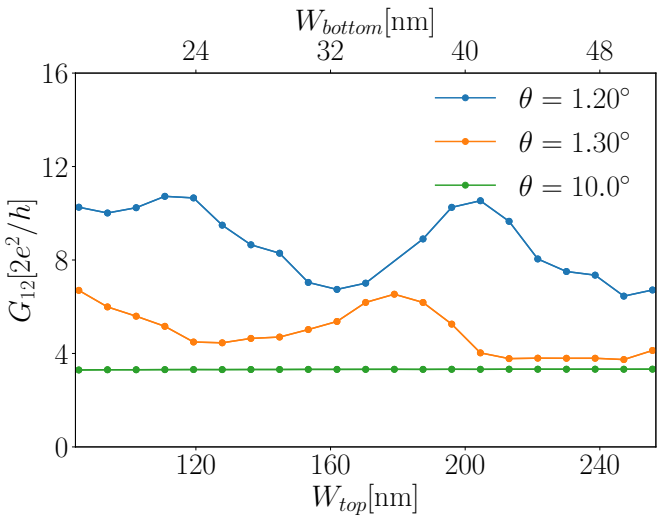

Figure 5.5: Wide-junction minimal conductance $G_{12}(E = 0)$ as a function of system size with fixed aspect ratio $W_{\text{top}}/W_{\text{bottom}} = 5$.

curve (compare upper and lower subpanels in column (b) of Fig. 5.4). However, unlike the moiré spectrum, the conductance is not exactly the same. Nonetheless, the difference is small, and does not affect the overall results of the calculations. This is further confirmation that we can use the interlayer hopping amplitude instead of the twist angle to tune the coupling of the layers continuously, both for spectral and conductance calculations.

In Fig. 5.5 we compare the minimal conductance in the small and large twist angle regimes as a function of the system size, maintaining a fixed aspect ratio. For large angles (we use $\theta = 10°$ as a representative case), the minimal conductance is the same universal monolayer graphene value, regardless of system size, consistent with our previous considerations. On the contrary, in the small-angle regime the conductance shows pronounced oscillations as a function of the system size. Notably, the period of these oscillations does not correspond to the size of the moiré unit cells. Also noteworthy is that for all system sizes considered the minimal conductance in the small-angle regime is significantly larger than the universal value of monolayer graphene, indicating that both layers contribute to electronic transport. This result is not trivial, since we expect moiré physics to emerge only if the system size has at least a few moiré unit cells, but in these results the smaller systems considered contain approximately a single moiré unit cell in their narrow dimension W_{bottom}. Unsurprisingly, the conductance is larger at the twist angle $\theta = 1.20°$ than at $\theta = 1.30°$, consistent with the expected flatter moiré bands at the larger angle. These results clearly indicate that variations in the size of the device can have significant effects, and should be carefully considered. For this reason, it is important to maintain constant as many variables as possible for proper comparison of the conductances at different twist angles. In particular, the size of the device and the moiré pattern should be constant.

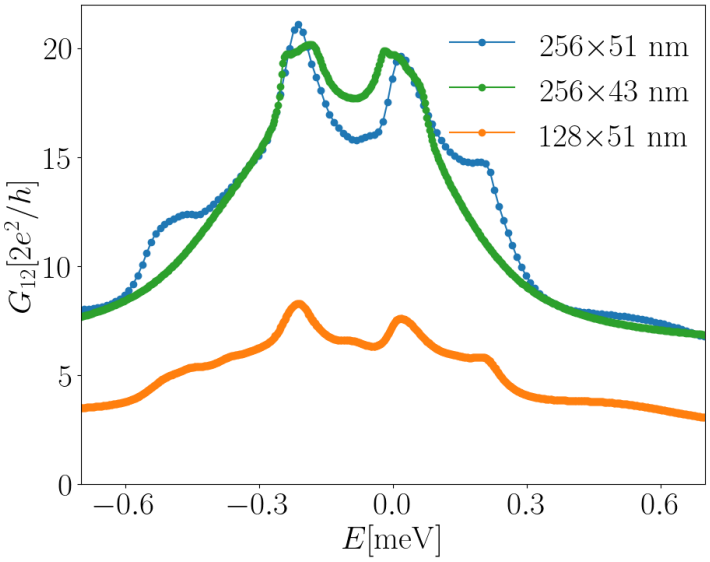

Figure 5.6: Wide-junction conductance $G_{12}(E)$ of three representative device sizes. 256×51nm corresponds to the size of the devices used throughout this work. 256×43nm represents a slight decrease of the long-junction width W_{bottom}. 128×51nm is a significant decrease of the wide-junction width W_{top}.

5.4 Quantum transport signatures of moiré bands

In this section, we relate the low-energy conductance $G_{ij}(E)$ of the twisted bilayer graphene device described above to the bulk spectrum of small-angle twisted bilayer graphene. We begin with a brief discussion of finite-size effects on these conductance simulations. Next, to facilitate our analysis we distinguish three separate regimes within the small-angle limit, and we discuss the signatures of van Hove singularities and other spectral features. To better relate the signatures in the conductance to the dispersion of the energy bands, we also study the evolution of the Fermi surface at energies close to these signatures. We note that with decreasing twist angle $\theta \lessapprox 1.05°$, additional energy band crossings lead to a plethora of spectral features in the moiré Brillouin zone. Some of these features have diverging density of states, but they are confined to such small regions of the moiré Brillouin zone, that they do not show a conductance signal in our device. We believe that with a much larger sample these features would show in the conductance. Since we cannot account for the effects of all spectral features on the conductance, in the following we restrict our discussion to only *significant* features in the computed density of states, defined not only by a diverging density of states but for the spread and height of the corresponding peak in the density of states plot. We also note that we checked that all significant peaks correspond to van Hove singularities with a logarithmic divergence, indicating that they are ordinary (see Sec. 2.3.2 regarding the order of van Hove singularities).

5.4.1 Finite-size effects

We need to quantify the effect that our choice of aspect ratio (about $1:5$ top width W_{top} to bottom width W_{bottom}) has on the conductance. The leads connected to the wide junction in our device contain tens of thousands of modes, tightly packed within the energy range of the quasi-flat bands. Fig. 5.6 shows the energy-resolved wide-junction conductance $G_{12}(E)$ of three samples of different sizes and with the same twist angle $\theta \approx 1.05°$. The reference curve is shown in blue, and corresponds to the chosen size of our device. We find that reducing the width W_{top}, which corresponds to the orange curve, suppresses the conductance overall, which is due to the reduced number of modes in the top and bottom leads. All of the conductance features are still visible, and there is no discernible effect on their energy position or spread. On the other hand, changing the long-junction width W_{bottom} affects both the broadening and the energetic position of the peaks, but has little effect on the overall conductance signal. Further decreasing W_{bottom} causes features to be washed out, and the signatures are erased from the conductance. Thus, we see two consequential finite-size effects in our device: the energetic shift and the broadening (to the point of complete washout) of features in the conductance. As we mentioned previously, some features in the spectrum are present in such tiny regions of the moiré Brillouin zone, that we were not able to capture their effects on the conductance.

5.4.2 Twist angles $1.12° \lessapprox \theta$

Let us first consider the conductance in the vicinity of the first pronounced maximum of the minimal conductance $G_{12}(E = 0)$, which occurs at the twist angle $\theta \approx 1.14°$ (see the upper row, left column of Fig. 5.4). Fig. 5.7 shows the conductance, the bulk density of states and the moiré bands at the nearest commensurate angle $\theta \approx 1.12°$. In agreement with the literature, the density of states goes to zero at the Dirac point energy, mirroring the case of monolayer graphene. Note that the shape of the moiré bands is quite similar to the four bands in untwisted bilayer graphene, but much flatter (about two orders of magnitude flatter). The conductance G_{12} at the Dirac-point energy $E = 0$ is large and significantly higher than that of monolayer graphene. This is another indication that the layers are strongly coupled in this regime, as we discussed above, so that the Dirac points of both layers now contribute to the conductance. Another reason for the enhancement is the proximity (in energy) of the Dirac-point energy to the two most significant peaks in the density of states: as the bands become flatter, the peaks in the density of states (which correspond to van Hove singularities, as we will soon discuss) approach zero energy. And, due to the broadening of conductance features, at low twist angles there is significant overlap of the signatures from both peaks near the Fermi level.

Near the Dirac point energy, we observe two pronounced peaks (highlighted with dotted red lines) in the wide-junction conductance G_{12}, which align with the two main peaks of the bulk density of states. These peaks are signatures of van Hove singularities in the moiré energy bands. The first indication of this is the diverging bulk density of states, shown in the middle panel in

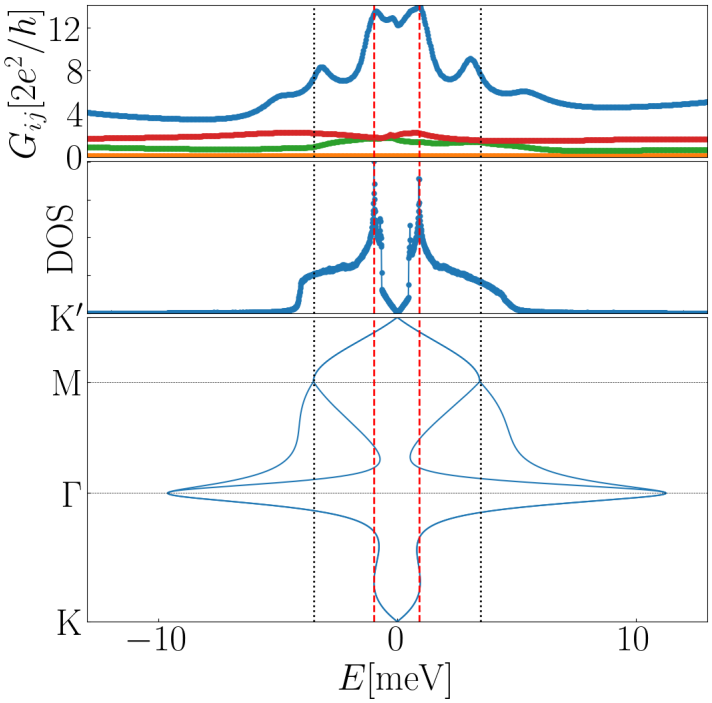

Figure 5.7: Low energy conductance (top), bulk density of states (middle) and moiré energy bands (bottom) of twisted bilayer graphene, at twist angle $\theta \approx 1.12°$ and interlayer hopping amplitude $V^0_{pp\sigma} = 390$meV.

Fig. 5.7. More directly, in Fig. 5.8 we can observe the *double saddle points* in the Fermi surface of the corresponding energies of the density of states peaks (we highlight the double saddle points with a red box). These double saddle points correspond to crossings of two energy bands along the $\Gamma \rightarrow K$ lines of the moiré Brillouin zone. At these crossings, the topology of the Fermi surface changes, constituting a *Lifshitz transition* leading to measurable transport signatures. G_{12} near these singular points is strongly enhanced, with a value about three times larger than outside the moiré bands.

Besides the two main peaks in the conductance we observe two more satellite peaks, with a signature about half as pronounced as the main ones. Notably, these signatures do not align with any van Hove singularity, which is indicated by the absence of divergence in the density of states. However, we have identified non-singular band crossings at the M points of the moiré Brillouin zone, which align closely to the satellite peaks in the conductance (indicated with black dotted lines in Fig. 5.7). We also show the evolution of the Fermi surfaces of these non-singular crossings in Fig. 5.9. These band crossings are also Lifshitz transitions, and appear to have a measurable effect on the conductance despite the fact that they make no contribution to the bulk density of states.

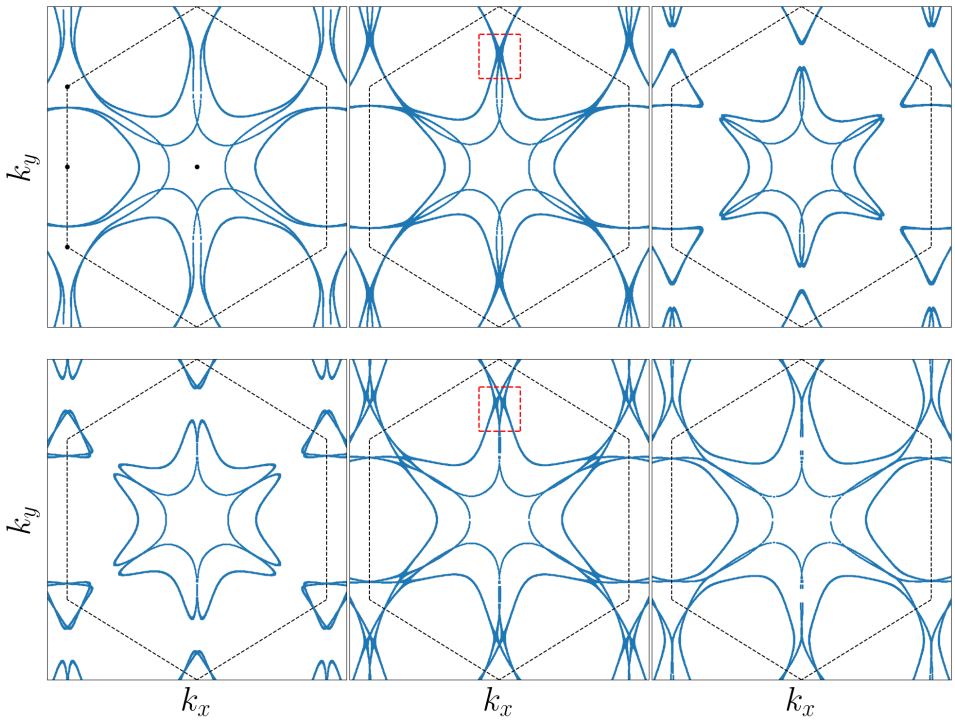

Figure 5.8: Evolution of Fermi surfaces around the van Hove singularities marked by the red dotted lines in Fig. 5.7. From left to right, the panels correspond to the energies slightly below, at, and slightly above a van Hove singularity. The top row corresponds to the singularity in the hole band and the bottom row to the one in the electron band. The red dotted boxes highlight the van Hove singularity.

5.4.3 Twist angles $1.05^\circ \lessapprox \theta \lessapprox 1.12^\circ$

As we decrease the twist angle from $\theta \approx 1.12^\circ$ down to the first magic angle $\theta \approx 1.05^\circ$, the moiré bands are further flattened by about an order of magnitude. This leads to a significant enhancement of the density of states near the Dirac-point energy and consequently to a higher wide-junction conductance $G_{12}(E)$. The conductance, bulk density of states and moiré bands at $\theta \approx 1.05^\circ$ are shown in Fig. 5.10. Remarkably, the conductance at its highest point is now about six times its value outside the quasi-flat bands. As in the previous case, we observe two pronounced peaks that align with two van Hove singularities (highlighted with red dotted lines). These singularities are the same double saddle points that we noted before, which can be observed by continuously tuning the Fermi surfaces using the interlayer hopping amplitude (in the supplementary material of our published work [20], we have included an animation showing the continuous evolution of the bands in the range $\theta \in (1.02^\circ, 1.08^\circ)$).

There are two significant differences between this case and the previous one. The first is the large electron-hole energy asymmetry, and the second is the non-zero bulk density of states at the Dirac-point energy $E = 0$. Unlike the continuous model described in Sec. 2.3.1, the tight-binding

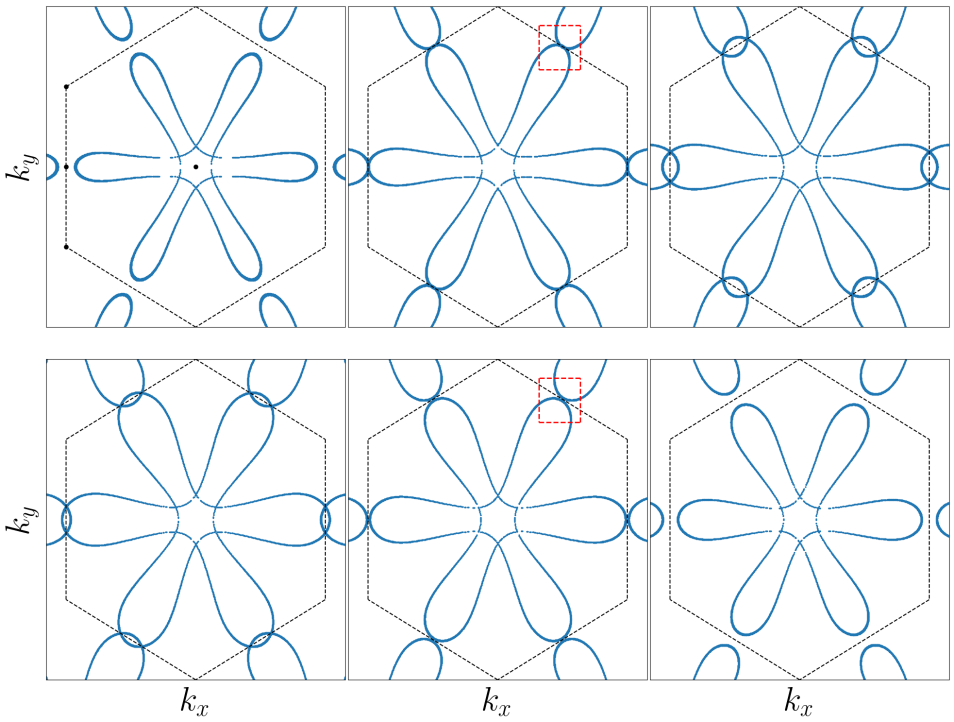

Figure 5.9: Evolution of Fermi surfaces around non-singular crossings of bands marked by the black dotted lines in Fig. 5.7. From left to right, the panels correspond to the energies slightly below, at, and slightly above the crossing points. The top row corresponds to the crossing in the hole band and the bottom row to the one in the electron band. The red dotted boxes highlight the crossings located at the M points.

model of twisted bilayer graphene does not have a strict electron-hole energy symmetry $H \to -H$. However, for angles $\theta \gtrapprox 1.06°$ there is an effective electron-hole symmetry that is rapidly broken near the first magic angle. At this angle, an electron band crosses the zero-energy value and contributes to the bulk density of states. Another interesting difference is the presence of a sharp kink in the density of states slightly to the left of the Dirac-point energy, midway between the Dirac-point energy and the left major peak in the density of states. This kink corresponds to a merging of two van Hove singularities in the bands, which were present in the previous case, but were very close to the two other more significant singularities, so that their effect in the bulk density of states was concealed. At $\theta \approx 1.05°$ these new singularities occupy such a tiny region of the Brillouin zone, that they barely show up in the density of states, and therefore have no corresponding conductance signature. However, these singularities become significant at even lower twist angles.

The Fermi surfaces near the two significant van Hove singularities, those marked with red dotted lines, are shown in Fig. 5.11. The Fermi surfaces of these two singularities remain very similar, despite the breaking of the effective electron-hole symmetry of the moiré bands. On the contrary, the Fermi surfaces of the two additional non-singular band crossings we discussed

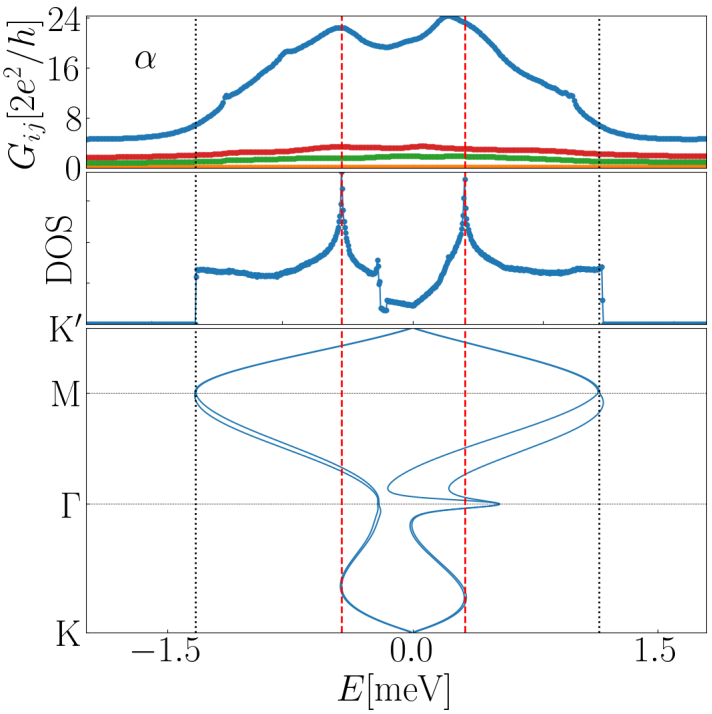

Figure 5.10: Low energy conductance (top), bulk density of states (middle) and moiré energy bands (bottom) of twisted bilayer graphene, at twist angle $\theta \approx 1.05°$ and interlayer hopping amplitude $V^0_{pp\sigma} = 390$meV.

earlier, which we show in Fig. 5.12, are now significantly different. Nonetheless they are of the same kind: a tangential touching at the M point of two oval-shaped surfaces which then collapse to the left of the hole bands (note the absence of Fermi surfaces in the upper left sub-panel) and to the right of the electron bands (lower right sub-panel).

5.4.4 Twist angles $1.02° \lessapprox \theta \lessapprox 1.05°$

Below the first magic angle $\theta_m \approx 1.05°$, twisted bilayer graphene exhibits a remarkably rich variety of spectral features. We noted earlier that the effective electron-hole symmetry of the tight-binding model of twisted bilayer graphene is broken near θ_m. As we lower the angle further, the differences become quite significant. In Fig. 5.16 we show the conductance, bulk density of states and moiré bands at the twist angle $\theta \approx 1.02°$. The first notable difference is the presence of $four$ significant peaks in the density of states, instead of two. Another important difference is the inversion of the bands, i.e. the crossing of electron and hole bands, and the vanishing of the bandgap due to the first dispersive bands connecting with the moiré bands near the Γ point. Finally, a surprising result is the significant misalignment between the peaks in the conductance and the bulk density of states. In this case, some peaks in the density of states have no discernible effect on the conductance, and some peaks in the conductance are not aligned with any significant

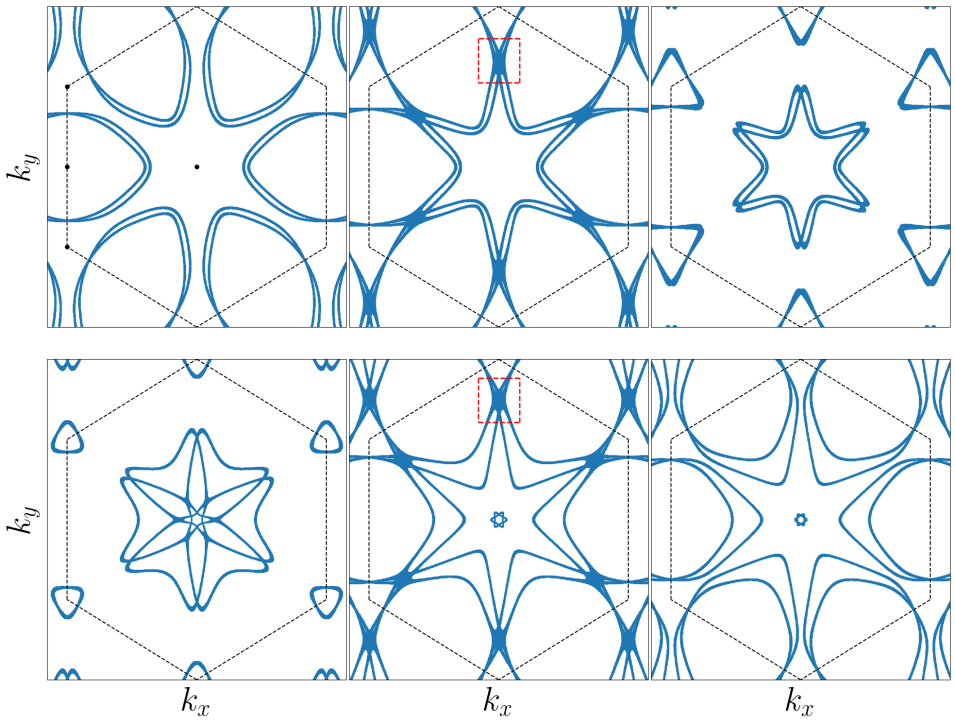

Figure 5.11: Evolution of Fermi surfaces around the van Hove singularities marked by the red dotted lines in Fig. 5.10. From left to right, the panels correspond to the energies slightly below, at, and slightly above a van Hove singularity. The top row corresponds to the singularity in the hole band and the bottom row to the one in the electron band. The red dotted boxes highlight the van Hove singularity.

feature in the bands.

If we tune the interlayer hopping amplitude continuously from an effective twist angle of $\theta \approx 1.08°$ to $\theta \approx 1.02°$, we can follow the evolution of the significant peaks in the density of states. We can see the screenshots at the twist angles $\theta = 1.02°$, $1.05°$ and $1.08°$ in Fig. 5.3. At the twist angle $\theta \approx 1.08°$ we observe only two significant peaks. Note, however, the valley near the Fermi energy. At the edges of this valley we observe two small peaks corresponding to van Hove singularities, but these are confined to such small regions of the moiré Brillouin zone that they do not contribute significantly to the density of states. As we decrease the angle, the van Hove singularity at the right edge of the valley moves to the left, and the left edge to the right. Near the magic angle θ_m, both singularities converge to the same energy point, which is why the valley disappears in the middle panels of Fig. 5.3, leaving only a small kink. Lowering the angle further, these singularities continue to move left and right until they merge with the two other van Hove singularities, which have significant peaks in the density of states. After the merging point, they continue to move left and right as before, but now they have about the same peak and width as the other two van Hove singularities, so that we have four significant peaks instead of two. Below the merging point, for example at the twist angle $\theta \approx 1.02°$, the two peaks to the extreme

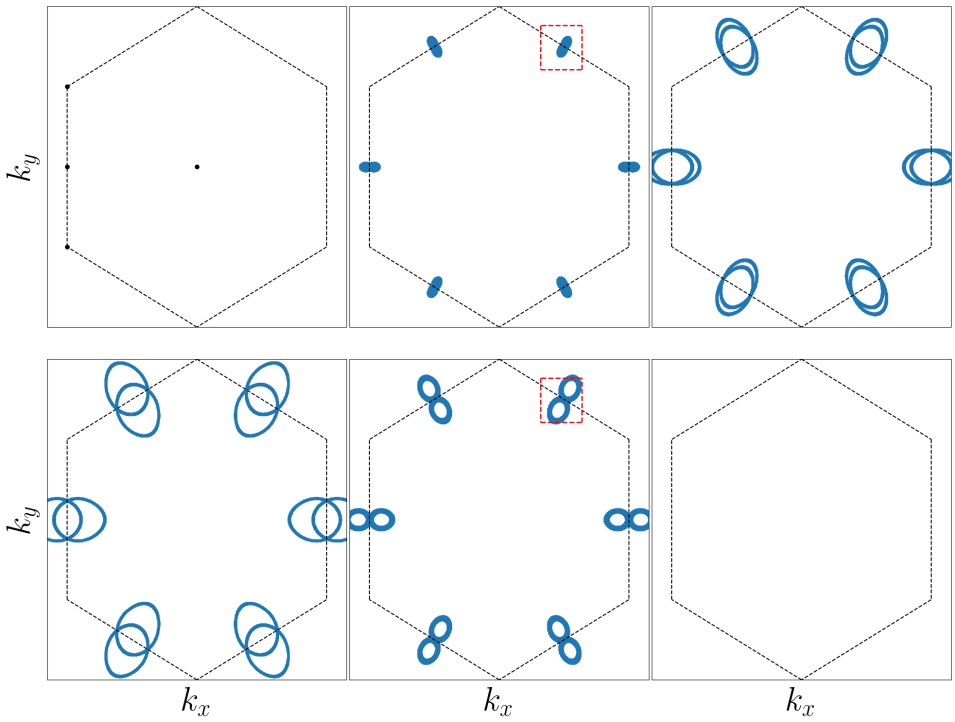

Figure 5.12: Evolution of Fermi surfaces around non-singular crossings of bands marked by the black dotted lines in Fig. 5.10. From left to right, the panels correspond to the energies slightly below, at, and slightly above the crossing points. The top row corresponds to the crossing in the hole band and the bottom row to the one in the electron band. The red dotted boxes highlight the crossings located at the M points.

left and right correspond to the two singularities that were not significant at angles above the merging point. Lowering the angle causes these two singularities to drift further to the left and right, respectively, increasing the energy width of the density of states. The singularity in the hole bands drifts faster, as a function of the effective twist angle, to the left, which is why at $\theta \approx 1.02^\circ$ we see the density of states spread more widely in the hole bands.

At twist angles below the merging point, the density of states is highly energy asymmetric (see the density of states at $\theta \approx 1.02^\circ$ in Fig. 5.16). We recall that at twist angles $\theta \geq \theta_m$ the density of states is not exactly electron-hole symmetric, which can be noticed at twist angle $\theta \approx 1.08^\circ$ because the small valley in the middle of the two significant peaks is slightly to the left of the Fermi energy (see the right panels in Fig. 5.3). However, this asymmetry is small, and consequently both the density of states and the wide-junction conductance are largely the same in the hole and electron bands. This is especially true near the magic angle θ_m. However, after the merging of two pairs of van Hove singularities, the peaks in the hole and electron bands are not equally spaced in energy. Thus, the density of states at twist angles below θ_m is more spread out in the hole band than in the electron band. This asymmetry of the bulk density of states below the first magic angle is of significant importance, and we will return to this effect when we

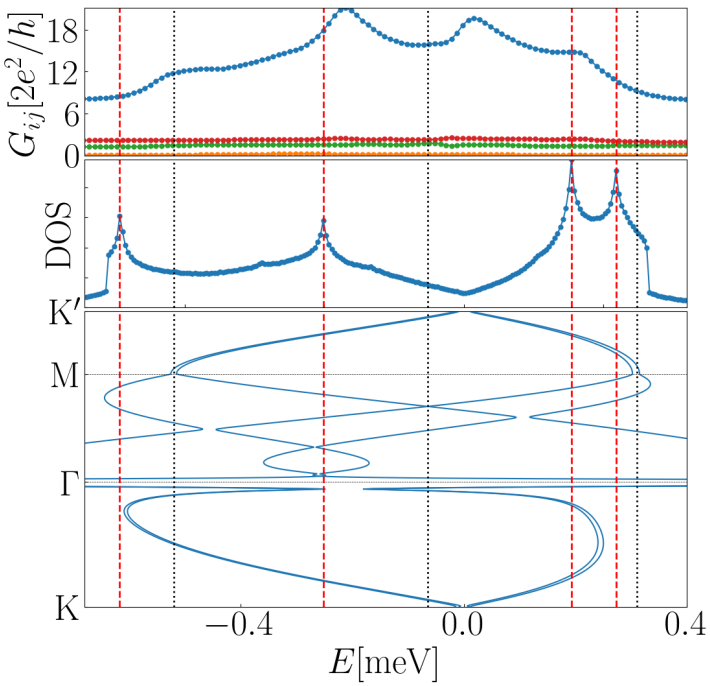

Figure 5.13: Low energy conductance (top), bulk density of states (middle) and moiré energy bands (bottom) of twisted bilayer graphene, at twist angle $\theta \approx 1.02°$ and interlayer hopping amplitude $V^0_{pp\sigma} = 390$meV.

discuss twist angle disorder in the next chapter.

The evolution of the Fermi surfaces near all four van Hove singularities, all marked with red dotted lines in Fig. 5.16, is shown in Fig. 5.14. The order of these from left to right in the conductance plot corresponds to top to bottom in the Fermi surface sub-panels. Note that the first and fourth singularities and the second and third singularities are of the same type, although they have different effects on the bulk density of states. The reason for the different peak amplitudes is that the two peaks in the electron bands are closer together and thus overlap more.

We also show the non-singular band crossings, marked with black dotted lines, in Fig. 5.15. Note that two of these crossings are near peaks in the conductance. Moreover, this time we find a band crossing that is not located at the M point in the Moiré Brillouin zone (second black dotted line from the left in Fig. 5.13, middle row in Fig. 5.15). However, this band crossing remains in the high-symmetry line ΓM.

The misalignment of the conductance and bulk density of states peaks is significant and poses a challenge to the interpretation of our results. Why was the relationship between divergent density of states and conductance peaks so clear at the twist angle $\theta \approx 1.05°$, but not so clear at $\theta \approx 1.02°$? One obvious possibility is that the size of the moiré unit cell at $\theta \approx 1.02°$ is too large for the device we are using. However, this has a simple solution, which is to keep the twist angle at $\theta \approx 1.05°$ and use the interlayer hopping amplitude to increase the coupling of the layers.

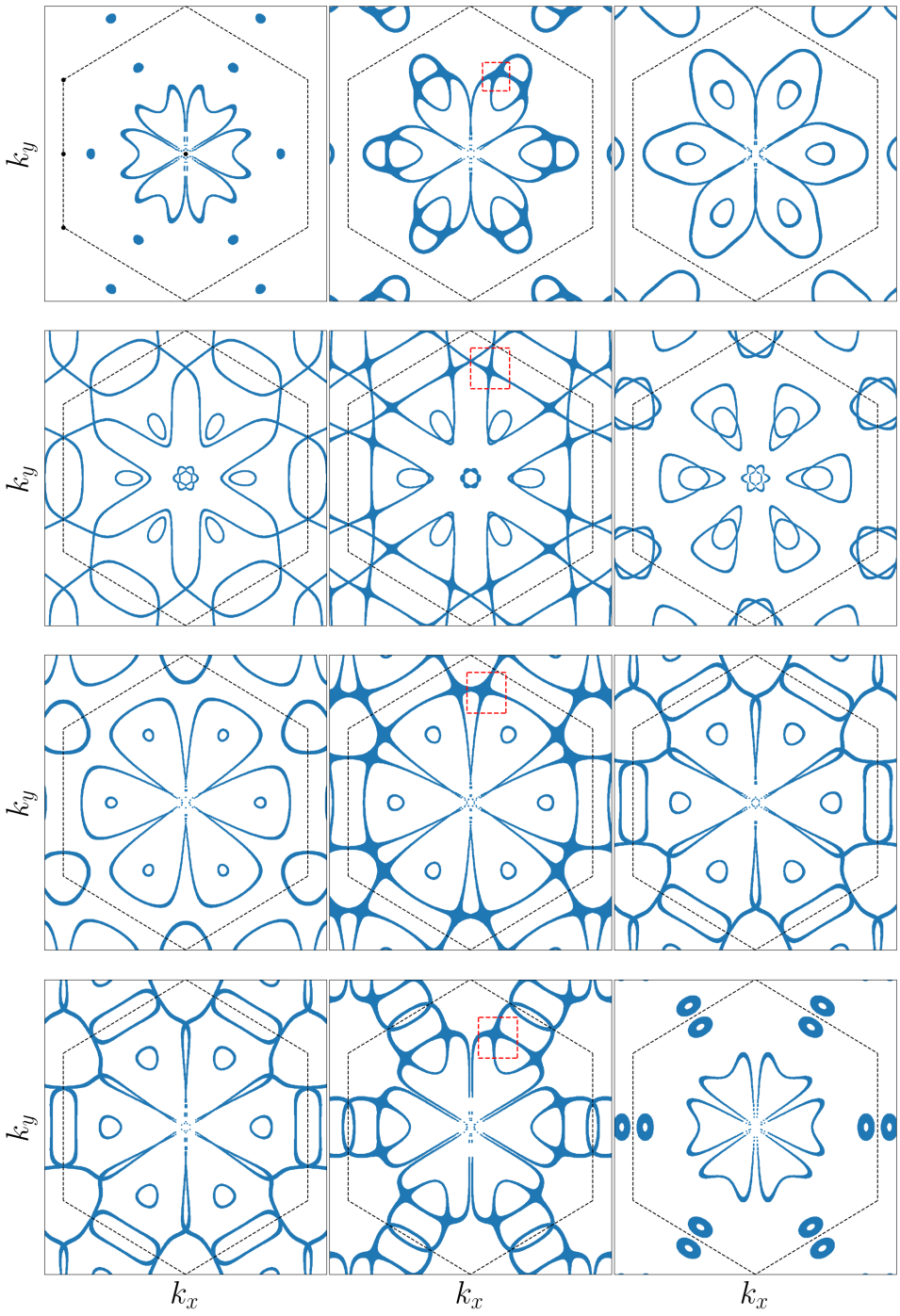

Figure 5.14: Evolution of Fermi surfaces around the van Hove singularities marked by the red dotted lines in Fig. 5.13. From left to right, the panels correspond to the energies slightly below, at, and slightly above the van Hove singularity. The four singularities marked in Fig. 5.13 correspond left to right to the Fermi surfaces top to bottom. The red dotted boxes highlight the van Hove singularity.

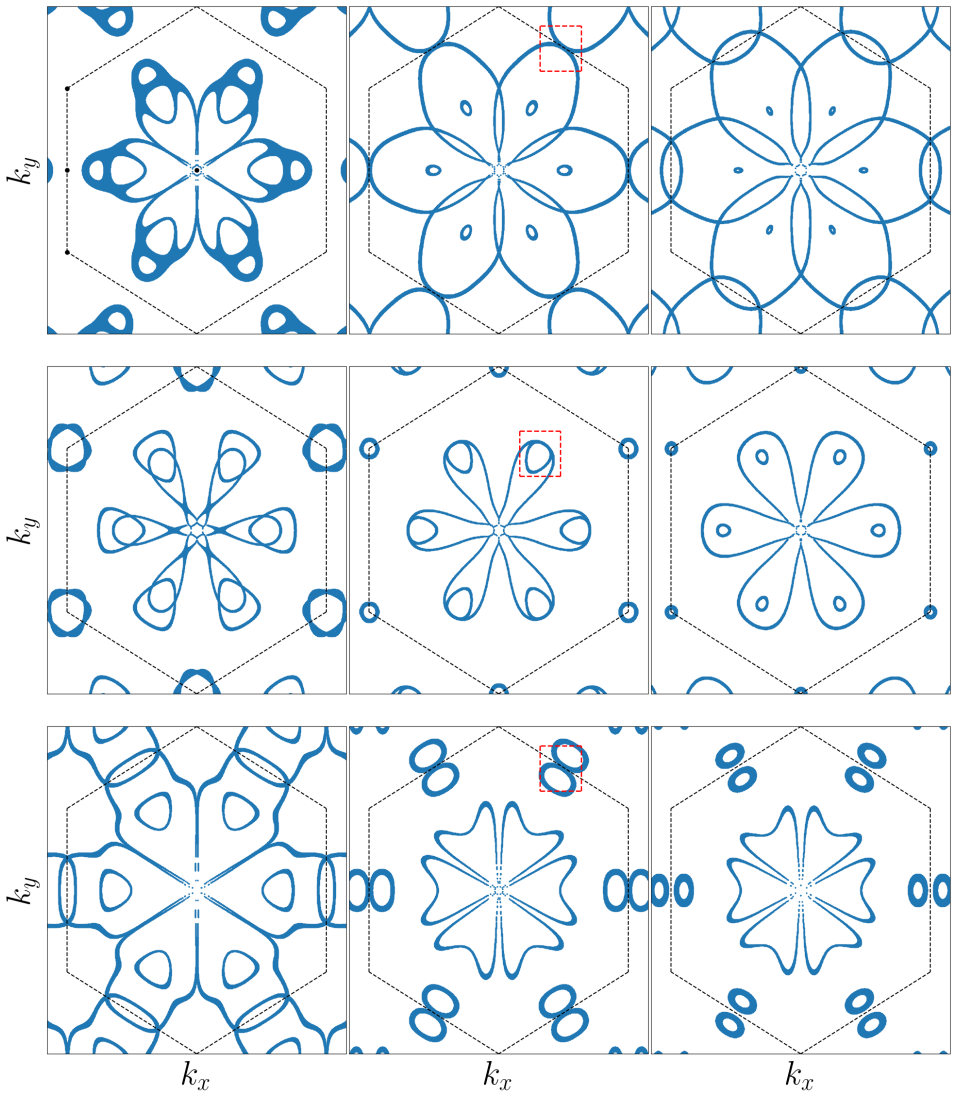

Figure 5.15: Evolution of Fermi surfaces around non-singular crossings of bands marked by the black dotted lines in Fig. 5.13. From left to right, the panels correspond to the energies slightly below, at, and slightly above the crossing points. The three crossings marked in Fig. 5.13 correspond left to right to the Fermi surfaces top to bottom. The red dotted boxes highlight the crossings located in the ΓM line.

In this way, not only the size of the unit cell but also the moiré pattern of the device is kept constant. Fig. 5.16 shows the conductance, bulk density of states, and moiré bands using the twist angle $\theta \approx 1.05°$ and the interlayer hopping amplitude $V^0_{pp\sigma} = 403$meV. We chose this hopping integral because we found that it leads to the same coupling of the layers as using the twist angle $\theta \approx 1.02°$. Note that the bulk density of states and the Moiré bands are essentially the same. Even the Fermi surfaces and non-singular band crossings are indistinguishable, as shown in Figs. 5.17 and 5.18.

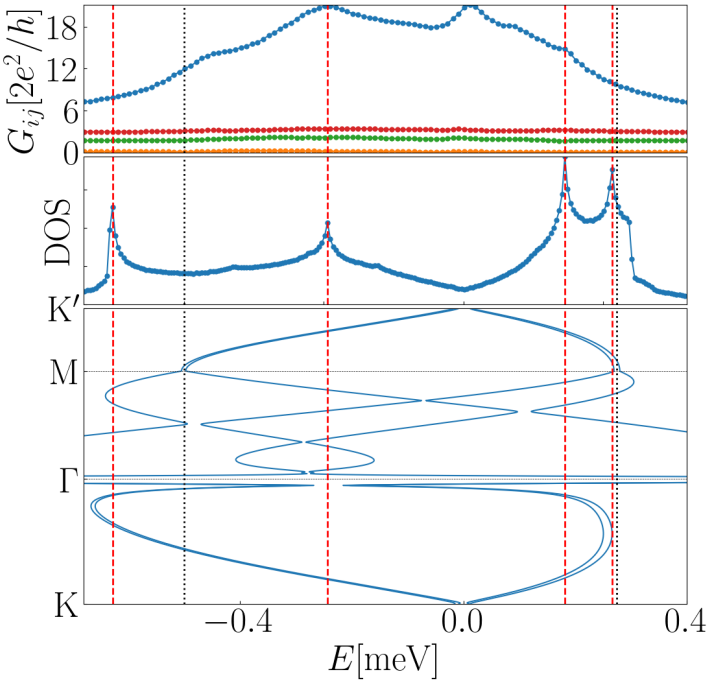

Figure 5.16: Low energy conductance (top), bulk density of states (middle) and moiré energy bands (bottom) of twisted bilayer graphene, at twist angle $\theta \approx 1.05°$ and interlayer hopping amplitude $V^0_{pp\sigma} = 403$meV.

Remarkably, the conductance plot is largely unaffected by these changes: the position of the peaks, the amplitude of the peaks, and all features of the conductance plot are essentially the same. This indicates that the misalignment between the conductance and the density of states is not due to a different moiré pattern. Nonetheless, we believe that the mismatch is due to finite-size effects, but of a non-trivial nature, since the size of the device was clearly sufficient at $\theta \approx 1.05°$, $V^0_{pp\sigma} = 390$meV. The stronger coupling of the layers at an effective twist angle of $\theta \approx 1.02°$ obviously has an influence on the size of the device needed to perform the conductance calculations. Unfortunately, we were not able to simulate a device large enough to overcome these effects.

5.5 Summary

In this chapter we studied the low-energy conductance of twisted bilayer graphene and its relation to the bulk spectrum. We used mesoscopic samples formed crossing a pair of narrow and wide graphene nanoribbons, with metallic leads attached to each graphene sheet. We found that this setup allows us to study the coupling of the layers, both qualitatively and quantitatively, and the relationship between features in the moiré spectrum and the conductance. The results outlined in this section indicate that the low-energy quantum transport of twisted bilayer graphene is

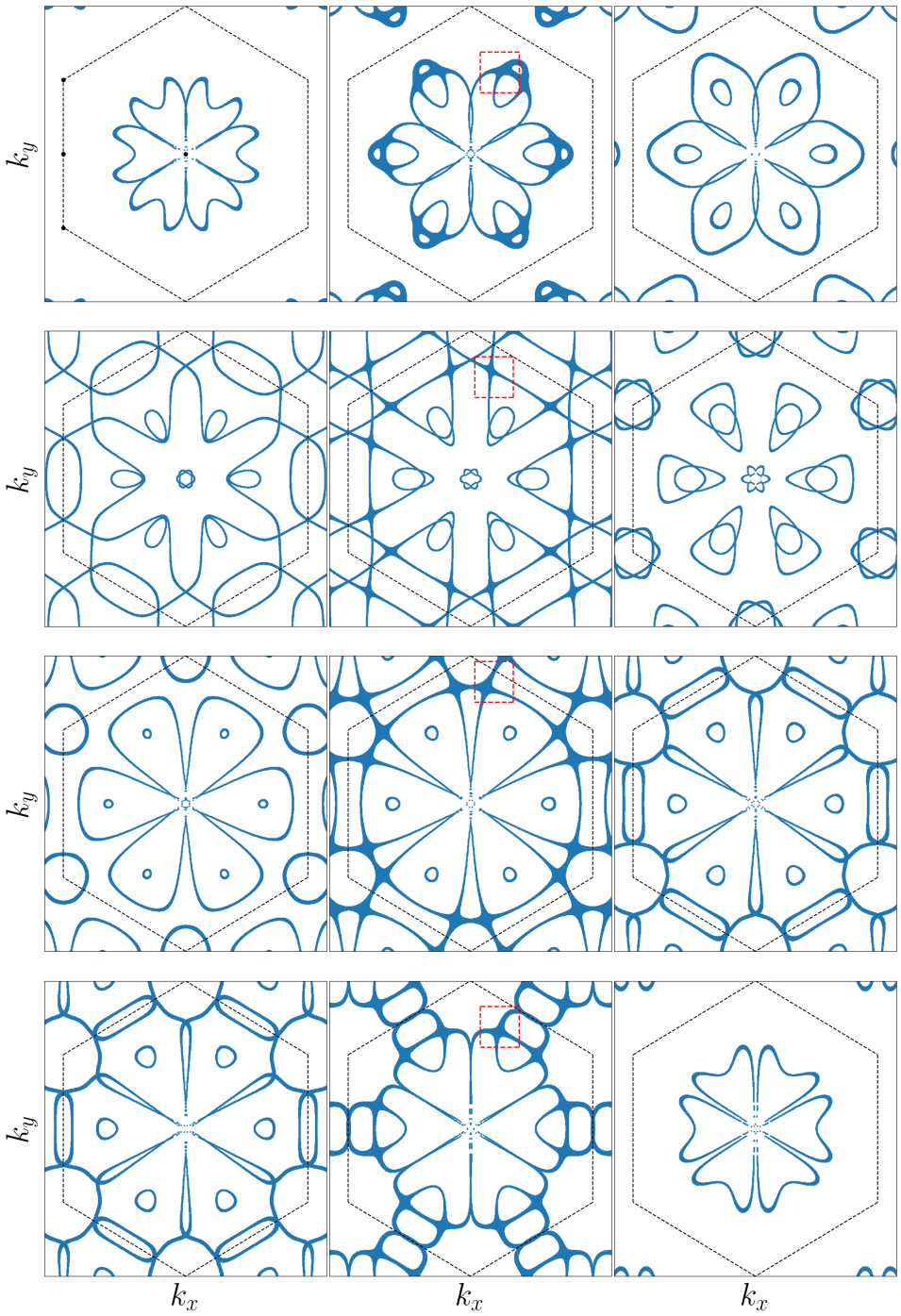

Figure 5.17: Evolution of Fermi surfaces around the van Hove singularities marked by the red dotted lines in Fig. 5.16. From left to right, the panels correspond to the energies slightly below, at, and slightly above the van Hove singularity. The four singularities marked in Fig. 5.16 correspond left to right to the Fermi surfaces top to bottom. The red dotted boxes highlight the van Hove singularity.

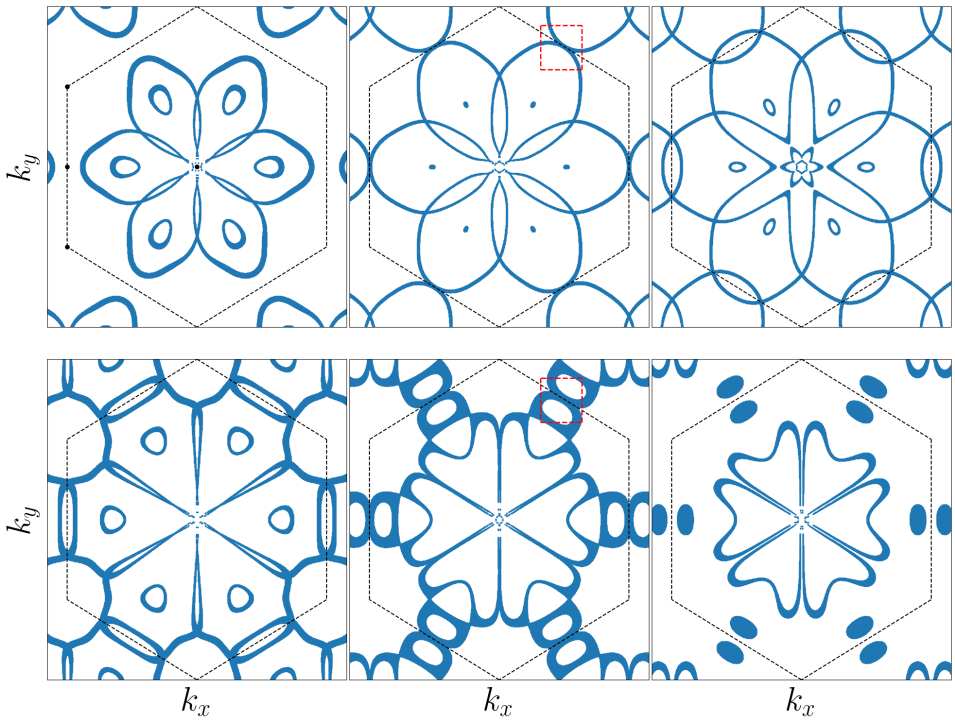

Figure 5.18: Evolution of Fermi surfaces around non-singular crossings of bands marked by the black dotted lines in Fig. 5.16. From left to right, the panels correspond to the energies slightly below, at, and slightly above the crossing points. The two crossings marked in Fig. 5.16 correspond left to right to the Fermi surfaces top to bottom. The red dotted boxes highlight the crossings located at the M points.

influenced by several factors. At large twist angles $\theta \geq 3°$, the layers are effectively decoupled and therefore the interlayer conductance is effectively zero, as incoming electrons are confined to their respective graphene sheets. Conversely, at small twist angles the layers are strongly coupled, and hence there is significant interlayer conductance. Moreover, the wide-junction conductance is strongly enhanced in the small-angle regime. Notably, the coupling of the layers can be fine-tuned with pressure, which in our model is simulated using the interlayer hopping amplitude.

Near-magic-angle twisted bilayer graphene $\theta \approx 1°$ constitutes a remarkably sensitive device with potential applications in high-frequency sensing. We find that the enhanced wide-junction conductance in near-magic-angle twisted bilayer graphene is primarily a consequence of the flattening of the moiré bands, which is in agreement with the literature. This is evidenced by the strong correlation between the bulk density of states and the wide-junction conductance. Furthermore, we have identified a number of van Hove singularities within the quasi-flat bands, which contribute to the conductance through their effects on the bulk density of states. Van Hove singularities play a prominent role in the exotic phenomena of magic angle twisted bilayer graphene by amplifying electronic correlation effects. Our results indicate that these singularities strongly influence the transport properties of the system, but we find that the relationship

between the bulk density of states and the conductance through a finite device is not always straightforward. For twist angles above the first magic angle, a peak in the density of states due to a van Hove singularity coincides precisely with a sharp peak in the conductance curve. However, we found that below the first magic angle, the relationship between density of states peaks and conductance features is not as direct. Peaks in the density of state do not align precisely with peaks in the conductance. In our analysis of finite-size effects in this section, we noted that such behavior happens if the narrow dimension of the sample is not large enough. However, we were not able to perform calculations on a device large enough to overcome these issues at angles below the magic angle. In addition, we identified conductance peaks that do not correspond to any feature of the bulk density of states. These additional conductance peaks seem to coincide with non-singular band crossings located at high symmetry points and lines of the Brillouin zone. Finally, we also observe a broadening of the various conductance features due to finite-size effects. This broadening leads to a strongly enhanced minimum conductance of twisted bilayer graphene near the magic angle, even when the bulk density of states vanishes at the Dirac point.

CHAPTER 6

EFFECTS OF TWIST-ANGLE DISORDER IN MESOSCOPIC TWISTED BILAYER GRAPHENE

In the previous chapter we discussed how remarkably sensitive magic angle twisted bilayer graphene is to variations in twist angle or pressure. The bandwidth of the quasi-flat moiré spectrum changes by several orders of magnitude between the twist angles $\theta = 3°$ and $\theta = 1°$. Indeed, the system evolves from weakly to strongly coupled in just a few degrees of twist. Moreover, the van Hove singularities in the moiré bands, which give rise to sharp nonlinear enhancements of the wide-junction conductance, shift their energetic position dramatically with changes of only a tenth of a degree of twisting. This extreme sensitivity can be exploited to construct a sensitive radio frequency device, but poses a significant challenge to the experimentalist who has a window of less than a tenth of a degree to create a crystal from high-quality graphene flakes. However, this is not the biggest problem facing the experimentalist.

Even if the experimentalist succeeds in producing a single crystal of twisted bilayer graphene with a twist angle pinned down very closely to the first magic angle $\theta_m \approx 1.05°$, the resulting flake subsequently breaks into a landscape of so-called *twist angle domains* [102, 104, 105]. The twist angle in these domains is slightly shifted from the original value, and can have a significant effect on the optoelectronic properties of a sample. This type of disorder is called twist angle disorder. The process of domain formation is due to crystal relaxation processes, and according to the literature it is inevitable and uncontrollable. However, state-of-the-art experimental techniques are capable of reducing the twist angle variation in these domains to as little as $\delta\theta \approx 0.1°$ [102]. This remarkable precision still leaves a large window of variation of the moiré band structure, in particular in regards to its bandwidth and to the energetic position of important spectral features, such as van Hove singularities. It is therefore not surprising that measurements of twisted bilayer graphene samples have a large variance. Typically, experimentalists need to produce

many flakes of twisted bilayer graphene before measurements show promising results. The results outlined in Chapter. 2 show that the location of van Hove singularities and the level of overall flatness of the moiré bands changes significantly between the commensurate angles $\theta \approx 1.02°$, $\theta \approx 1.05°$ and $\theta \approx 1.02°$, and therefore approximate to state-of-the-art experimental capabilities. A comprehensive study of twist angle disorder and its effects on the physical properties of twisted bilayer graphene is therefore necessary to better understand this remarkably sensitive material.

Previous theoretical works on twist angle disorder in twisted bilayer graphene have used a variety of approaches. Among these we note the following: real-space domain models [78, 106], non-uniform moiré patterns with a minimal continuous model [107], transmission calculations though one dimensional variation of twist angle in minimal continuous models [77, 78, 81], and a Landau-Ginzburg theory to study the interplay between electron-electron interactions and disorder [108]. Although these studies contribute to the understanding of twist angle disorder, they are often limited to single twist angle domains, boundaries between two singular domains, or they are long-wavelength theories that can not account for correlations at the moiré scale. A major hurdle for the study of twist angle disorder is that numerical simulations are notoriously difficult to perform due to the implied distortions of the real-space lattice. Most numerical packages for quantum transport, such as the Python package kwant that we use in this work, require that the leads have the same translational symmetry as the crystal in the scattering region. In addition, it is often not clear how to numerically treat the boundaries between twist angle domains.

Fortunately, the equivalence between twist angle and interlayer hopping amplitude that we discovered in the previous chapter provides a powerful tool that allows us to bypass the distortion of the physical lattice. Instead of changing the real-space position of sites, we can instead tune the interlayer hopping amplitude and leave the spacial configuration of the lattice intact. In this way, we alter the coupling of the layers in different domains but we do not have to contend with issues at domain boundaries, or alterations of the translational symmetry of the leads. The results outlined in the previous chapter show that the coupling of the layers is affected equally by tuning the twist angle and the interlayer hopping amplitude, as long as the deviation of the twist angle is within $\delta\theta \lessapprox 0.3°$. This range of equivalence is more than sufficient for our purposes, as it is significantly lower than the state-of-the-art experimental precision of $\delta\theta \approx 0.1°$.

This chapter is organized as follows. We begin in Sec. 6.1 where we describe in detail the model and the type of apparatus we use to study twist angle disorder. We then explain the randomization process we used to generate ensembles of disordered samples. Next, in Sec. 6.2 we show the effects that twist angle disorder has on the conductance. We also compare the effects of twist angle disorder to on-site energy disorder, and find a characteristic feature of twist angle disorder in near-magic angle twisted bilayer graphene, which we suggest could be used for the characterization of disorder in real samples. We continue in Sec. 6.3 and investigate the effects of temperature on the conductance. Although the effects of twist angle disorder are disrupted by temperature, we find that the temperature required to completely destroy the characteristic

signatures of twist angle disorder is higher than the critical temperature of the correlated phases in twisted bilayer graphene. Therefore, we suggest our characterization can be used in realistic samples. We also study the effects of Hartree interactions in Sec. 6.4, and of lattice corrugation in Sec. 6.5. In both cases, we find solid arguments for expecting the effects of twist angle disorder to survive these disruptions in real devices. Finally, we provide a summary of this chapter in Sec. 6.6.

6.1 Model and setup

For the theoretical description of twisted bilayer graphene, we use the same tight binding model that we developed in Sec. 2.3 and exploited in the previous chapter. We are interested in the effects of twist angle disorder near a magic angle. However, we do not in fact induce deformations in the lattice. Instead, we use the equivalency between twist angle and interlayer hopping amplitude that we showed on the previous chapter. We anchor the twist angle at the first magic angle $\theta_m \approx 1.05^\circ$ and induce twist angle disorder through the interlayer hopping amplitude $V^0_{pp\sigma}$. To study this type of disorder we must first generate ensembles of samples with randomized twist angle domains, and then perform conductance calculations over all devices in each ensemble. Therefore, to even greater extent than before, tight binding is the only feasible approach which is capable of scaling up to mesoscopic devices with at least a few tens of magic-angle moiré unit cells. Moreover, we use the same size of the device used in the previous chapter, since we found that it accurately describes both the conductance throughout the moiré bands and the sharp features in the conductance due to van Hove singularities.

We have done preliminary calculations and found that an ensemble of 20 samples is sufficient to obtain a reasonable conductance average with low variance. Thus, for each parameter set, we generate an ensemble of 20 samples with randomized twist angle domains. Furthermore, we are no longer interested in the qualitative evaluation of the coupling of the layers. Therefore, it is not necessary to include the long junction in our calculations. The wide junction G_{01} is the only one which is of interest for us in this chapter, since it gives the quantitative effect of the moiré spectrum on the conductance. Thus, we utilize a simple two-terminal configuration instead of the four-terminal setup we used in the previous chapter.

We begin by describing the process that generates the disordered samples with randomized twist angle domains. There are two main parameters to control for: the number of twist angle domains N_d present in a sample and the disorder strength of the effective twist angle $\delta\theta$. Each ensemble contains only samples with exactly the same number of twist angle domains. The domains are then assigned a randomized effective twist angle using a uniform random distribution in the range $[\theta_m - \delta\theta, \theta_m + \delta\theta]$. We want these domains to have similar shape to the ones found in real grown crystals. Thus, they should have what we can loosely describe as a bubble-like shape. Also, these domains should have smooth boundaries, since lattice relaxation

tends to maximize the line of contact between domains. Finally, we want to avoid adding very small domains, since including them in our calculations would blur the physical meaning of having N_d distinct domains. Therefore, we impose the constraint that each domain should have at least an area of 10% of the domain area average A_s/N_d, where A_s is the total area of the device (approximately equal to 100 magic angle moiré unit cells).

The boundaries of the twist angle domains can be created using the contour lines $g(\mathbf{x}) = C$ of any smooth continuous scalar function g. We find that two-dimensional Gaussian functions defined on the surface of the device are particularly well-suited for this task. Therefore, we will consider the contour lines of the sum of N Gaussian functions defined by the following relation

$$g(\mathbf{x}) = \sum_{i=1}^{N} \frac{1}{\sigma\sqrt{2\pi}} e^{\frac{|\mathbf{x}-\mathbf{x}_i|^2}{2\sigma^2}}, \tag{6.1}$$

where the centers $\mathbf{x}_i$ are random points inside the area of the device, sampled from a uniform random distribution. The number of Gaussians N, the value of the contour line C, and the standard deviation σ of the Gaussians are useful parameters that we can tune to optimize the generation process to resemble real twist angle domains as much as possible. We find that using different standard deviations for each Gaussian leads to inconsistencies and large variance of the twist angle domains' area, so we use the same standard deviation for all functions. A twist angle domain is therefore defined as any region enclosed by a contour line of Eq. 6.1. Domains that are completely inside another domain, *i.e.* holes in the larger domain, are deleted, the hole is filled and the area is added to the larger domain. This is also to make the generated domains similar to those observed in real samples, and to reduce twist angle domain variance within ensembles. Domain boundaries may cross the edges of the sample, and if they do, the contour lines are concatenated to the edge lines. Finally, the remaining region after all generated domains have been removed from the sample is defined as a singular domain, even if it is composed of discontinuous regions. Figure 6.1 shows three examples of randomized samples with $N_d = 3, 5$ and 7 twist angle domains. The "remaining domain" is shown in blue.

To generate the ensembles, we considered the ranges of the parameters $N \in [20, 50]$, $\sigma \in [1.0, 5.0]$, and $C \in [0.01, 0.20]$. In each case, we generated random samples until we had exactly 20 devices with precisely N_d twist angle domains. If a sample has a different N_d than the target, it is simply discarded and the generation process is reinitialized. For most values of N, σ, and C, the generated samples within an ensemble vary enormously, and consequently the area of the twist angle domains within an ensemble has a wide variance. Therefore, we decided to optimize these parameters for each ensemble in regards to the area of the twist angle domains. Thus, we choose the set of parameters N, σ and C that has the smallest standard deviation in area $\sigma_A = \sqrt{\sum_i (A_{\mathrm{d}i} - \bar{A})^2}$, where $A_{\mathrm{d}i}$ is the area of a domain and $\bar{A}$ is the mean of the domain areas in the ensemble. Each ensemble has a distinct set of parameters minimizing σ_A. The optimizing parameters are the following: for $N_d = 3$ we have $N = 23$, $\sigma = 5.0$ and $C = 0.09$; N_d: $N = 26$, $\sigma = 2.0$ and $C = 0.01$; $N_d = 7$: $N = 40$, $\sigma = 2.0$ and $C = 0.05$.

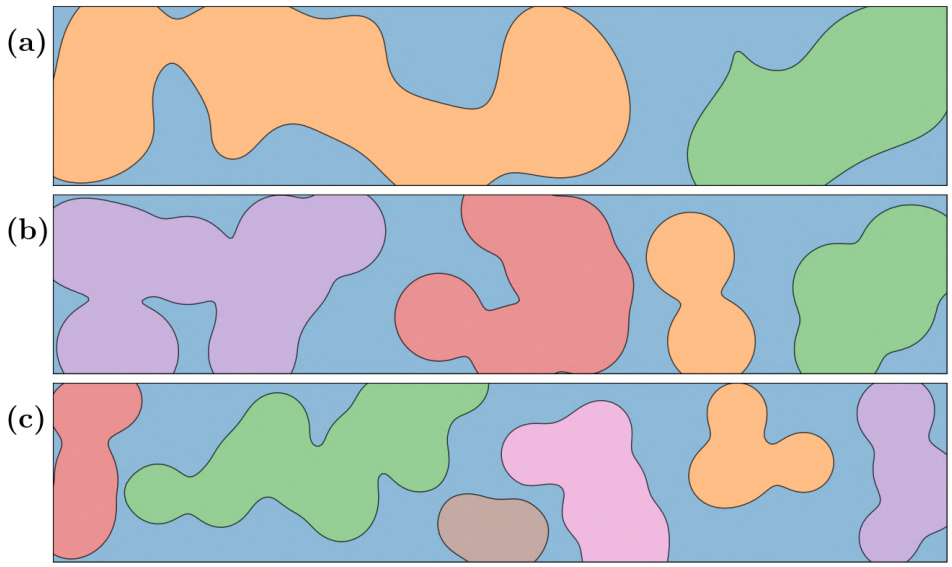

Figure 6.1: Three representative examples of rectangular pristine samples broken into N_d domains with smooth boundaries: (a) $N_d = 3$, (b) $N_d = 5$ and $N_d = 7$. Each color represents a single domain.

Some of the choices we have made for the generation of the disordered ensembles could be seen as arbitrary and therefore disruptive to the randomization procedure. However, we believe that in all cases they are justified by considerations regarding the known shape of twist angle domains in real devices. There is a delicate balance that must be maintained between ensuring that the randomization procedure is not arbitrarily biased, and on the other hand generating the types of structures that correspond to realistic devices. By including small domains, the conductance would be essentially unaffected by twist angle disorder in these tiny regions. In addition, an ensemble with a fixed number of domains could have samples that are very dissimilar. Therefore, we believe that optimizing for ensembles with a fixed number of domains that are comparable in size is the best way to achieve our goal of studying the effects of twist angle disorder on the conductance.

After the process of twist angle domain sample randomization, we proceed to actually induce disorder in each sample and for each ensemble. As mentioned in the introduction, if we tried to displace the actual position of the atomic sites throughout the lattice, we would not be able to attach leads to the system and we would have other difficulties modeling the device. Instead, we induce disorder through the interlayer hopping amplitude, taking advantage of the remarkably useful equivalence between these coupling parameters discussed in the previous chapter. When considering hopping amplitudes between sites in two adjacent twist angle domains, we simply average the values of the interlayer hopping amplitudes in each domain. This clearly has the effect of smoothing the boundaries of the twist angle domains. However, we are not particularly interested in domain boundary effects in this work. Previous research indicates that transmission

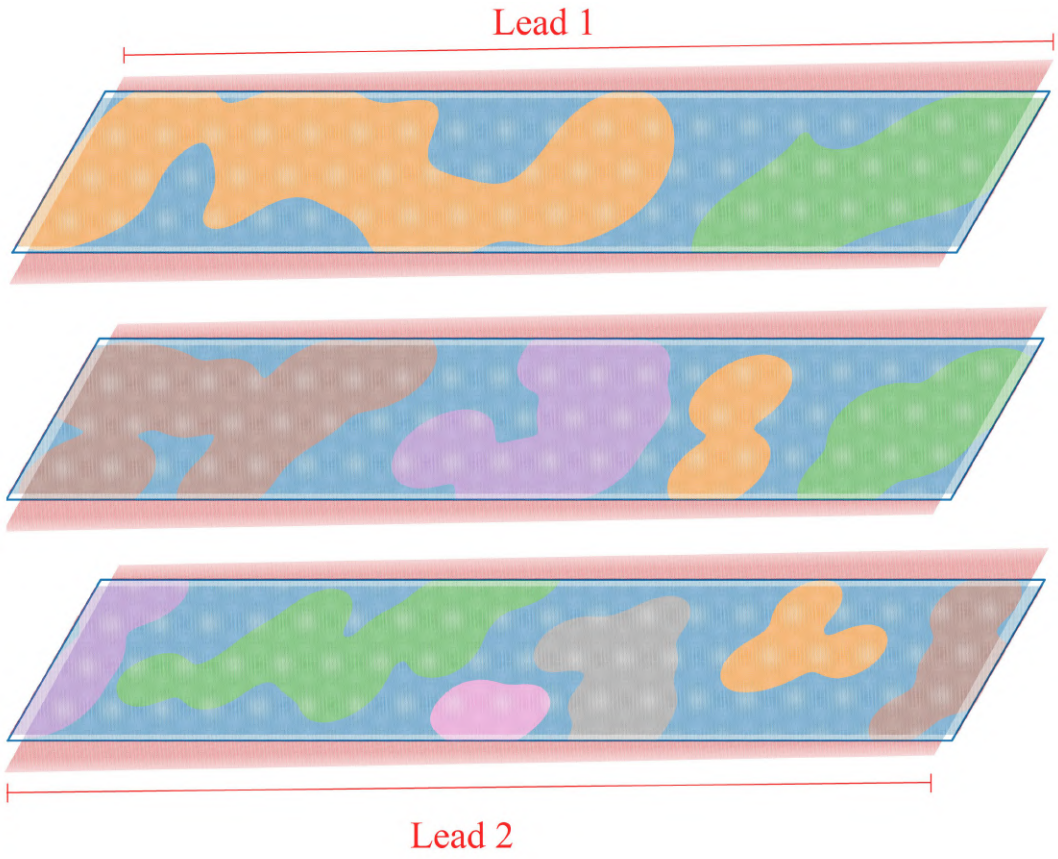

Figure 6.2: Three representative examples of two-terminal twisted bilayer graphene devices broken into N_d domains: (top panel) $N_d = 3$, (middle panel) $N_d = 5$ and (bottom panel)$N_d = 7$. Each color represents a singular domain.

between domain boundaries is not strongly suppressed unless the degree of twist angle mismatch is considerably larger than the values considered throughout this work [78]. Therefore, we believe that anyway domain boundaries have only marginal effects to our results.

Figure 6.2 shows three examples of disordered samples with $N_d = 3, 5$ and 7 twist angle domains. Each of these domains then gets assigned a slightly different equilibrium interlayer hopping amplitude $V_{pp\sigma}$ within the range $[V_{pp\sigma} - \delta V^0_{pp\sigma}, V_{pp\sigma} + \delta V^0_{pp\sigma}]$, sampled using a random uniform distribution. The disorder strength $\delta V^0_{pp\sigma}$ determines the degree of variation between the twist angle domains. To better keep track of the degree of twist angle disorder, variations of $V^0_{pp\sigma}$ are instead expressed using the equivalent twist angle variation $\delta\theta$. The conversion between these quantities is straightforward to extrapolate using the results discussed in the previous chapter (see Sec. 5.2).

Finally, we perform energy-resolved two-terminal conductance calculations on each sample and for each ensemble, and average the results for each ensemble. To make the leads metallic, *i.e.* with as many modes as possible, we use the same chemical potential in both leads that we

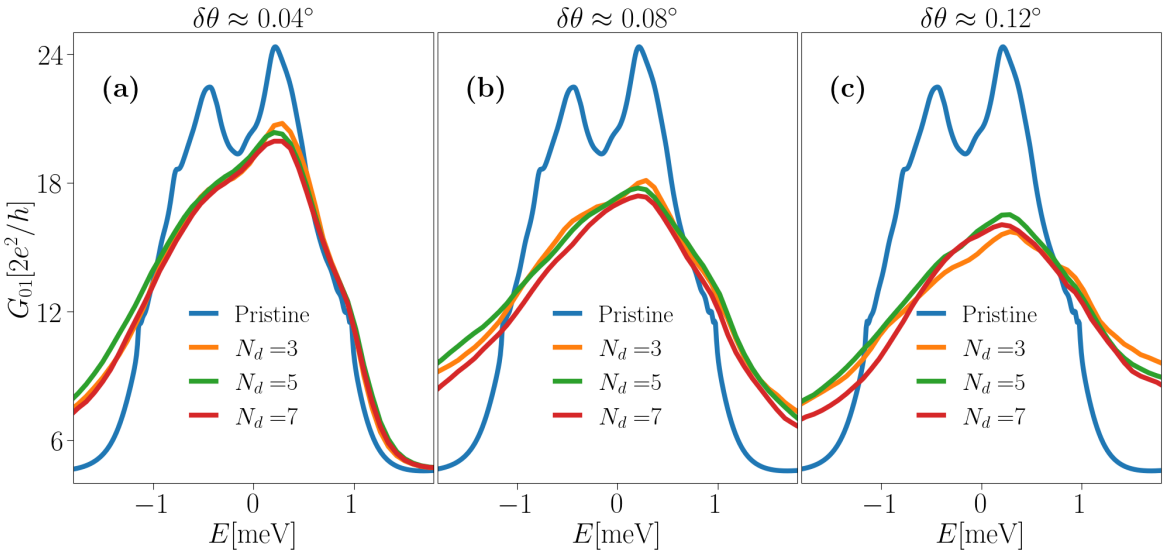

Figure 6.3: Energy-resolved averaged conductance $G(E)$ for ensembles with $N_d = 3, 5$, and 7 twist-angle domains. The effective twist angle disorder is the following: (a) $\delta\theta \approx 0.04°$ (corresponding to $\delta V^0_{pp\sigma} = 17\,\text{meV}$), (b) $\delta\theta \approx 0.08°$ ($\delta V^0_{pp\sigma} = 34\,\text{meV}$) and (c) $\delta\theta \approx 0.12°$ ($\delta V^0_{pp\sigma} = 51\,\text{meV}$). Each ensemble has 20 samples.

used in the previous chapter $\mu = 2\,\text{eV}$, which places the propagating modes deep in the bulk of the dispersion bands.

6.2 Effects of twist angle disorder

We begin by discussing the effects of twist angle disorder on the two-terminal conductance. The averaged wide-junction conductance $G_{01}(E)$ for three values of the disorder strength $\delta\theta$ and for three ensembles with different numbers of twist angle domains N_d is shown in Fig. 6.3. As is typical of disorder, $\delta\theta$ has the overall effect of suppressing and smearing the energy-resolved conductance curve $G_{01}(E)$. The sharp peaks in $G_{01}(E)$ associated with van Hove singularities in the moiré bands are significantly suppressed and broadened. It is shown that N_d has only a marginal effect on G_{01}, and $\delta\theta$ is clearly the dominant factor. Interestingly, the suppression of the conductance is not uniform in energy. The conductance is more suppressed in the hole bands, and this is the case for all values of $\delta\theta$ and N_d. Moreover, even at the lowest value of twist angle disorder considered $\delta\theta \approx 0.04°$, the conductance signature of the van Hove singularity in the hole bands is completely washed out. This is in contrast to the effects of twist angle disorder on the electron bands, where even at a disorder strength of $\delta\theta \approx 0.12°$ we can clearly discern a peak in the conductance that aligns with the energetic position of the van Hove singularity.

What makes one of the conductance peaks, the one in the electron bands, robust to twist angle disorder, while the one in the hole bands is so sensitive to it? To answer this question,

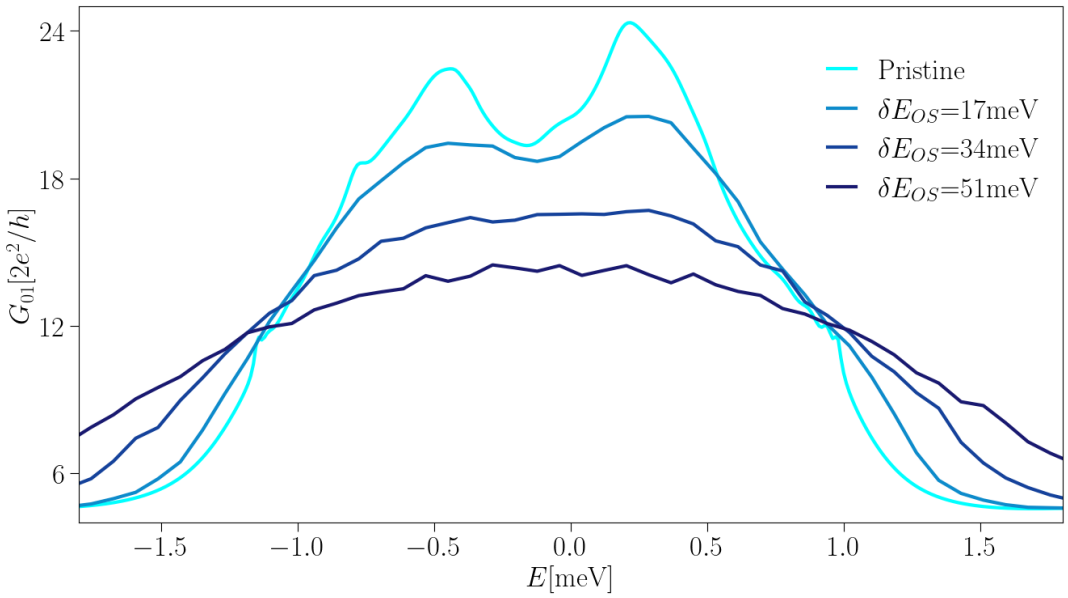

Figure 6.4: Energy-resolved averaged conductance $G_{01}(E)$ of ensembles of 20 samples with on-site energy disorder δE_{OS}.

we first investigate whether this is a peculiarity of twist angle disorder, instead of a typical effect of various types of disorder. Figure 6.4 shows the energy-resolved averaged wide-junction conductance $G_{01}(E)$ of an ensemble with on-site electrostatic potential disorder. To model this type of disorder, we simply shifted the on-site energy in each atom of the scattering region by a value sampled from a random uniform distribution. We induced the same degree of disorder to the on-site energy of the atoms that we used for the twist angle disorder in Fig. 6.3. As expected, the overall conductance is also suppressed and smeared by this electrostatic potential energy disorder. However, in this case the suppression is symmetric energy-wise, affecting the electron and hole bands to equal extent. Moreover, the effects of electrostatic potential energy disorder are shown to be more destructive. Even at lowest value of disorder considered $\delta E = 17\,\text{meV}$, the signatures of both van Hove singularities are mostly washed out.

Clearly, the asymmetric suppression of G_{01} is not a universal feature of disorder, but is specific to twist angle disorder. To answer why this is so, we recall the density of states of near-magic angle twisted bilayer graphene of the pristine, periodic crystal. Panel (b) in Fig. 6.5 shows the density of states of twisted bilayer graphene at the magic angle $\theta_m \approx 1.05°$, and its two closest commensurate angles are shown in panels (a) and (c) respectively. Notice that the density of states is largely symmetric energy-wise at angles above θ_m, but loses this approximate electron-hole symmetry at lower twist angles. In our effective tight-binding model, the density of states is essentially symmetric for all twist angles above θ_m, and it breaks just below this value. At the twist angle $\theta \approx 1.02°$ the density of states in the hole bands and the electron bands is very different. The density of states in the hole bands is more spread-out in energy than in the

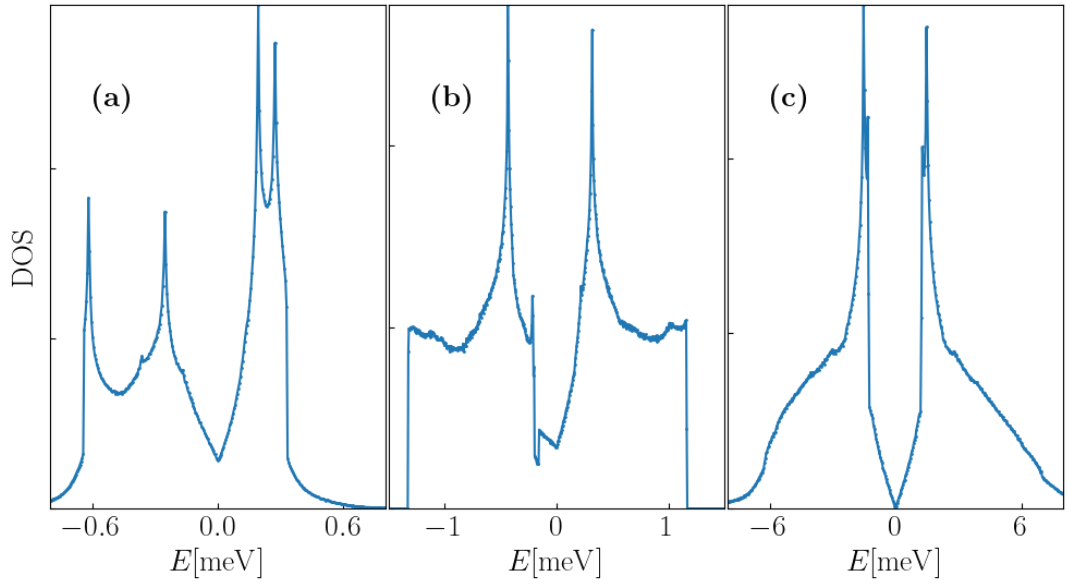

Figure 6.5: Density of states of near-magic angle twisted bilayer graphene. Panel (a) $\theta \approx 1.02°$, (b) $\theta \approx 1.05°$ and (c) $\theta \approx 1.08°$.

electron bands, and consequently it has lower peaks. On the contrary, the electron band peaks in G_{01} are very close to each other, and the overall effect is a sharper and more concentrated density of states for electrons than for holes. This is the reason for the asymmetric effect of twist angle disorder in G_{01}. Some of the twist angle domains have effective twist angles below θ_m, and thus their contribution to conductance will be affected by the density of states below the first magic angle, with its characteristic asymmetric shape.

To support our case that the asymmetry in the conductance curve is due to the asymmetry in the moiré bands, we can sum the normalized density of states of an ensemble of near-magic angle twisted bilayer graphene. Panel (a) in Fig. 6.6 shows the averaged density of states of magic angle twisted bilayer graphene with varying interlayer hopping amplitude in the range $V^0_{pp\sigma} \in [377, 403]$meV, corresponding to a twist angle variation of $\delta\theta \approx 0.03°$. The averaged density of states is clearly sharper and more tightly packed energy-wise in the electron bands, and more spread-out (and less pronounced) in the hole bands. To show that this effect is not simply a consequence of the averaging of the density of states, in panel (b) of Fig. 6.6 we also show the averaged density of states of twisted magic angle bilayer graphene with randomized Fermi level, sampled using a uniform distribution with the same energy variation as in panel (a). As expected, in this case the averaged density of states is essentially symmetric in energy, and shows no distinguishing feature between the hole and electron bands. At any twist angle above $\theta_m \approx 1.05°$ we find a symmetric averaged density of states using this type of Fermi-level randomization procedure, but not for lower twist angles.

The asymmetric suppression and broadening of the conductance G_{01} is a feature of twist

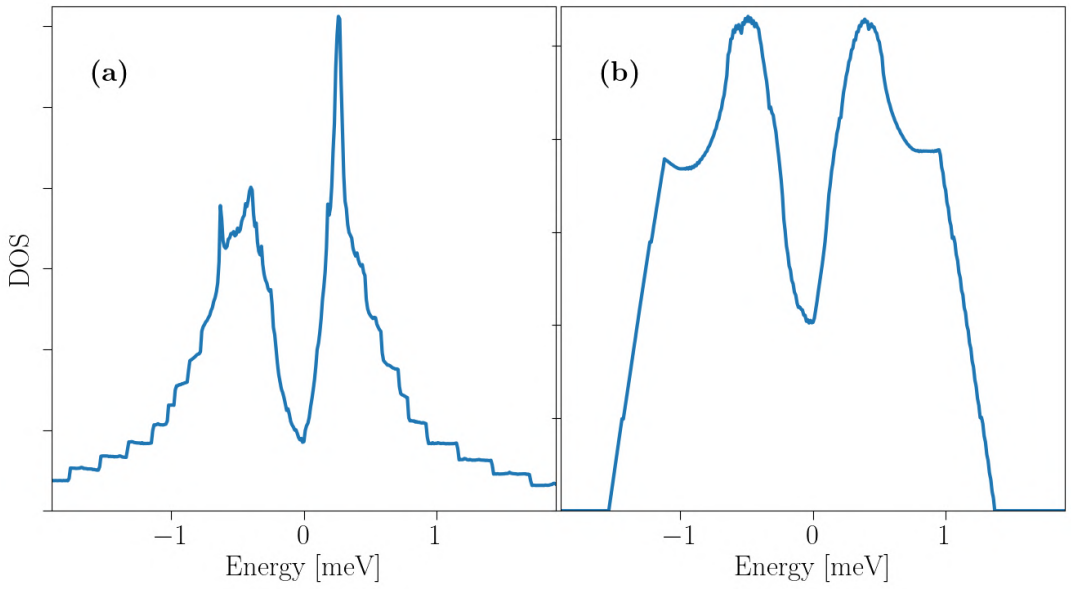

Figure 6.6: Density of states of magic-angle twisted bilayer graphene samples averaged over (a) an ensemble with interlayer hopping amplitude uniformly distributed within the range $V^0_{pp\sigma} \in [377, 403]$meV, and (b) an ensemble of samples with Fermi levels uniformly distributed within the range $E_f \in [-200, 200]$meV.

angle disorder only at twist angles near the first magic angle θ_m. If the effective twist angle is larger than this value, and the disorder strength is not sufficient to move the effective twist angle below the first magic angle in at least some twist angle domains, then the conductance will not show this asymmetric effect. We propose that this effect can be used to characterize disorder in real samples near the magic angle. However, at this point it is not clear whether this effect would still be noticeable in real measurements that are affected by temperature, Hartree interactions, lattice corrugation and other types of disorder. Below we discuss the effects of these phenomena on the conductance G_{01}.

6.3 Effects of temperature on the conductance

We typically expect that temperature will cause thermal broadening of the energy-resolved conductance and the smearing of peaks in the conductance curve. Unlike the effects of twist angle disorder, we expect this effect to be the same in both the electron and hole bands. Figure 6.7 shows the averaged conductance G_{01} of four sets of disordered ensembles at temperatures in the range $T \in [0, 5]$K. In panels (a) and (c) we show G_{01} of ensembles with twist angle disorder, where we used the number of domains $N_d = 3$ (since N_d only marginally affects G_{01}, we did not consider other values of N_d). For comparison, we also show samples with on-site energy disorder in panels (b) and (d). For the lowest value of twist angle disorder $\delta\theta \approx 0.04^\circ$ we can still see an asymmetric peak in the conductance at a temperature of $T = 5$K. However, at higher values of twist angle

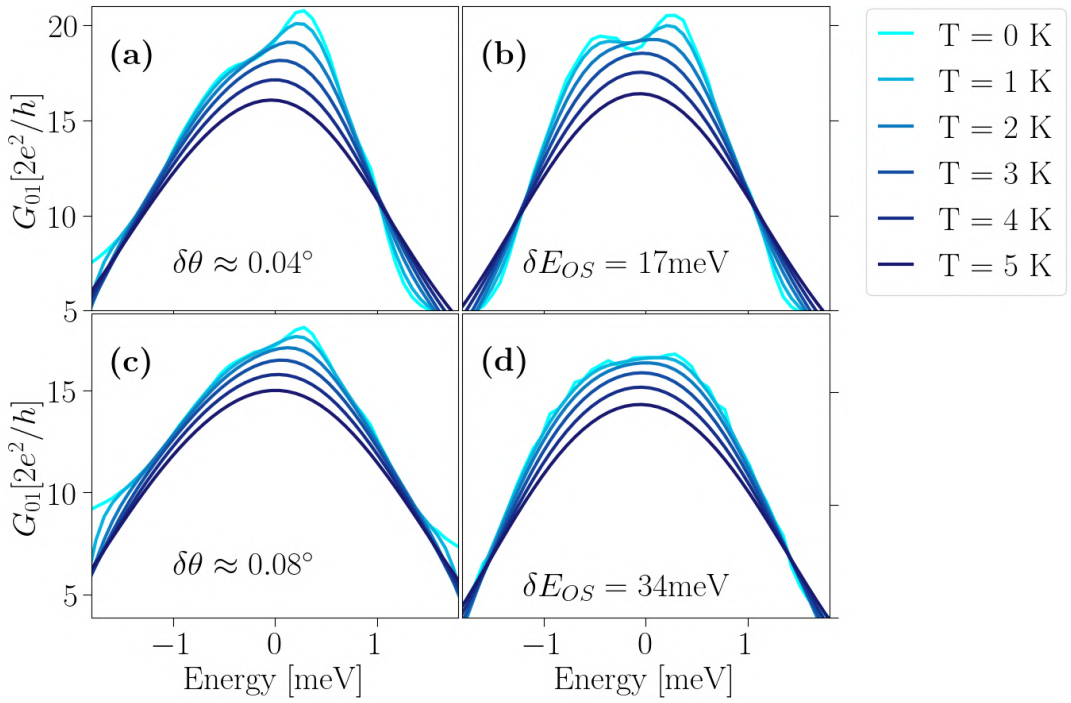

Figure 6.7: Averaged conductance $G(E)$ of magic-angle twisted bilayer graphene samples as a function temperatures for two values of twist angle disorder strength: (a) $\delta\theta \approx 0.04°$ ($\delta V^0_{pp\sigma}$ = 17 meV) and (c) $\delta\theta \approx 0.08°$ ($\delta V^0_{pp\sigma}$ = 34 meV; and for on-site-energy disorder strength: (b) δE_{OS} = 17 meV and (d) δE_{OS} = 34 meV.

disorder, the asymmetry is more and more difficult to notice. At $\delta\theta \approx 0.08°$ the asymmetry is still noticeable at a temperature of $T = 4$ K, but the curve is too washed out at $T = 5$ K to notice them. In the case of on-site energy disorder, the signatures of van Hove singularities vanish already at a temperature of $T = 2$ K, even at the lowest value of disorder considered, $\delta E \approx 0.04$ meV. Since the critical temperatures of the correlated phases in magic angle twisted bilayer graphene are typically in the range of $T_c \approx$ 1-2 K, our results indicate that the type and strength of disorder present in real samples can be characterized at reasonable temperatures where the correlated phenomena of magic-angle twisted bilayer graphene is still present.

6.4 Effects of Hartree interactions on the conductance

So far we have considered the non-interactive description of twisted bilayer graphene. However, in Sec. 2.3.3.2 we discussed how electron-electron interactions in twisted bilayer graphene lead to an inhomogeneous Hartree potential, resulting in significant distortions of the flat bands. Now, Hartree interactions vanish at a particular doping level, so even if their effect is too disruptive to our results we can always do away with them by tuning the electrostatic potential in twisted bilayer graphene samples. Nonetheless, let us consider the effect of these interactions. Recall

that Hartree interactions can be accounted for in our atomistic simulations with a simple on-site moiré-periodic Hartree potential:

$$V_H(\mathbf{r}) = V_\theta(\nu - \nu_\theta) \sum_{j=1,2,3} \cos\left(\mathbf{r}\cdot\mathbf{G}_j\right), \tag{6.2}$$

where V_θ is a twist angle dependent energy parameter, ν_θ is the doping level at which the Hartree potential vanishes, $\mathbf{G}_1, \mathbf{G}_2$ are the magic angle moiré reciprocal vectors, and $\mathbf{G}_3 = \mathbf{G}_1 + \mathbf{G}_2$. The magnitude of this Hartree potential depends on the screening, which is a function of the substrate and the electrostatic environment. In this work we parametrize the Hartree potential by an effective potential strength $\Delta\nu V_\theta$, where $\Delta\nu = (\nu - \nu_\theta)$, and we assume that $\Delta\nu V_\theta$ is of similar magnitude as the Hartree-Fock potentials appearing in the correlated phases of twisted bilayer graphene due to Coulomb interactions $\Delta\nu V_\theta/k_B \sim 1\,\mathrm{K}$.

The effects of the Hartree potential on the conductance G_{01} of the pristine sample are shown in Fig. 6.8. At a potential strength of $\Delta\nu V_\theta/k_B \sim 1\,\mathrm{K}$ the effects are marginal and would not affect the results shown in Fig. 6.3. Even at four times this value, at $\Delta\nu V_\theta/k_B \sim 4\,\mathrm{K}$, we can see both peaks in the conductance curve due to van Hove singularities, and therefore we expect the conductance to show the asymmetric effect of twist angle disorder. Therefore, our results indicate that Hartree interactions are not destructive enough to effectively smear the asymmetric effects of twist angle disorder in the energy-resolved conductance, and anyway the experimentalist can always tune the doping level to the point where the Hartree potential vanishes.

6.5 Effects of atomic corrugation on the conductance

Lattice relaxation processes break pristine crystals of twisted bilayer graphene into landscapes of twist angle domains. However, lattice relaxation also leads to lattice *corrugation* in the axis perpendicular to the plane of the crystal. This corrugation amounts to a displacement of the atoms in the out-of-plane direction [109–111]. In Sec. 2.3.3.1 we discussed this phenomenon, and we found that the corrugation can be included in our tight-binding model of twisted bilayer graphene by including a moiré-periodic displacement function:

$$z(\mathbf{r}) = \frac{\alpha}{3} \sum_{j=1,2,3} \cos\left(\mathbf{r}\cdot\mathbf{G}_j\right), \tag{6.3}$$

where α is the corrugation amplitude, and $\mathbf{G}_i\, i = 1, 2, 3$ are the same as in Eq. 6.2. The correction to the interlayer hoppings $t'(r)$ due to corrugation is shown in Eq. 2.37. Recall that the effective decay parameter λ' in the out-of-plane $z-$axis is not the same as the decay parameter λ in the in-plane surface. Because of different screenings, λ' is about twice the value of λ.

Figure 6.9 shows the effect of corrugation on the two-terminal energy-resolved conductance $G_{12}(E)$ of a pristine sample of twisted bilayer graphene. We again observe a broadening of the conductance curve and the smearing of signatures of van Hove singularities. This effect is

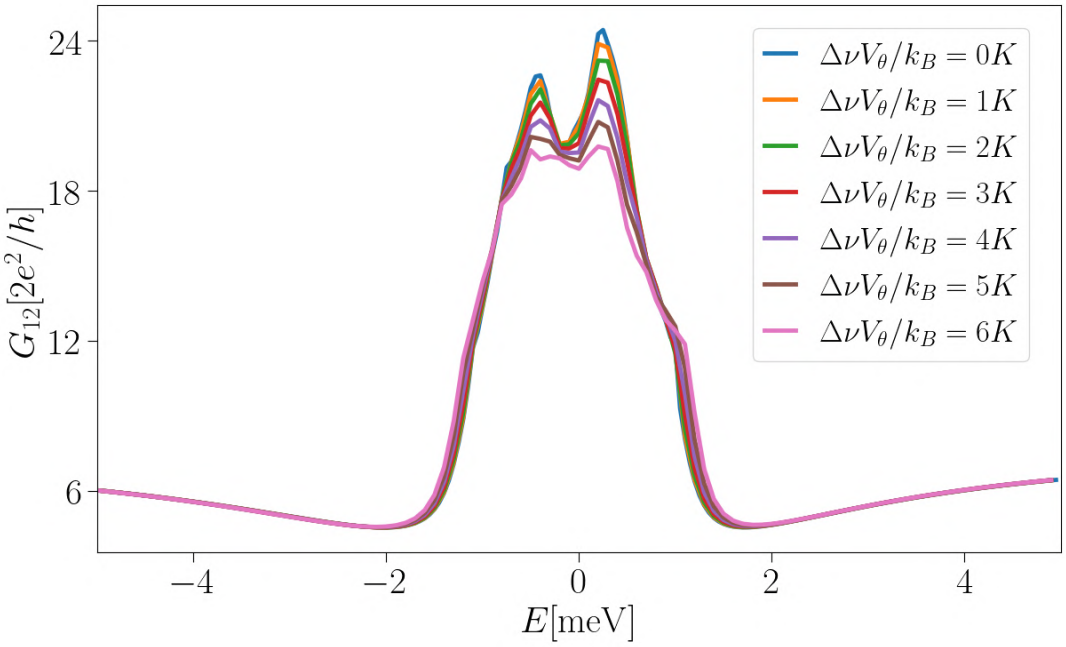

Figure 6.8: Energy-resolved conductance $G_{12}(E)$ of pristine magic-angle twisted bilayer graphene samples with different values of the effective Hartree potential strength expressed in units of temperature $\Delta\nu V_\theta/k_B$.

congruent with the broadening of the quasi-flat moiré bands of twisted bilayer graphene due to corrugation, as we detailed in Sec. 2.3.3.1. A corrugation amplitude of 1% of d_0, where d_0 is the uncorrugated distance between the graphene sheets, is not strong enough to completely smear the two peaks in the conductance. Recall that we do not have precise information regarding the degree of corrugation in realistic devices. Measurements of corrugation in real samples of twisted bilayer graphene are not precise, so it is difficult to know exactly what degree of corrugation can reasonably be expected to be present in devices. The only theoretical estimates of corrugation in twisted bilayer graphene find a value of $\Delta d \approx 7\%$ at the magic angle θ_m [56]. However, this estimate is based on density functional theory calculations of twisted bilayer graphene suspended in a vacuum. Real samples of twisted bilayer graphene are constructed with substrates in both graphene sheets, typically made of thin hBN layers, which is subsequently pressed together to stabilize the structure. Moreover, previous studies of corrugation in twisted bilayer graphene have found its effects in the moiré bands to be marginal. In our simulations, corrugation of $\Delta d > 1\%$ more than doubles the width of the moié bands. Therefore, we believe that realistic samples created with state-of-the-art experimental techniques will have an effective corrugation amplitute of less than the equivalent of $\Delta d > 1\%$ in our model. Within this range of corrugation, the peaks in the conductance due to van Hove singularities are still pronounced enough to be used to characterize samples using the asymmetric effect of twist angle disorder near the magic angle.

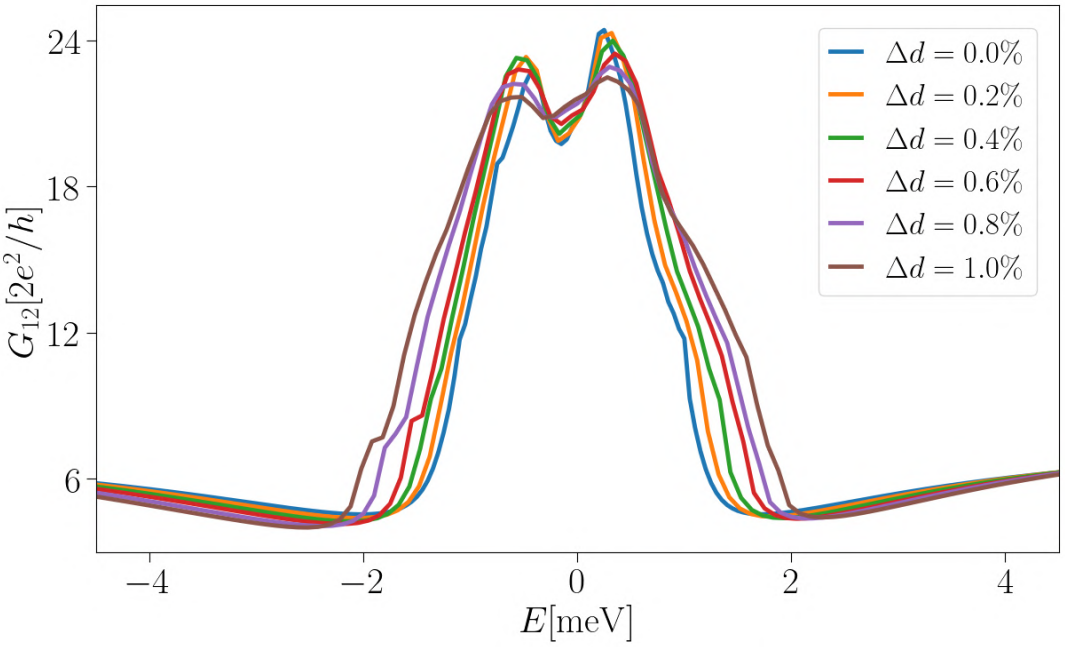

Figure 6.9: Energy-resolved conductance $G_{12}(E)$ of pristine magic-angle twisted bilayer graphene samples for different atomic corrugation values. Here $\Delta d = |d_{far} - d_{near}|$, and we express it as a percentage of the uncorrugated equilibrium interlayer distance $d_0 = 3.35\,\text{Å}$.

6.6 Summary

In this chapter, we investigated the effects of twist angle disorder on the conductance of magic angle twisted bilayer graphene. To achieve this, we used the interlayer hopping amplitude to induce disorder instead of directly distorting the lattice structure. We find that the effects of twist angle disorder are directly related to changes in the moiré quasi-flat bands due to the twist angle shift. The twist angle domains considered in our mesoscopic devices are in most cases larger than a few moiré unit cells, which is comparable to measured twist angle domains reported in the literature. We find that twist angle disorder leads to an asymmetric broadening of the energy-resolved conductance. The electron bands are much more resistant to twist angle disorder than the hole bands. We propose that this effect can be used to characterize disorder in real samples. For this to work, two main conditions must be met: (1) some disordered domains should have an effective twist angle below the first magic angle at which the energetic electron-hole symmetry of the bands is broken; (2) the combination of temperature, other types of disorder (such as electrostatic potential disorder), Hartree interaction effect, and lattice corrugation should be low enough to not completely smear-out the signatures of van Hove singularities on the conduction curve. We show that the critical temperature required to destroy the asymmetric feature of twist angle disorder is significantly higher than the critical temperature of the correlated phases of magic angle twisted bilayer graphene. Therefore, this asymmetry should be present within the

range of temperatures in which twisted bilayer graphene exhibits strongly correlated behavior. Moreover, the expected level of lattice disorder, Hartree interactions, and lattice corrugation in realistic samples is shown to be below the threshold required to effectively destroy all signatures of the asymmetric effects of twist angle disorder. Therefore, we are confident that the effects described in this chapter are robust enough to be observed in transport measurements of real twisted bilayer graphene samples created using state-of-the-art experimental techniques.

CHAPTER 7

OUTLOOK

The study of two-dimensional moiré superlattices has unveiled a rich landscape of tunable electronic and optical phenomena, offering unprecedented opportunities for both fundamental research and future technologies. The ability to engineer correlated states, superconductivity, and exotic band topology through twist angle control, strain, electrostatic gating, uniaxial pressure between layers, and more, makes these systems highly versatile platforms for quantum materials science. Potential applications range from ultra-low-power electronics to sensitive quantum sensors and on-demand optoelectronic devices, where tunability is a key advantage.

Twisted bilayer graphene, the focus of this work, was shown to exhibit unconventional correlated electron phenomena at certain small "magic angles." Although most of the interesting properties of twisted bilayer graphene are only present at low temperatures, and therefore the possibilities for device applications is limited, it constitutes a remarkable model-material to study strongly interacting systems, and possibly to build exceptionally sensitive high-frequency devices under controlled conditions. In this work we showed how van Hove singularities near the Fermi level can be exploited to further tune electron correlations. The zero-energy conductivity of a sample can be increased severalfold with a change in the Fermi level of only a few meVs.

At present, the field of twistronics faces several challenges that must be addressed before these systems can transition from laboratory discoveries to scalable technologies. One major hurdle is the precise fabrication of moiré heterostructures, which currently relies on painstaking manual assembly techniques, limiting reproducibility and large-scale production. Advances in automated stacking, epitaxial growth, and twist-angle control will be crucial for practical applications. Additionally, these systems are remarkably sensitive to various types of disorder, and many interesting properties are only available once disorder effects are significantly mitigated. Understanding and mitigating these sources of disorder will be essential for achieving reliable

and uniform devices. In this work we discussed how twist angle disorder affects the energy-resolved conductance. This type of disorder is particularly disruptive, since it is to a certain extent unavoidable and uncontrollable. Any twisted bilayer graphene mesoscopic device, no matter how carefully prepared, breaks down into a landscape of twist angle domains due to lattice relaxation processes inherent in the material. However, in this work we showed that this type of disorder has characteristic effects that allows us to use it in real devices to characterize real devices and quantify the magnitude of disorder present in a given sample. We showed how the characteristic effects of twist angle disorder can reasonably be expected to be observed in real samples under typical laboratory conditions.

Despite the obstacles, the rapid progress in the field of twistronics suggests that many of these challenges can be overcome with continued research. Theoretical advances in understanding disorder effects, combined with improved experimental techniques for material synthesis and characterization, will pave the way for more robust and scalable moiré devices. As the field matures, the unique tunability of two-dimensional moiré superlattices may well revolutionize quantum technologies and beyond, bridging the gap between fundamental physics and real-world applications.

BIBLIOGRAPHY

[1] K. S. Novoselov, D. Jiang, F. Schedin, T. J. Booth, V. V. Khotkevich, S. V. Morozov, and A. K. Geim. Two-dimensional atomic crystals. *Proceedings of the National Academy of Sciences*, 102(30):10451–10453, 2005.

[2] Robert J. Young, Ian A. Kinloch, Lei Gong, and Kostya S. Novoselov. The mechanics of graphene nanocomposites: A review. *Composites Science and Technology*, 72(12):1459–1476, 2012.

[3] I. Snyman and C. W. J. Beenakker. Ballistic transmission through a graphene bilayer. *Phys. Rev. B*, 75:045322, Jan 2007.

[4] M. I. Katsnelson. Zitterbewegung, chirality, and minimal conductivity in graphene. *The European Physical Journal B - Condensed Matter and Complex Systems*, 51(2):157–160, May 2006.

[5] K.M. Janavika and Ravi Prakash Thangaraj. Graphene and its application: A review. *Materials Today: Proceedings*, 2023.

[6] J. Tworzydło, B. Trauzettel, M. Titov, A. Rycerz, and C. W. J. Beenakker. Sub-Poissonian Shot Noise in Graphene. *Phys. Rev. Lett.*, 96:246802, Jun 2006.

[7] Ziyi Han, Ruijie Zhang, Menghan Li, Lin Li, Dechao Geng, and Wenping Hu. Recent advances in the controlled chemical vapor deposition growth of bilayer 2d single crystals. *J. Mater. Chem. C*, 10:13324–13350, 2022.

[8] Peng Cheng, Wen Zhang, Lei Zhang, Jian Gou, Ping Kwan Johnny Wong, and Lan Chen. Chapter 4 - molecular beam epitaxy fabrication of two-dimensional materials. *2D Semiconductor Materials and Devices*, pages 103–134, 2020.

[9] A.V. Rozhkov, A.O. Sboychakov, A.L. Rakhmanov, and Franco Nori. Electronic properties of graphene-based bilayer systems. *Physics Reports*, 648:1–104, August 2016.

[10] V. N. Davydov. Some peculiarities of thermopower at the lifshitz topological transitions due to stacking change in bilayer and multilayer graphene. *Proceedings of the Royal Society A: Mathematical, Physical and Engineering Sciences*, 475(2226):20190028, June 2019.

[11] Zhengguang Lu, Tonghang Han, Yuxuan Yao, Aidan P. Reddy, Jixiang Yang, Junseok Seo, Kenji Watanabe, Takashi Taniguchi, Liang Fu, and Long Ju. Fractional quantum anomalous hall effect in multilayer graphene. *Nature*, 626(8000):759–764, Feb 2024.

[12] Rafi Bistritzer and A. H. MacDonald. Moire bands in twisted double-layer graphene. *Proceedings of the National Academy of Sciences*, 108(30):12233–12237, jul 2011.

[13] E. Suárez Morell, J. D. Correa, P. Vargas, M. Pacheco, and Z. Barticevic. Flat bands in slightly twisted bilayer graphene: Tight-binding calculations. *Phys. Rev. B*, 82:121407, Sep 2010.

[14] Yuan Cao, Valla Fatemi, Shiang Fang, Kenji Watanabe, Takashi Taniguchi, Efthimios Kaxiras, and Pablo Jarillo-Herrero. Unconventional superconductivity in magic-angle graphene superlattices. *Nature*, 556(7699):43, mar 2018.

[15] Yuan Cao, Valla Fatemi, Ahmet Demir, Shiang Fang, Spencer L. Tomarken, Jason Y. Luo, Javier D. Sanchez-Yamagishi, Kenji Watanabe, Takashi Taniguchi, Efthimios Kaxiras, Ray C. Ashoori, and Pablo Jarillo-Herrero. Correlated insulator behaviour at half-filling in magic-angle graphene superlattices. *Nature*, 556, Apr 2018.

[16] Mei-Yan Tian, Yu-Meng Gao, Yue-Jiao Zhang, Meng-Xue Ren, Xiao-Huan Lv, Ke-Xin Hou, Chen-Dong Jin, Hu Zhang, Ru-Qian Lian, Peng-Lai Gong, Rui-Ning Wang, Jiang-Long Wang, and Xing-Qiang Shi. Toward direct band gaps in typical 2d transition-metal dichalcogenides junctions via real and energy spaces tuning. *Communications Materials*, 5(1):188, Sep 2024.

[17] A. Chaves, J. G. Azadani, Hussain Alsalman, D. R. da Costa, R. Frisenda, A. J. Chaves, Seung Hyun Song, Y. D. Kim, Daowei He, Jiadong Zhou, A. Castellanos-Gomez, F. M. Peeters, Zheng Liu, C. L. Hinkle, Sang-Hyun Oh, Peide D. Ye, Steven J. Koester, Young Hee Lee, Ph. Avouris, Xinran Wang, and Tony Low. Bandgap engineering of two-dimensional semiconductor materials. *npj 2D Materials and Applications*, 4(1):29, Aug 2020.

[18] Sudipta Kundu, Tomer Amit, H. R. Krishnamurthy, Manish Jain, and Sivan Refaely-Abramson. Exciton fine structure in twisted transition metal dichalcogenide heterostructures. *npj Computational Materials*, 9(1):186, Oct 2023.

[19] Trithep Devakul, Valentin Crépel, Yang Zhang, and Liang Fu. Magic in twisted transition metal dichalcogenide bilayers. *Nature Communications*, 12(1):6730, Nov 2021.

[20] Aleksander Sanjuan Ciepielewski, Jakub Tworzydło, Timo Hyart, and Alexander Lau. Transport signatures of van hove singularities in mesoscopic twisted bilayer graphene. *Phys. Rev. Res.*, 4:043145, Nov 2022.

[21] Gui-Bin Liu, Wen-Yu Shan, Yugui Yao, Wang Yao, and Di Xiao. Three-band tight-binding model for monolayers of group-vib transition metal dichalcogenides. *Phys. Rev. B*, 88:085433, Aug 2013.

[22] Alexander Lau, Rajyavardhan Ray, Dániel Varjas, and Anton R. Akhmerov. Influence of lattice termination on the edge states of the quantum spin hall insulator monolayer $1T^{'}-\mathrm{wte}_2$. *Phys. Rev. Mater.*, 3:054206, May 2019.

[23] Srivani Javvaji, Fengping Li, and Jeil Jung. Ab initio tight-binding models for mono- and bilayer hexagonal boron nitride (h-bn). *Phys. Rev. Mater.*, 9:024004, Feb 2025.

[24] Aleksander Sanjuan Ciepielewski, Jakub Tworzydło, Timo Hyart, and Alexander Lau. Transport effects of twist-angle disorder in mesoscopic twisted bilayer graphene. *Nanotechnology*, 36(6):065401, nov 2024.

[25] Kyounghwan Kim, Ashley DaSilva, Shengqiang Huang, Babak Fallahazad, Stefano Larentis, Takashi Taniguchi, Kenji Watanabe, Brian J. LeRoy, Allan H. MacDonald, and Emanuel Tutuc. Tunable moiré bands and strong correlations in small-twist-angle bilayer graphene. *Proceedings of the National Academy of Sciences*, 114(13):3364–3369, March 2017.

[26] Jianpeng Liu, Junwei Liu, and Xi Dai. Pseudo Landau level representation of twisted bilayer graphene: Band topology and implications on the correlated insulating phase. *Phys. Rev. B*, 99:155415, Apr 2019.

[27] Noah F. Q. Yuan, Hiroki Isobe, and Liang Fu. Magic of high-order van Hove singularity. *Nature Communications*, 10(1):5769, December 2019.

[28] Zhida Song, Zhijun Wang, Wujun Shi, Gang Li, Chen Fang, and B. Andrei Bernevig. All Magic Angles in Twisted Bilayer Graphene are Topological. *Phys. Rev. Lett.*, 123:036401, Jul 2019.

[29] Xiaobo Lu, Petr Stepanov, Wei Yang, Ming Xie, Mohammed Ali Aamir, Ipsita Das, Carles Urgell, Kenji Watanabe, Takashi Taniguchi, Guangyu Zhang, Adrian Bachtold, Allan H. MacDonald, and Dmitri K. Efetov. Superconductors, orbital magnets and correlated states in magic-angle bilayer graphene. *Nature*, 574(7780):653–657, oct 2019.

[30] Grigory Tarnopolsky, Alex Jura Kruchkov, and Ashvin Vishwanath. Origin of Magic Angles in Twisted Bilayer Graphene. *Phys. Rev. Lett.*, 122:106405, Mar 2019.

[31] Matthew Yankowitz, Shaowen Chen, Hryhoriy Polshyn, Yuxuan Zhang, K. Watanabe, T. Taniguchi, David Graf, Andrea F. Young, and Cory R. Dean. Tuning superconductivity in twisted bilayer graphene. *Science*, 363(6431):1059–1064, March 2019.

[32] Bikash Padhi and Philip W. Phillips. Pressure-induced metal-insulator transition in twisted bilayer graphene. *Phys. Rev. B*, 99:205141, May 2019.

[33] Eva Y. Andrei and Allan H. MacDonald. Graphene bilayers with a twist. *Nature Materials*, 19(12):1265–1275, November 2020.

[34] Risto Ojajärvi, Timo Hyart, Mihail A. Silaev, and Tero T. Heikkilä. Competition of electron-phonon mediated superconductivity and Stoner magnetism on a flat band. *Phys. Rev. B*, 98:054515, Aug 2018.

[35] Hiroki Isobe, Noah F. Q. Yuan, and Liang Fu. Unconventional Superconductivity and Density Waves in Twisted Bilayer Graphene. *Phys. Rev. X*, 8:041041, Dec 2018.

[36] Fengcheng Wu, A. H. MacDonald, and Ivar Martin. Theory of Phonon-Mediated Superconductivity in Twisted Bilayer Graphene. *Physical Review Letters*, 121(25):257001, dec 2018.

[37] Teemu J. Peltonen, Risto Ojajärvi, and Tero T. Heikkilä. Mean-field theory for superconductivity in twisted bilayer graphene. *Phys. Rev. B*, 98:220504, Dec 2018.

[38] Vladyslav Kozii, Hiroki Isobe, Jörn W. F. Venderbos, and Liang Fu. Nematic superconductivity stabilized by density wave fluctuations: Possible application to twisted bilayer graphene. *Phys. Rev. B*, 99:144507, Apr 2019.

[39] Tamaghna Hazra, Nishchhal Verma, and Mohit Randeria. Bounds on the Superconducting Transition Temperature : Applications to Twisted Bilayer Graphene and Cold Atoms. *Physical Review X*, 9(3):31049, 2019.

[40] Xiang Hu, Timo Hyart, Dmitry I. Pikulin, and Enrico Rossi. Geometric and conventional contribution to the superfluid weight in twisted bilayer graphene. *Phys. Rev. Lett.*, 123:237002, Dec 2019.

[41] Fang Xie, Zhida Song, Biao Lian, and B. Andrei Bernevig. Topology-Bounded Superfluid Weight in Twisted Bilayer Graphene. *Phys. Rev. Lett.*, 124:167002, Apr 2020.

[42] A. Julku, T. J. Peltonen, L. Liang, T. T. Heikkilä, and P. Törmä. Superfluid weight and Berezinskii-Kosterlitz-Thouless transition temperature of twisted bilayer graphene. *Phys. Rev. B*, 101:060505, Feb 2020.

[43] Stephen Carr, Daniel Massatt, Shiang Fang, Paul Cazeaux, Mitchell Luskin, and Efthimios Kaxiras. Twistronics: Manipulating the electronic properties of two-dimensional layered structures through their twist angle. *Phys. Rev. B*, 95:075420, Feb 2017.

[44] Léon Van Hove. The Occurrence of Singularities in the Elastic Frequency Distribution of a Crystal. *Phys. Rev.*, 89:1189–1193, Mar 1953.

[45] Philipp Rosenzweig, Hrag Karakachian, Dmitry Marchenko, Kathrin Küster, and Ulrich Starke. Overdoping graphene beyond the van hove singularity. *Phys. Rev. Lett.*, 125:176403, Oct 2020.

[46] Y. F. Suprunenko, E. V. Gorbar, V. M. Loktev, and S. G. Sharapov. Effect of next-nearest-neighbor hopping on the electronic properties of graphene. *Low Temperature Physics*, 34(10):812–817, 10 2008.

[47] N. M. R. Peres, F. Guinea, and A. H. Castro Neto. Electronic properties of disordered two-dimensional carbon. *Phys. Rev. B*, 73:125411, Mar 2006.

[48] P. Plochocka, C. Faugeras, M. Orlita, M. L. Sadowski, G. Martinez, M. Potemski, M. O. Goerbig, J.-N. Fuchs, C. Berger, and W. A. de Heer. High-energy limit of massless dirac fermions in multilayer graphene using magneto-optical transmission spectroscopy. *Phys. Rev. Lett.*, 100:087401, Feb 2008.

[49] Gilles Montambaux. Artificial graphenes: Dirac matter beyond condensed matter. *Comptes Rendus. Physique*, 19(5):285–305, 2018.

[50] F. D. M. Haldane. Model for a quantum hall effect without landau levels: Condensed-matter realization of the "parity anomaly". *Phys. Rev. Lett.*, 61:2015–2018, Oct 1988.

[51] Liu Yang and Qing-Dong Jiang. Emergent haldane model and photon-valley locking in chiral cavities. *Communications Physics*, 8(1):126, Apr 2025.

[52] P. R. Wallace. The band theory of graphite. *Phys. Rev.*, 71:622–634, May 1947.

[53] A. H. Castro Neto, F. Guinea, N. M. R. Peres, K. S. Novoselov, and A. K. Geim. The electronic properties of graphene. *Rev. Mod. Phys.*, 81:109–162, Jan 2009.

[54] Edward McCann and Mikito Koshino. The electronic properties of bilayer graphene. *Reports on Progress in Physics*, 76(5):056503, apr 2013.

[55] M. I. Katsnelson. Minimal conductivity in bilayer graphene. *The European Physical Journal B*, 52(2):151–153, July 2006.

[56] Kazuyuki Uchida, Shinnosuke Furuya, Jun-Ichi Iwata, and Atsushi Oshiyama. Atomic corrugation and electron localization due to moiré patterns in twisted bilayer graphenes. *Phys. Rev. B*, 90:155451, Oct 2014.

[57] Mikito Koshino, Noah F. Q. Yuan, Takashi Koretsune, Masayuki Ochi, Kazuhiko Kuroki, and Liang Fu. Maximally localized wannier orbitals and the extended hubbard model for twisted bilayer graphene. *Phys. Rev. X*, 8:031087, Sep 2018.

[58] J. M. B. Lopes dos Santos, N. M. R. Peres, and A. H. Castro Neto. Continuum model of the twisted graphene bilayer. *Phys. Rev. B*, 86:155449, Oct 2012.

[59] Zhi-Da Song and B. Andrei Bernevig. Magic-angle twisted bilayer graphene as a topological heavy fermion problem. *Phys. Rev. Lett.*, 129:047601, Jul 2022.

[60] Guohong Li, A. Luican, J. M. B. Lopes dos Santos, A. H. Castro Neto, A. Reina, J. Kong, and E. Y. Andrei. Observation of Van Hove singularities in twisted graphene layers. *Nature Physics*, 6(2):109–113, November 2009.

[61] Alexander Kerelsky, Leo J. McGilly, Dante M. Kennes, Lede Xian, Matthew Yankowitz, Shaowen Chen, K. Watanabe, T. Taniguchi, James Hone, Cory Dean, Angel Rubio, and Abhay N. Pasupathy. Maximized electron interactions at the magic angle in twisted bilayer graphene. *Nature*, 572(7767):95–100, July 2019.

[62] Youngjoon Choi, Jeannette Kemmer, Yang Peng, Alex Thomson, Harpreet Arora, Robert Polski, Yiran Zhang, Hechen Ren, Jason Alicea, Gil Refael, Felix von Oppen, Kenji Watanabe, Takashi Taniguchi, and Stevan Nadj-Perge. Electronic correlations in twisted bilayer graphene near the magic angle. *Nature Physics*, 15(11):1174–1180, August 2019.

[63] Xianqing Lin and David Tománek. Minimum model for the electronic structure of twisted bilayer graphene and related structures. *Phys. Rev. B*, 98:081410, Aug 2018.

[64] M. S. Tang, C. Z. Wang, C. T. Chan, and K. M. Ho. Environment-dependent tight-binding potential model. *Phys. Rev. B*, 53:979–982, Jan 1996.

[65] W. Landgraf, S. Shallcross, K. Türschmann, D. Weckbecker, and O. Pankratov. Electronic structure of twisted graphene flakes. *Phys. Rev. B*, 87:075433, Feb 2013.

[66] Shengqiang Huang, Kyounghwan Kim, Dmitry K. Efimkin, Timothy Lovorn, Takashi Taniguchi, Kenji Watanabe, Allan H. MacDonald, Emanuel Tutuc, and Brian J. LeRoy. Topologically protected helical states in minimally twisted bilayer graphene. *Phys. Rev. Lett.*, 121:037702, Jul 2018.

[67] S. L. Tomarken, Y. Cao, A. Demir, K. Watanabe, T. Taniguchi, P. Jarillo-Herrero, and R. C. Ashoori. Electronic compressibility of magic-angle graphene superlattices. *Phys. Rev. Lett.*, 123:046601, Jul 2019.

[68] Francisco Guinea and Niels R. Walet. Electrostatic effects, band distortions, and superconductivity in twisted graphene bilayers. *Proceedings of the National Academy of Sciences*, 115(52):13174–13179, 2018.

[69] Tommaso Cea, Niels R. Walet, and Francisco Guinea. Electronic band structure and pinning of fermi energy to van hove singularities in twisted bilayer graphene: A self-consistent approach. *Phys. Rev. B*, 100:205113, Nov 2019.

[70] Louk Rademaker, Dmitry A. Abanin, and Paula Mellado. Charge smoothening and band flattening due to hartree corrections in twisted bilayer graphene. *Phys. Rev. B*, 100:205114, Nov 2019.

[71] Zachary A H Goodwin, Valerio Vitale, Xia Liang, Arash A Mostofi, and Johannes Lischner. Hartree theory calculations of quasiparticle properties in twisted bilayer graphene. *Electronic Structure*, 2(3):034001, aug 2020.

[72] Zachary A. H. Goodwin, Valerio Vitale, Fabiano Corsetti, Dmitri K. Efetov, Arash A. Mostofi, and Johannes Lischner. Critical role of device geometry for the phase diagram of twisted bilayer graphene. *Phys. Rev. B*, 101:165110, Apr 2020.

[73] Supriyo Datta. *Quantum Transport: Atom to Transistor*. Cambridge University Press, 2005.

[74] David K Ferry, Xavier Oriols, and Josef Weinbub. *Quantum Transport in Semiconductor Devices*. 2053-2563. IOP Publishing, 2023.

[75] C.W.J. Beenakker and H. van Houten. Quantum transport in semiconductor nanostructures. In Henry Ehrenreich and David Turnbull, editors, *Semiconductor Heterostructures and Nanostructures*, volume 44 of *Solid State Physics*, pages 1–228. Academic Press, 1991.

[76] Alexandre Jaoui, Ipsita Das, Giorgio Di Battista, Jaime Díez-Mérida, Xiaobo Lu, Kenji Watanabe, Takashi Taniguchi, Hiroaki Ishizuka, Leonid Levitov, and Dmitri K. Efetov. Quantum critical behaviour in magic-angle twisted bilayer graphene. *Nature Physics*, 18(6):633–638, Jun 2022.

[77] Sandeep Joy, Saad Khalid, and Brian Skinner. Transparent mirror effect in twist-angle-disordered bilayer graphene. *Phys. Rev. Res.*, 2:043416, Dec 2020.

[78] Héctor Sainz-Cruz, Tommaso Cea, Pierre A. Pantaleón, and Francisco Guinea. High transmission in twisted bilayer graphene with angle disorder. *Phys. Rev. B*, 104:075144, Aug 2021.

[79] Aditya Jayaraman, Kimberly Hsieh, Bhaskar Ghawri, Phanibhusan S. Mahapatra, Kenji Watanabe, Takashi Taniguchi, and Arindam Ghosh. Evidence of lifshitz transition in the thermoelectric power of ultrahigh-mobility bilayer graphene. *Nano Letters*, 21(3):1221–1227, January 2021.

[80] E. H. Hwang and S. Das Sarma. Impurity-scattering-induced carrier transport in twisted bilayer graphene. *Phys. Rev. Research*, 2:013342, Mar 2020.

[81] Bikash Padhi, Apoorv Tiwari, Titus Neupert, and Shinsei Ryu. Transport across twist angle domains in moiré graphene. *Phys. Rev. Research*, 2:033458, Sep 2020.

[82] David K Ferry, Josef Weinbub, Mihail Nedjalkov, and Siegfried Selberherr. A review of quantum transport in field-effect transistors. *Semiconductor Science and Technology*, 37(4):043001, feb 2022.

[83] Yanjie Shao, Marco Pala, Hao Tang, Baoming Wang, Ju Li, David Esseni, and Jesús A. del Alamo. Scaled vertical-nanowire heterojunction tunnelling transistors with extreme quantum confinement. *Nature Electronics*, Nov 2024.

[84] B. J. van Wees, H. van Houten, C. W. J. Beenakker, J. G. Williamson, L. P. Kouwenhoven, D. van der Marel, and C. T. Foxon. Quantized conductance of point contacts in a two-dimensional electron gas. *Phys. Rev. Lett.*, 60:848–850, Feb 1988.

[85] D A Wharam, T J Thornton, R Newbury, M Pepper, H Ahmed, J E F Frost, D G Hasko, D C Peacock, D A Ritchie, and G A C Jones. One-dimensional transport and the quantisation of the ballistic resistance. *Journal of Physics C: Solid State Physics*, 21(8):L209, mar 1988.

[86] Christoph W Groth, Michael Wimmer, Anton R Akhmerov, and Xavier Waintal. Kwant: a software package for quantum transport. *New Journal of Physics*, 16(6):063065, June 2014.

[87] Fengcheng Wu, Euyheon Hwang, and Sankar Das Sarma. Phonon-induced giant linear-in-T resistivity in magic angle twisted bilayer graphene: Ordinary strangeness and exotic superconductivity. *Phys. Rev. B*, 99:165112, Apr 2019.

[88] M. Andelković, L. Covaci, and F. M. Peeters. DC conductivity of twisted bilayer graphene: Angle-dependent transport properties and effects of disorder. *Phys. Rev. Materials*, 2:034004, Mar 2018.

[89] Zhe Hou, Ya-Yun Hu, and Guang-Wen Yang. Moiré pattern assisted commensuration resonance in disordered twisted bilayer graphene. *Phys. Rev. B*, 109:085412, Feb 2024.

[90] Luis A. Gonzalez-Arraga, J. L. Lado, Francisco Guinea, and Pablo San-Jose. Electrically controllable magnetism in twisted bilayer graphene. *Phys. Rev. Lett.*, 119:107201, Sep 2017.

[91] Dario A. Bahamon, G. Gómez-Santos, and T. Stauber. Emergent magnetic texture in driven twisted bilayer graphene. *Nanoscale*, 12(28):15383–15392, 2020.

[92] Javad Vahedi, Robert Peters, Ahmed Missaoui, Andreas Honecker, and Guy Trambly de Laissardière. Magnetism of magic-angle twisted bilayer graphene. *SciPost Phys.*, 11:083, 2021.

[93] B. H. Zhou, W. H. Liao, B. L. Zhou, K.-Q. Chen, and G. H. Zhou. Electronic transport for a crossed graphene nanoribbon junction with and without doping. *The European Physical Journal B*, 76(3):421–425, June 2010.

[94] Pedro Brandimarte, Mads Engelund, Nick Papior, Aran Garcia-Lekue, Thomas Frederiksen, and Daniel Sánchez-Portal. A tunable electronic beam splitter realized with crossed graphene nanoribbons. *The Journal of Chemical Physics*, 146(9):092318, March 2017.

[95] Sofia Sanz, Pedro Brandimarte, Géza Giedke, Daniel Sánchez-Portal, and Thomas Frederiksen. Crossed graphene nanoribbons as beam splitters and mirrors for electron quantum optics. *Phys. Rev. B*, 102:035436, Jul 2020.

[96] Liying Jiao, Li Zhang, Lei Ding, Jie Liu, and Hongjie Dai. Aligned graphene nanoribbons and crossbars from unzipped carbon nanotubes. *Nano Research*, 3(6):387–394, April 2010.

[97] A. Inbar, J. Birkbeck, J. Xiao, T. Taniguchi, K. Watanabe, B. Yan, Y. Oreg, Ady Stern, E. Berg, and S. Ilani. The quantum twisting microscope. *Nature*, 614(7949):682–687, Feb 2023.

[98] Mitsutaka Fujita, Katsunori Wakabayashi, Kyoko Nakada, and Koichi Kusakabe. Peculiar localized state at zigzag graphite edge. *Journal of the Physical Society of Japan*, 65(7):1920–1923, 1996.

[99] J. M. B. Lopes dos Santos, N. M. R. Peres, and A. H. Castro Neto. Graphene Bilayer with a Twist: Electronic Structure. *Phys. Rev. Lett.*, 99:256802, Dec 2007.

[100] Stephen Carr, Shiang Fang, Pablo Jarillo-Herrero, and Efthimios Kaxiras. Pressure dependence of the magic twist angle in graphene superlattices. *Phys. Rev. B*, 98:085144, Aug 2018.

[101] Matthew Yankowitz, Shaowen Chen, Hryhoriy Polshyn, Yuxuan Zhang, K. Watanabe, T. Taniguchi, David Graf, Andrea F. Young, and Cory R. Dean. Tuning superconductivity in twisted bilayer graphene. *Science*, 363(6431):1059–1064, 2019.

[102] A. Uri, S. Grover, Y. Cao, J. A. Crosse, K. Bagani, D. Rodan-Legrain, Y. Myasoedov, K. Watanabe, T. Taniguchi, P. Moon, M. Koshino, P. Jarillo-Herrero, and E. Zeldov. Mapping the twist-angle disorder and landau levels in magic-angle graphene. *Nature*, 581(7806):47–52, May 2020.

[103] Kyoko Nakada, Mitsutaka Fujita, Gene Dresselhaus, and Mildred S. Dresselhaus. Edge state in graphene ribbons: Nanometer size effect and edge shape dependence. *Phys. Rev. B*, 54:17954–17961, Dec 1996.

[104] Tobias A. de Jong, Tjerk Benschop, Xingchen Chen, Eugene E. Krasovskii, Michiel J. A. de Dood, Rudolf M. Tromp, Milan P. Allan, and Sense Jan van der Molen. Imaging moiré deformation and dynamics in twisted bilayer graphene. *Nature Communications*, 13(1):70, Jan 2022.

[105] Jiawei Hu, Shiyu Zhu, Qianying Hu, Yunhao Wang, Chengmin Shen, Haitao Yang, Xiaoshan Zhu, Qing Huan, Yang Xu, and Hong-Jun Gao. Visualizing the local twist angle variation within and between domains of twisted bilayer graphene. *Chinese Physics Letters*, 41(3):037401, mar 2024.

[106] Justin H. Wilson, Yixing Fu, S. Das Sarma, and J. H. Pixley. Disorder in twisted bilayer graphene. *Phys. Rev. Res.*, 2:023325, Jun 2020.

[107] Naoto Nakatsuji and Mikito Koshino. Moiré disorder effect in twisted bilayer graphene. *Phys. Rev. B*, 105:245408, Jun 2022.

[108] Alex Thomson and Jason Alicea. Recovery of massless dirac fermions at charge neutrality in strongly interacting twisted bilayer graphene with disorder. *Phys. Rev. B*, 103:125138, Mar 2021.

[109] Chao Ding, Han Gao, Lei Sun, Xikui Ma, and Mingwen Zhao. Corrugation effect, dirac cone splitting, and plasmon properties of biased twisted bilayer graphene. *Phys. Rev. B*, 104:155427, Oct 2021.

[110] Tawfiqur Rakib, Pascal Pochet, Elif Ertekin, and Harley T. Johnson. Corrugation-driven symmetry breaking in magic-angle twisted bilayer graphene. *Communications Physics*, 5(1):242, Oct 2022.

[111] Procolo Lucignano, Dario Alfè, Vittorio Cataudella, Domenico Ninno, and Giovanni Cantele. Crucial role of atomic corrugation on the flat bands and energy gaps of twisted bilayer graphene at the magic angle $\theta \sim 1.08°$. *Phys. Rev. B*, 99:195419, May 2019.